Doctoral Dissertation

Studies on Nanometer-sized Artificial Basement Membranes for Cell Compartmentalization in Three-dimensional Tissues

ZENG JINFENG

June 2021

Graduate School of Engineering
Osaka University

Content

General Introduction

The fields of tissue engineering (TE) and regenerative medicine (TERM) have offered the possibility of mitigating the critical shortage of donor organs via the fabrication of three-dimensional (3D) tissue models to repair, improve or replace tissues/organs.[1,2] Over the past few decades, hydrogel scaffolds[3–5] and non-scaffold techniques[6,7] have been extensively used for 3D tissue construction. However, current cell encapsulation systems where multiple cell types are embedded randomly are limited to replicate the complex and hierarchically organized tissues/organs *in vivo* (**Figure 1**). Thus, it is still a considerable challenge to replicate complex and well-organized tissues. Controlling patterned cell localization will be of great importance for the construction of complex compartmentalized 3D tissues.[8] To maintain the spatial positions of multiple types of cells, micropatterned cell co-culture systems are helpful for seeding cells on the patterned substrates.[9–11] However, indirect guidance of cell patterning by patterned material adhesiveness on the substrate is unsuitable for 3D cells co-culture, with limitations in the control of resolution and cell position on existing cell layers. To date, there has been only one report by Takayama[12] *et al.* on customized cell-printing on a cell monolayer for 3D cell co-culture based on an optimized polymeric aqueous biphasic system. However, isolated cell structures cannot be maintained without any physical barriers due to cell migration during cell culture.

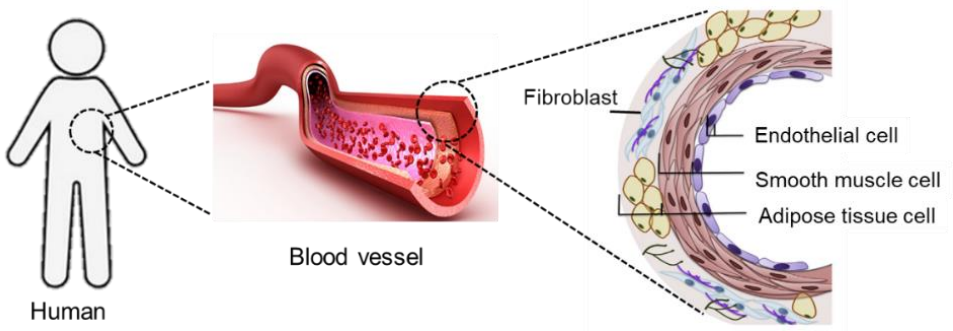

Figure 1. Schematic illustration of well-organized cells/tissue structure *in vivo*.

In vivo, cells and tissues are hierarchically organized by basement membranes (BMs) that divide cells into compartments.[13] BM is a condensed region of extracellular matrix (ECM),

underlies epithelial (endothelial) cells and is surrounded by muscle, fat, and Schwann cells (**Figure 2**).[14] They have been identified in almost all mammalian tissue since 1840.[15] Initially, the BM was regarded as a passive scaffold for the mechanical support of adjacent cells. The organ-specific components and active role of the BM that contribute to both embryonic differentiation and the maintenance of multi-cellular life were subsequently recognized, leading to an understanding of its complexity and heterogeneity[16–20]

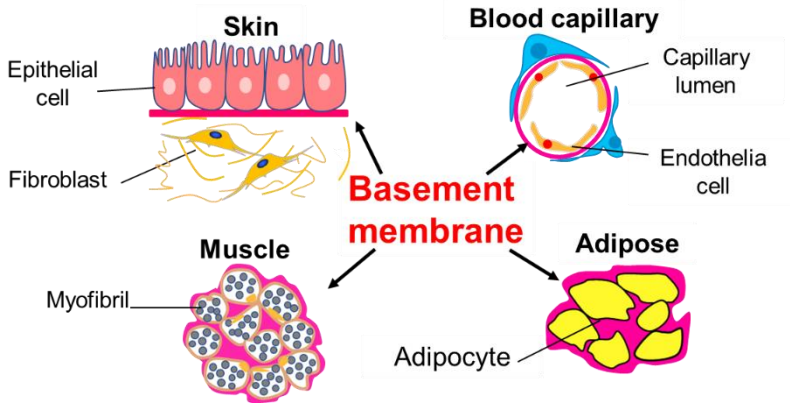

Figure 2. Schematic illustration of compartmentalization cells/tissue structure isolated by BMs.

The BM has been identified as a specialized, condensed ECM protein structure and its composition is dynamic and highly diverse in different tissues.[21] The composition of the BMs is highly diverse and dynamic in different tissues. Generally, collagen type IV (Col-IV) and laminin (LM) are the main components, forming two independent networks by self-assembly. The networks are crosslinked by other ECM proteins, such as nidogen, perlecan, and agrin.[21,22] Col-IV, which accounts for around 50% of BMs, is a kind of nonfibrillar collagen comprising a triple helical collagenous domain and two terminal domains, a 7S domain at the N-terminus and a non-collagenous NC1 domain at the C-terminus (**Figure 3a**). Col-IV is composed of three distinct α chains where each α chain is 400 nm long and around 171 kDa in total. LM (400-800 kDa) is the most abundant noncollagenous protein in BMs and is composed of three heterotrimeric chains, designated as α, β, and γ-chain (**Figure 3b**).[23] LM is a highly biologically active molecule that plays essential roles in regulating cell adhesion, phenotyping, proliferation, and differentiation.[24,25] Furthermore, it is critical for the assembly of BMs-

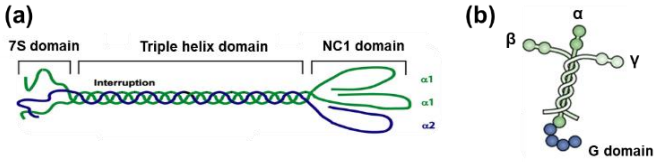

Figure 3. Structure of (a) Col-IV, (b) LM and their domains.

like matrices during early development.[26] Once LM binds to cell membrane receptors, such as integrin and dystroglycan, the polymerization of LM starts, followed by the accumulation of other core components to bridge the networks of Col-IV and LM.[27] Col-IV has been demonstrated to be fundamental to maintain the integrity, stability, and functionality of BMs at their formation stage, even under increasing mechanical demands, due to its covalently stable network.[28,29] It is worth noting that several additional components, such as fibulin, type XV collagen, and type XVIII collagen, account for a small proportion of BMs but are also essential for their assembly and endow BM tissue with specificity and heterogeneity.[23,30]

Besides the specific interactions between BMs components and cells, cell phenotype is also influenced by the biophysical properties of BMs, including topography and mechanical properties. The topography of BMs is a reflection of the BM proteins assembly results, generating a nanometer-scale of thickness and porous structure. As an example, vascular BMs microstructure are shown in **Figure 4**. As described previously, these topographic features also depend on their location, age, and pathological state. For example, the networks of vascular BMs consist of pores and fibers in the submicron (100-1000 nm) and nanoscale (1-100 nm) range, varying by vessel type.[18,31]

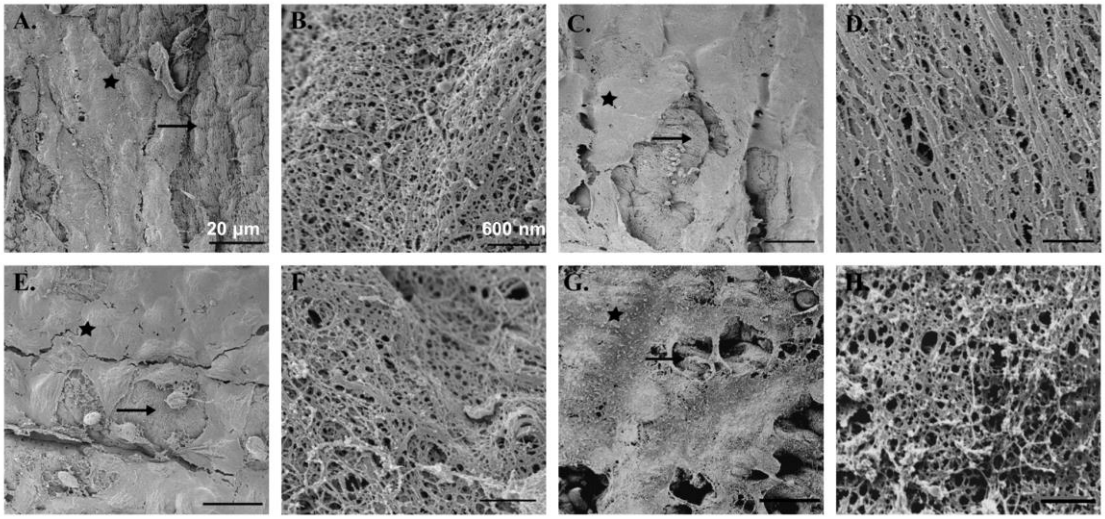

Figure 4. Scanning electron micrographs of the basement membranes from four separate vessels: aorta (A. B), carotid (C. D), saphenous (E. F), and inferior vena cava (G. H).[31]

Since both endothelial (epithelial) cells and mesenchymal cells attach closely to BMs, the mechanical properties of BMs play a vital role in regulating cell functions. Measurements using

atomic force microscopy (AFM), micropipette aspiration, and other methods have indicated that the stiffness of BMs varies by four orders of magnitude (0.5 kPa to 5 MPa) in different tissues. Furthermore, different Young's modulus values have been found on different sides of the BM, where the epithelial side being stiffer than the stromal side.[18] It is noteworthy that the evaluation of BM stiffness *in vivo* remains experimentally challenging, and improved measurement methods are still needed.

Based on their unique components, sophisticated structure, and biophysical properties, BMs exhibit various fundamental functions: (i) serving as a physical barrier to maintain the cell/tissue compartment, (ii) providing mechanical support for surrounding cells, (iii) regulating adjacent cell functions or maintaining cell phenotypes, and (iv) acting as a platform to administer molecular permeability for cell-cell cross-talk.[14,30,32,33]

BMs serve as physical barriers to the passage of both cells and large molecules, maintaining cell compartmentalization, and are essential for forming well-organized tissues. The successful construction of artificial BMs (A-BMs) will contribute to advances in tissue engineering. Inspired by the typical characteristics and biofunctions of natural BMs, the fabrication of A-BMs *in vitro* has to satisfy the following requirements at a minimum (**Figure 5**): (1) nanometer-scale thickness and a porous network, (2) appropriate stiffness, (3) cell separation, and (4) molecular permeability.

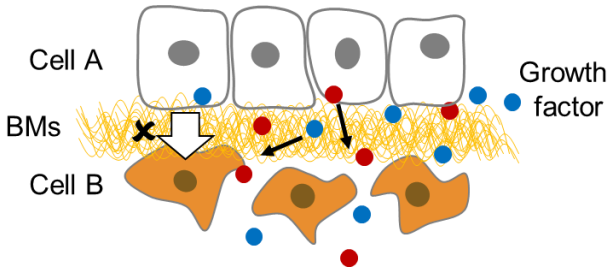

Figure 5. Schematic illustration of the characteristics and functions of BMs.

As described above, natural BMs are highly complicated membranes. Inspired by their ultra-thin, flexible, permeable, and porous structure, several attempts have been reported for compartmentalized cell co-culture from simple polymer membranes to complex ultrathin nanofilms (**Figure 6**).

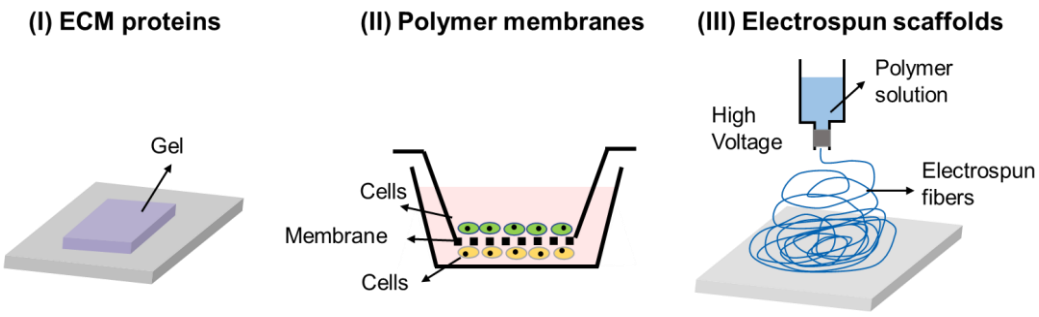

Figure 6. Schematic illustration of the fabrication of A-BMs *in vitro*.

(I) ECM protein gel

Inspired by nature, biofunctional materials can be reconstructed following the design strategies of natural BMs. One of the simplest but most valuable methods uses ECM proteins to imitate natural ECM in cell-based assays.[7,24,34] The use of ECM proteins to mimic the organized microstructure *in vivo* was first introduced by Dunn[35] *et al.* in 1989. They found that adult rat hepatocytes cultured between two layers of type I collagen (Col-I) gel maintained their general morphology and albumin secretion for at least 42 days. However, the albumin secretion of hepatocytes cultured on a single Col-I gel gradually ceased in 7 days but could recover their functionality after putting another layer of Col-I gel. This pioneering work provided a simple, stable culture environment for *in vitro* studies of cell growth, differentiation, and polarity. Even ignoring its barely satisfactory thickness, only Col-I is far from reproducing BMs because of the significant components difference. Since one kind of BMs protein gel was firstly reported in 1986 to stimulate cell growth and differentiation,[36] Matrigel, an extract of BMs from Engelbreth-Holm-Swarm (EHS) tumor, has been widely used for cell/tissue culture.[37,38] Matrigel consists of almost the same components as natural BMs, making it the most BM-like natural matrix model.[25] Nevertheless, due to the tumorigenic origin and species difference, its safety has been disputed. Perry[39] *et al.* used surface initiated assembly (SIA) techniques to develop an engineered BM by casting a dense membrane of Col-IV and LM on a Col-I gel surface at a thickness of approximately 10 μm. They found that corneal endothelium seeded on this engineered BM formed a more intact monolayer than the control group, with continuous tight junction expression between cells. However, its thickness, unclear permeability and Young's modulus restricted its application for separated and bilateral cell co-culture. Following on from the above works, Mondrinos[40] *et al.* incorporated an engineered

ECM proteins membrane into a microfluidic device to create compartmentalized microenvironments for cell co-culture. Changing the engineered ECM protein mixture components, including Col-I, matrix gel, and alginate, endowed this BM mimic membrane with adjustable transparency, stiffness, and porosity. Using this instrument, they found that a compartmentalized, microfluidic cell culture could be constructed to observe the formation of interfaces between various types of tissues. Even though this work paved the way for the evaluation of an engineered ECM protein membrane for compartmentalized tissue culture with the assistance of a microfluidic device, several drawbacks still limited their development. For example, the thickness (20 μm) differs too much from natural BM thickness at the nanometer scale, which in turn influences cellular communication on different sides of the membrane. In summary, the ECM protein gel or membrane showed their great potential for cell-based assays due to the specific interactions between cells and ECM proteins. It, however, suffers from some disadvantages. Due to its physical state, it is challenging to control porous structures for molecular permeability artificially. On the other hand, the thickness of ECM membrane cannot be reduced to nanometer scale, restricting hierarchical cell culture.

(II) Porous polymer membrane

The process of membrane casting using a polymer is easily achievable, and membrane thickness and porosity can be designed to order. Furthermore, compared with ECM proteins, the mechanical properties of engineered polymer membranes are closer to natural BMs.[41,42] Some ultrathin polymer membranes using conventional nano and microfabrication techniques, replica molding, soft-lithography, and so on have been reported to mimic BM structures.[41] Among the numerous materials, commercial porous polycarbonate and polyethylene terephthalate (PET) membranes in transwell insets, without any particular instruments, have been reported to mimic the compartmentalized cell culture microenvironment.[42,43] A Col-IV coated-PET membrane was employed to separate podocytes and endothelial cells on different sides, acting as a glomerular filtration barrier. An albumin permeability assay demonstrated its application for rapid drug testing. However, this simple model cannot fully reproduce the BMs functions because the 10-μm thickness may inhibit cellular communications between cells seeded on different sides of membrane. To overcome the thickness issue, a

poly(dimethylsiloxane) (PDMS)-based ultrathin film would be a promising candidate to mimic BMs. Due to their high transmittance, relatively lower modulus, and biocompatibility, PDMS membranes have been widely used for sensors and microfluidic devices.[44,45] Rathod[41] *et al.* reported a freely suspended ultrathin membrane using spin-coating, which had a sub-micrometer thickness and ~kPa elastic modulus. Meanwhile, the authors used undiluted PDMS Sylgard 527 instead of a conventional diluted polymer solution,[46] to achieve a decreased modulus, thus meeting the requirements of vascular BMs. When human umbilical vein endothelial cells were cultured on BMs mimic membranes, the cell density and spreading area on a thinner membrane were much larger than those on the thicker one. To achieve the submicron thickness of a polymer membrane, the study of porous structure was usually neglected. However, if it lacks sufficient porosity, the obtained compartmentalized tissue structure is far from natural tissues where natural BMs act as a complex platform and administer molecular permeability. To develop an ultra-thin, flexible, and permeable A-BM, Fujie and coworkers[47] used a combination of gravure coating and polymer-based phase separation, firstly reporting a biodegradable, porous, and meter-length scale nanosheets. They successfully induced the differentiation of skeletal muscle cells on this ultra-thin platform, realizing the deposition and even penetration of ECM proteins through a porous structure, and generating multilayered and anisotropic muscular structures.

(III) Electrospun scaffold

To engineer a BM structure, a key challenge is to mimic its complex chemical and physical characteristics. Studies on porous polymer membranes have focused on the porous structure and submicron thickness but the topological structure of natural BMs has generally been ignored. The higher porosity and fibrous structure of electrospun meshes suggest that they would be a better candidate *in vitro*.[27,48] As introduced above, the BM is composed of fibrillar protein networks. Scaffolds that consist of aligned electrospun nanofibers at nanometer diameter can efficiently mimic the nanoscale topography of BMs. Additionally, due to the requirements of the electrospinning process, so far, only polycaprolactone (PCL), poly (lactic-co-glycolic acid) (PLGA), and other synthetic polymer fibers can be produced stably.[27,48] For the fabrication of BM-mimicking networks, different biomolecules are generally used to

modify these nanofibers to improve cell adhesion, such as Col-IV, LM, and Arg-Gly-Asp (RGD) peptides. A promoted endothelialization process of endothelial cell functions was observed on aligned PCL fibers immobilized with Col-IV and LM.[49] Nishiguchi[50,51] *et al.* also reported a bipolar cultured alveolar-capillary barrier model of human primary cells supported by an electrospun mesh consisting of PCL and multifunctional starshaped polyethylene glycols (sPEG). Bioactive laminin ligands were used to decorate the nanofiber surfaces. Compared with microporous films, the obtained nanofiber meshes enhanced the bipolar cultivation of epithelial cells and had a high molecular permeability. Electrospinning is undeniably a well-established technique but its application in the creation of a BM mimetic is still in its early stages. Although appropriate pore size and fiber diameters were observed from SEM images, the studies of interactions between cell and material, and the cell-cell crosstalk through the barrier with a thickness exceeding 10 μm are lacking. On the other hand, the over-reliance on synthetic polymers for electrospun scaffolds are facing obstacles to reproduce the complicated biofunctions of BMs *in vitro*.

In vivo, BMs have complex biological structures and perform various functions by virtue of their specific components. The above techniques have shown their advantages for the production of BMs *in vitro,* including the presence of a porous structure and barrier functions to main cell compartmentalization (**Table 1**). However, a synthetically robust BMs mimic membrane has rarely been reported. Complicated biofunctions, such as the close interactions with cells, were unreachable using the above techniques. As stated earlier, the interactions of natural BMs with cells to regulate cell phenotype, cell fate, cellular communication, and even tissue polarization mainly rely on their components. That's why Col-IV, LM, and their peptides have been chosen to enhance cell adhesion on synthetic polymers. Therefore, if the main components of natural BMs, Col-IV and LM, can be used to construct an ultra-thin membrane *in vitro,* the obtained Col-IV/LM nanofilms would successfully reproduce the biofunctions of BMs. However, due to their limitations, Col-IV/LM nanofilm fabrication using the above techniques is unworkable. Moreover, to reproduce an artificial 3D tissue with various and complicated structures, a shape-customized A-BM is necessary. For this purpose, the *in-situ* construction of an A-BM inside 3D tissues is essential. None of the above techniques is

acceptable to operate on already existing cells or tissues surface.

Table 1. Capability of the different methods to reproduce A-BMs. (✓:convenient, ×: limited)

A-BMs	Nanometer thickness	Porous structure	Proteins applicability	3D patterning
ECM matrix	×	✓	✓	×
Porous polymer films	✓	✓	×	×
Electrospun scaffolds	×	✓	×	×
LbL films	✓	✓	✓	✓

For the construction of an ultra-thin proteins nanofilm, the layer-by-layer (LbL) assembly technique offers a versatile method for controllable bio-coating at micro-/nano-meter scale without any limitations of substrates and materials. Decher[52,53] *et al.* first reported that the LbL assembly technique was a promising surface coating approach. The fabrication of multilayered nanofilms was achieved by immersing the substrates such as glass slides into oppositely charged polymer solutions (**Figure 7**). Researchers subsequently extended the LbL assembly adsorption of polyelectrolytes to uncharged materials, including biomolecules[54,55] and polysaccharides,[56,57] dyes,[58] and nanostructures.[59,60] Solely electrostatic interaction has already been extended to hydrogen bonding,[61] coordinate bonding,[62] covalent bonding,[63] and biologically specific recognition.[64] In the last twenty years, the applications of LbL assembly to design and fabricate nanofilms on a substrate surface for 2D cell culture and nanocoating around the single cell, cell aggregates, or implants for 3D tissue construction has attracted much attention, especially in the biomedical field.[65–67] Advantages of the LbL assembly technique compared with other methods of constructing A-BM are also summarized in **Table 1**, such as controllable nanometer-scale thickness, compatibility to proteins, and the manipulation on living cells. Furthermore, LbL assembly approach possesses another significant advantage: its compatibility with bioprinting, which increases the complexity of the multilayered scaffolds by controlling printing location and patterning.[33]

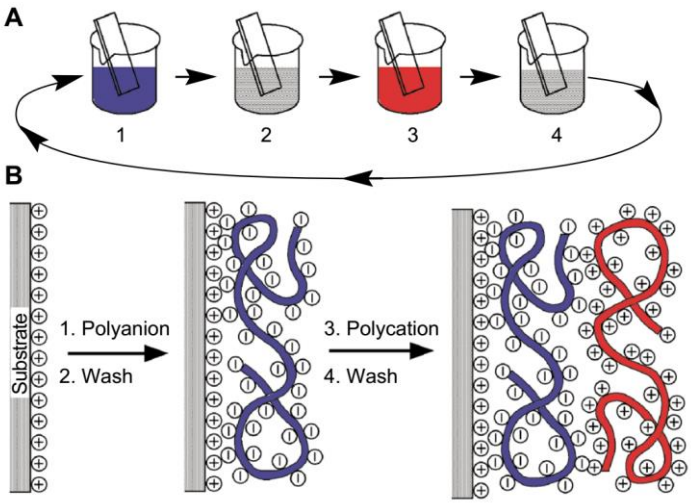

Figure 7. (a) Schematic illustration of the LbL assembly process and (b) the alternate deposition of polyanion and polycation on the substrate for films construction.[53]

Based on this knowledge, Rajagopalan and co-workers assembled a nano-scale polyelectrolyte multilayer scaffold on the top of live mammalian cells for the first time.[68] This polyelectrolyte scaffold could not only provide a cell-adhesive surface for the second layer of cell culture, resulting in a multilayered cellular architecture, but also assist to maintain hepatocytes morphology, cytoskeletal structure, and liver-specific functions. Subsequently, they modulated the assembly of chitosan (polycation) and hyaluronic acid (polyanion) to mimic the physical properties of BMs.[69] However, the dissolving of chitosan needs an acid environment, and the cytotoxicity of polycations also suggested that chitosan and hyaluronic acid assembly is not available on the cell surface. Akashi and co-workers reported a bottom-up strategy through alternate deposition of fibronectin (FN)/gelatin (G) LbL nanofilm and fibroblasts layers to construct 3D tissue models, in which the FN/G nanofilms acted as nano-ECM for cell adhesion.[70] However, FN and other ECM components, such as type I collagen (Col-I), cannot prevent cell migration. Kino-oka[71] *et al*. also reported that endothelial cells seeded on the bottom can migrate through human skeletal muscle myoblast (HSMM) sheets, forming net-shaped aggregates, even with the distribution of FN and Col-I matrix between cell sheets. Therefore, a robust A-BM with a similar microstructure to natural BMs, suitable mechanical properties, essential biofunctions, and barrier ability to maintain cell separation as well as the cytocompatibility to construct directly inside 3D tissues is strongly desired.

In this thesis, the author aimed to develop a robust A-BM to maintain cell compartmentalization for the construction of organized 3D tissues *in vitro* (**Figure 8**). Using natural BMs components, nanometer-sized Col-IV and LM multilayered films were constructed in 3D tissues directly by the LbL assembly approach to replicate BMs. The microstructure, mechanical properties, barrier functions to isolate cells, and molecular permeability were evaluated. Transglutaminase (TGase) as a biosafety crosslinking promoter was used to enhance the stability of the obtained Col-IV/LM nanofilms for long-time compartmentalized cell co-culture. Furthermore, in order to apply obtained A-BMs in different tissues, shape-customized LbL nanofilms were constructed in 3D tissues by the combination of LbL assembly approach and inkjet printing.

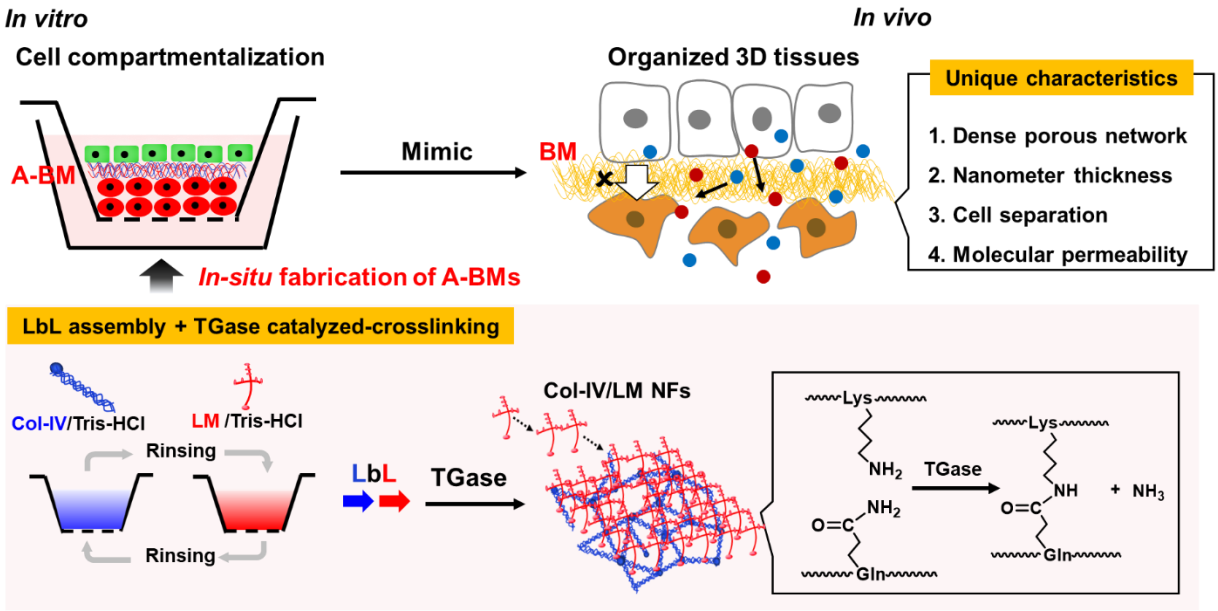

Figure 8. Schematic illustration of the fabrication of robust A-BMs based on multilayered Col-IV/LM nanofilms by LbL assembly approach and *in-situ* TGase catalyzed-crosslinking to maintain cell compartmentalization between fibroblasts and endothelial cells *in vitro*.

Outline of this thesis

In this thesis, the author describes the fabrication of A-BMs and their barrier ability to main cell compartmentalization for the construction of organized 3D tissues. This thesis includes the following four chapters.

Chapter 1

Fabrication of Artificial Basement Membrane by Layer-by-Layer Assembly for Cell Compartmentalization

Nanometer-sized artificial basement membranes (A-BMs) through layer-by-layer (LbL) assembly of collagen type IV (Col-IV) and laminin (LM) were constructed directly in 3D tissues. Col-IV and LM are the main components of natural BMs and have the potential to replicate natural BMs structure and biofunctions *in vitro*. *In-situ* construction of A-BMs on cell surfaces provides a basis for constructing complicated and organized 3D tissues. Studies in this chapter focused on the fabrication of A-BMs and evaluation of their microstructure, effects on cell behaviors and barrier functions to maintain cell compartmentalization.

Chapter 2

Analysis of Structure and Mechanical Property of Artificial Basement Membranes on Endothelial Cell Functions

In chapter 2, the author further studied the structure and mechanical properties of the obtained A-BMs. A wide range of roughness and Young's modulus were achieved by simply adjusting the concentration of assembly solutions to meet the mechanical requirements of A-BMs used in various tissues. The effects of A-BMs structure and mechanical properties on endothelial cell (EC) functions, including cell adhesion, spreading, proliferation, and barrier integrity of the confluent EC monolayer, were evaluated. Studies in this chapter highlight the influence of LbL assembly conditions on endothelial functions, which offer a new criterion for the design of A-BMs in well-organized 3D tissues.

Chapter 3

***In-situ* Crosslinking of Artificial Basement Membranes and Their Size-dependent Molecular Permeability**

In chapter 3, we tried *in-situ* crosslinking of Col-IV/LM nanofilms after fabrication on 3D tissues of normal human dermal fibroblasts (NHDF) by adding TGase to obtain stable A-BMs. Through *in-situ* crosslinking, the A-BMs were stably maintained between endothelial cells and NHDF tissues for at least 5 days and the permeability of A-BMs was retained even after crosslinking. To the best of our knowledge, this is the first report on the *in-situ* crosslinking of nanofilms in living 3D tissues. In this chapter, the effects of molecular size and conformation on the transport kinetics of molecules through the Col-IV/LM nanofilms were assessed. Furthermore, based on the permeability, we evaluated the cell-cell cross-talk through the barrier of Col-IV/LM nanofilms. The use of Col-IV/LM nanofilms as A-BMs provides a broader perspective for understanding the unique barrier functions to maintain cell separation while allowing the molecular permeability of natural BMs.

Chapter 4

Fabrication of Shape-customized Artificial Basement Membranes in Organized 3D Tissues

In chapter 4, based on the similar microstructure, using the robust barrier ability for maintaining cell separation and molecular permeability of Col-IV/LM multilayer nanofilms, shape-customized A-BMs were constructed between fibroblasts and endothelial cell layers by alternate printing of Col-IV and LM for a patterned 3D cell co-culture. The author assessed the possibility of combining inkjet printing with the LbL assembly approach to control the shape of LbL nanofilms. The barrier ability of shape-customized LbL NFs to maintain cell compartmentalization was also analyzed.

Reference

[1] V. M. Gaspar, P. Lavrador, J. Borges, M. B. Oliveira, J. F. Mano, *Adv. Mater.* **2020**, *32*, 1903975.
[2] D. F. Williams, *Front. Bioeng. Biotechnol.* **2019**, *7*, 127.
[3] C.-Y. Liaw, S. Ji, M. Guvendiren, *Adv. Healthcare Mater.* **2018**, *7*, 1701165.
[4] M. Matsusaki, H. Yoshida, M. Akashi, *Biomaterials* **2007**, *28*, 2729.
[5] J. Pant, J. Sundaram, M. J. Goudie, D. T. Nguyen, H. Handa, *J. Biomed. Mater. Res.* **2019**, *107*, 1068.
[6] A. Alghuwainem, A. T. Alshareeda, B. Alsowayan, *IJMS* **2019**, *20*, 4926.
[7] M. Matsusaki, C. P. Case, M. Akashi, *Adv. Drug Delivery Rev.* **2014**, *74*, 95.
[8] C. R. Correia, S. Nadine, J. F. Mano, *Adv. Funct. Mater.* **2020**, 1908061.
[9] R. Singhvi, A. Kumar, G. Lopez, G. Stephanopoulos, D. Wang, G. Whitesides, D. Ingber, *Science* **1994**, *264*, 696.
[10] C. A. Goubko, X. Cao, *Mater. Sci. Eng., C* **2009**, *29*, 1855.
[11] P.-O. Strale, A. Azioune, G. Bugnicourt, Y. Lecomte, M. Chahid, V. Studer, *Adv. Mater.* **2016**, *28*, 2024.
[12] H. Tavana, B. Mosadegh, S. Takayama, *Adv. Mater.* **2010**, *22*, 2628.
[13] M. P. M, *Crit. Rev. Biochem. Mol. Biol.* **1992**, *27*, 93.
[14] P. D. Yurchenco, *Cold Spring Harbor Perspect. Biol.* **2011**, *3*, a004911.
[15] B. William, *Philos. Trans. R. Soc. London*, 1840, 130, 457-501.
[16] A. L. Fidler, C. E. Darris, S. V. Chetyrkin, V. K. Pedchenko, S. P. Boudko, K. L. Brown, W. Gray Jerome, J. K. Hudson, A. Rokas, B. G. Hudson, *eLife* **2017**, *6*, e24176.
[17] R. W. Naylor, M. R. P. T. Morais, R. Lennon, *Nat. Rev. Nephrol.* **2021**, *17*, 112.
[18] C. Leclech, C. F. Natale, A. I. Barakat, *J. Cell Sci.* **2020**, *133*, jcs239889.
[19] B. G. Hudson, S. T. Reeders, K. Tryggvason, *J. Biol. Chem.* **1993**, *268*, 26033.
[20] R. Kalluri, C. F. Shield, P. Todd, B. G. Hudson, E. G. Neilson, *J. Clin. Invest.* **1997**, *99*, 2470.
[21] E. Hohenester, P. D. Yurchenco, *Cell Adhes. Migr.* **2013**, *7*, 56.
[22] R. Kalluri, *Nat. Rev. Cancer* **2003**, *3*, 422.
[23] V. S. LeBleu, B. MacDonald, R. Kalluri, *Exp. Biol. Med. (Maywood)* **2007**, *232*, 1121.
[24] A. E. Stanton, X. Tong, F. Yang, *Acta Biomater.* **2019**, *96*, 310.
[25] R. Cruz-Acuña, A. J. García, *Matrix Biol.* **2017**, *57–58*, 324.
[26] K. K. McKee, D. Harrison, S. Capizzi, P. D. Yurchenco, *J. Biol. Chem.* **2007**, *282*, 21437.
[27] S. Pazhanimala, D. Vllasaliu, B. Raimi-Abraham, *Appl. Sci.* **2019**, *9*, 910.
[28] E. Poschl, *Development* **2004**, *131*, 1619.
[29] G. Bhave, S. Colon, N. Ferrell, *Am. J. Physiol. Renal. Physiol.* **2017**, *313*, F596.
[30] A. Pozzi, P. D. Yurchenco, R. V. Iozzo, *Matrix Biol.* **2017**, *57–58*, 1.
[31] S. J. Liliensiek, P. Nealey, C. J. Murphy, *Tissue Eng., A* **2009**, *15*, 2643.
[32] R. Timpl, J. C. Brown, *Bioessays* **1996**, *18*, 123.
[33] G. Perry, W. Xiao, G. I. Welsh, A. W. Perriman, R. Lennon, *Integr. Biol.* **2018**, *10*, 680.
[34] F. Louis, S. Kitano, J. F. Mano, M. Matsusaki, *Acta Biomater.* **2019**, *84*, 194.
[35] J. C. Y. Dunn, M. L. Yarmush, H. G. Koebe, R. G. Tompkins, *FASEB j.* **1989**, *3*, 174.
[36] H. K. Kleinman, M. L. McGarvey, J. R. Hassell, V. L. Star, F. B. Cannon, G. W. Laurie,

G. R. Martin, *Biochemistry* **1986**, *25*, 312.
[37] G. Benton, I. Arnaoutova, J. George, H. K. Kleinman, J. Koblinski, *Adv. Drug Delivery Rev.* **2014**, *79–80*, 3.
[38] M. E. Dolega, F. Abeille, N. Picollet-D'hahan, X. Gidrol, *Biomaterials* **2015**, *52*, 347.
[39] R. N. Palchesko, J. L. Funderburgh, A. W. Feinberg, *Adv. Healthcare Mater.* **2016**, *5*, 2942.
[40] M. J. Mondrinos, Y.-S. Yi, N.-K. Wu, X. Ding, D. Huh, *Lab Chip* **2017**, *17*, 3146.
[41] M. L. Rathod, J. Ahn, B. Saha, P. Purwar, Y. Lee, N. L. Jeon, J. Lee, *ACS Appl. Mater. Interfaces* **2018**, *10*, 40388.
[42] M. Li, A. Corbelli, S. Watanabe, S. Armelloni, M. Ikehata, V. Parazzi, C. Pignatari, L. Giardino, D. Mattinzoli, L. Lazzari, A. Puliti, F. Cellesi, C. Zennaro, P. Messa, M. P. Rastaldi, *Eur. J. Pharm. Sci.* **2016**, *86*, 1.
[43] R. Booth, H. Kim, *Lab Chip* **2012**, *12*, 1784.
[44] M. Cha, J. Shin, J.-H. Kim, I. Kim, J. Choi, N. Lee, B.-G. Kim, J. Lee, *Lab Chip* **2008**, *8*, 932.
[45] S. Kim, S. Han, J. Lee, *Lab Chip* **2017**, *17*, 2095.
[46] A. L. Thangawng, R. S. Ruoff, M. A. Swartz, M. R. Glucksberg, *Biomed. Microdevices* **2007**, *9*, 587.
[47] S. Suzuki, K. Nishiwaki, S. Takeoka, T. Fujie, *Adv. Mater. Technol.* **2016**, *1*, 1600064.
[48] J. Xue, T. Wu, Y. Dai, Y. Xia, *Chem. Rev.* **2019**, *119*, 5298.
[49] C. Yu, G. Guan, S. Glas, L. Wang, Z. Li, L.-S. Turng, *Bio-des. Manuf.* **2021**, *4*, 171.
[50] A. Nishiguchi, S. Singh, M. Wessling, C. J. Kirkpatrick, M. Möller, *Biomacromolecules* **2017**, *18*, 719.
[51] E. Dohle, S. Singh, A. Nishigushi, T. Fischer, M. Wessling, M. Möller, R. Sader, J. Kasper, S. Ghanaati, C. J. Kirkpatrick, *Tissue Eng., Part C* **2018**, *24*, 495.
[52] G. Decher, J.-D. Hong, *Makromol. Chem. Macromol. Symp.* **1991**, *46*, 321.
[53] G. Decher, *Science* **1997**, *277*, 1232.
[54] M. Matsusaki, K. Fujimoto, Y. Shirakata, S. Hirakawa, K. Hashimoto, M. Akashi, *J. Biomed. Mater. Res., Part A* **2015**, *103*, 3386.
[55] Y. B. Lee, J. Lee, H. Byun, T. Ahmad, M. Akashi, M. Matsusaki, H. Shin, *Biofabrication* **2018**, *10*, 025001.
[56] N. I. Martins, M. P. Sousa, C. A. Custódio, V. C. Pinto, P. J. Sousa, G. Minas, F. Cleymand, J. F. Mano, *Acta Biomater.* **2017**, *57*, 313.
[57] H. Chang, M. Hu, H. Zhang, K. Ren, B. Li, H. Li, L. Wang, W. Lei, J. Ji, *ACS Appl. Mater. Interfaces* **2016**, *8*, 14357.
[58] Y. Zhang, W. Cao, *New J. Chem.* **2001**, *25*, 483.
[59] D. S. Couto, N. M. Alves, J. F. Mano, *J. Nanosci. Nanotechnol.* **2009**, *9*, 1741.
[60] S. Gil, J. M. Silva, J. F. Mano, *ACS Biomater. Sci. Eng.* **2015**, *1*, 1016.
[61] H. Lee, R. Mensire, R. E. Cohen, M. F. Rubner, *Macromolecules* **2012**, *45*, 347.
[62] X. Wang, Z. Jiang, J. Shi, Y. Liang, C. Zhang, H. Wu, *ACS Appl. Mater. Interfaces* **2012**, *4*, 3476.
[63] Q. An, T. Huang, F. Shi, *Chem. Soc. Rev.* **2018**, *47*, 5061.
[64] M. Matsusaki, M. Akashi, *Polym. J.* **2014**, *46*, 524.
[65] M. Matsusaki, H. Ajiro, T. Kida, T. Serizawa, M. Akashi, *Adv. Mater.* **2012**, *24*, 454.
[66] M. J. Landry, F.-G. Rollet, T. E. Kennedy, C. J. Barrett, *Langmuir* **2018**, *34*, 8709.

[67] J. M. Silva, R. L. Reis, J. F. Mano, *Small* **2016**, *12*, 4308.
[68] P. Rajagopalan, C. J. Shen, F. Berthiaume, A. W. Tilles, M. Toner, M. L. Yarmush, *Tissue Eng.* **2006**, *12*, 1553-1563.
[69] A. L. Larkin, R. R. Rodrigues, T. M. Murali, P. Rajagopalan, *Tissue Eng., Part C* **2013**, *19*, 875.
[70] M. Matsusaki, K. Kadowaki, Y. Nakahara, M. Akashi, *Angew. Chem., Int. Ed.* **2007**, *46*, 4689.
[71] E. Nagamori, T. X. Ngo, Y. Takezawa, A. Saito, Y. Sawa, T. Shimizu, T. Okano, M. Taya, M. Kino-oka, *Biomaterials* **2013**, *34*, 662.

Chapter 1

Fabrication of Artificial Basement Membrane by Layer-by-Layer Assembly for Cell Compartmentalization

1.1 Introduction

Localized between epithelial (endothelial) cells and underlying connective tissues, BMs provide cell and tissue support and act as platforms for complex signaling. Anchored closely to BMs platform, cell behaviors are modulated through the specific interactions between cell membrane receptors and BMs components, especially Col-IV and LM.[1,2] As the main components of BMs, the presence of Col-IV networks is essential to integrate other components of BMs, including laminin, entactin, and perlecan, into highly organized supramolecular architectures.[2] Col-IV was demonstrated to be fundamental to maintain the integrity, stability, and functionality of BMs at the stage of BMs formation, even under increasing mechanical demands.[3] Some specific cell binding-sites were localized to the major triple-helical domain of Col-IV,[4] which plays a part in guiding cells behaviors, *e.g.,* modulating the migration and adhesion of epithelial cells that are the essential processes of re-epithelialization. Meanwhile, LM is critical for the assembly of BMs-like matrices during early development.[5] LM interacts with adjacent cells by specific cell-binding and these cell-matrix interactions contribute to anchoring adhered cells into 3D ECM that is essential for the physiological function and tissue organization.[1] Both Col-IV and LM are reported to relate to angiogenesis, for example, the NC1 domain of Col-IV can suppress tumor growth and inhibit endothelial cell migration and induce cell apoptosis.[6,7] Thus, as "functional polymers", Col-IV and LM would be promising candidates to reproduce complicated structure and biofunctions of natural BMs *in vitro*.

As mentioned in the general introduction, compared with other techniques, LbL assembly approach has more advantages in the fabrication of nanometer-scale protein films on existing cell monolayers directly. The only requirement is the interactions between assembly components.[8] By observing the bonding sites of LM with Col-IV or pepsin digested Col-IV

using transmission electron microscopy (TEM), researchers found that short arms of LM generally contacted Col-IV on the areas of ~81 nm, ~216 nm, and ~291 nm from the carboxy end of Col-IV.[9] Furthermore, LM was demonstrated to bind preferentially to Col-IV over other collagens based on the biologically specific recognition.[10] Nugroho[11] *et al.* quantified the adhesion energies of Col-IV, Col-I, LM, and cellulose nanofibrils using the AFM-colloidal probe technique, and they found that the absorption force between Col-IV and LM was higher than the other groups. These results explained the potential to construct Col-IV/LM nanofilms using LbL assembly approach.

In this chapter, an ultra-thin film was fabricated by the LbL assembly of Col-IV and LM. The LbL assembly process, microstructure, and barrier functions of Col-IV/LM were evaluated.

1.2 Experiments

1.2.1 Materials

Collagen type IV (Col-IV) was purchased from Sigma-Aldrich (C7521, Missouri, USA). Laminin-111 (LM) was purchased from Corning (354259, New York, USA). Normal human dermal fibroblast cells (NHDF, CC-2509), and human umbilical vein endothelial cells (HUVEC, C2517A), were obtained from Lonza (Basel, Switzerland). GFP expressed human umbilical vein endothelial cells (GFP-HUVEC) were purchased from Argio-Proteomie (Massachusetts, USA). Collagenase type IV was purchased from Gibco BRL, Life Technologies (Rockville, Maryland, USA). Crystal violet hydrate was purchased from TCI (548-62-9, Tokyo, Japan). Collagen type IV, FAM conjugated was purchased from AnaSpec (AS-85112, California, USA), and Laminin (Red fluorescent, rhodamine) was purchased from Cytoskeleton (LMN01-A, Colorado, USA). CellTracker Deep Red and Pacific Blue of goat anti-mouse IgG were purchased from Invitrogen (California, USA). Monoclonal mouse antihuman CD31 antibody was purchased from Dako (M0823, Glostrup, Denmark). An AT-cut quartz crystal (9 mm diameter) with a parent frequency of 9 MHz and a frequency counter (model 53131A) were purchased from USI (Fukuoka, Japan).

1.2.2 Col-IV/LM multilayered nanofilm preparation

The quantitative analysis of LbL assembly was performed using a quartz crystal microbalance (QCM) as our previously reported protocols.[12,13] At first, the QCM chip was treated by Piranha solution (H_2SO_4/40% H_2O_2 aqueous solution=3:1 in volume) twice. Following the cleaning step, the QCM chip was alternately immersed into Col-IV (40 μg/mL) and LM (40 μg/mL)/Tris-HCl buffer solution (50 mM, pH=7.4) for 15 min at 37 °C. Between each step, the QCM chip was rinsed with 1mM Tris-HCl buffer solution (pH=7.4), and then dried under N_2 gas. The alternate steps were repeated until 5 bilayers, the nanofilm was denoted as $(Col\text{-}IV/LM)_5$ nanofilms (Col-IV/LM NFs). For each step, frequency shift (ΔF) was recorded, and the amount (Δm) of deposition was obtained by calculating according to the Sauerbrey equation: $-\Delta F$ (Hz)=1.15 Δm (ng).[14] After further calculation according to the deposited amount and assumed nanofilm density of proteins and polyelectrolytes at 1.3 and 1.2 g/cm^3,[15] respectively, the thickness of the resultant Col-IV/LM NFs was obtained following the equation: thickness (nm)=Δm (ng)/1.3 (g/cm^3)/0.159 (cm^3)/2. In the same way, LbL assembly of Col-IV and LM solution at 4, 8, 80, 400, and 1000 μg/mL were also performed and the effects of sodium chloride (NaCl) on LbL assembly were analyzed by adding various amounts of NaCl into Tris-HCl buffer solution (0, 0.15, and 1 mol/L respectively).

1.2.3 Characterization of Col-IV/LM NFs

The stability of Col-IV/LM NFs was measured by immersing samples coated onto the QCM chips into PBS solution (pH=7.4) at 37 °C for 7 days. Frequency shifts of the QCM chips were recorded at intervals. PBS solution was renewed every day. The degradation of Col-IV/LM NFs was analyzed by immersing them into a collagenase-IV/PBS solution (100 U/mL) at 37 °C. The weight of the remaining amount of nanofilms was measured using QCM. The surface wettability of Col-IV/LM NFs was analyzed through the contact angles between water and the surface of the samples. Contact angles of Col-IV/LM NFs were evaluated by Drop Master (Kyowa Interface Science, Saitama, Japan).

1.2.4 Cell adhesion

Cell Culture: NHDF (passage: 6-8) were cultured with DMEM containing 10% FBS and 1% penicillin/streptomycin in 5% CO_2 at 37 °C. HUVEC (passage: less than 8-10) were cultured in EGM-2.

6-well polystyrene plates with or without tissue culture treatment were used for cell culture substrate, noted as TCPS and PS, respectively. Same with the LbL assembly process using QCM, 2 mL of Col-IV (40 μg/mL) and LM (40 μg/mL) in Tris-HCl buffer solution (50 mM, pH=7.4) were alternately added into the 6-well plate, incubated at 37 °C for 15 min, followed by a rinsing step between each protein deposition by 1 mM of Tris-HCl solution. The alternate steps were repeated until the desired bilayer numbers were reached. The multilayered nanofilms were washed with PBS three times. 1.0×10^5 of NHDF and HUVEC in 2 mL medium were seeded onto the nanofilms, respectively. After 1 and 24 h of incubation, the culture medium was removed and samples were washed with PBS three times to remove nonadherent cells. Cell morphology was observed using an FL EVOS Auto microscope (Thermo Fisher, USA). Cell number was counted by trypan blue staining.

1.2.5 Cell viability

The viability of NHDF with Col-IV/LM NFs was performed using a Live/Dead viability assay kit and WST-8 kit assay. Col-IV/LM NFs were coated into a cell culture plate by LbL assembly and were washed with PBS three times. For Live/Dead viability assay kit, 1 mL of 1.0×10^5 NHDF were seeded in each well (24-well plate) and then incubated at 37 °C for 24 h. After a further washing with PBS, 300 μL of PBS solution containing Calcein AM and EthD-III/PBS (2 μmol/L) was added into each well, followed by incubation at 37 °C for 45 min in the dark. After incubation, the nanofilms were washed with PBS three times. Images were obtained using a confocal laser scanning microscope (CLSM, FV 3000, Olympus, Japan). ImageJ software was used for the analysis of the projections, calculating the percentage of each staining (1280×1280 μm, n=3). For WST-8 kit assay, 100 μL of 1.0×10^4 NHDF were cultured in 96-well plate at 37 °C for 24 h. After a further washing with PBS, 100 μL of cell count

reagent SF/DMEM (1:9, without phenol red) was added to each well. The cells were incubated for another 2-4 h at 37 °C. And then transferring the supernatant to a new well, the absorbance of supernatant at 450/600 nm was measured by microplate reader.

1.2.6 Cell staining

CellTracker staining: Briefly, CellTracker Deep Red was dissolved in dimethyl sulfoxide (DMSO) at 1.0×10^{-3} m, then diluted into FBS-free medium at 1:1000 (v:v). Precultured cells were rinsed with PBS three times and exposed to the diluted dye for 40 min at 37 °C. Next, the medium with CellTracker was aspirated, and cells were washed with PBS three times. Cells were incubated with DMEM at 37 °C for at least 24 h before being detached.

Immunofluorescence staining: After incubation, samples were washed with PBS three times and fixed by 4% paraformaldehyde (PFA) for 15 min at room temperature. After washing with PBS three times, 0.2% Triton-X 100 was incubated with cells for enhancing antibody permeability for 30 min at room temperature. Next, after washing with PBS three times, 1% BSA/PBS solution was added at room temperature for 30 min in order to block the unspecific staining of the antibody. The cells were then washed with PBS three times and incubated with CD31 (primary antibody, diluted 100 times in 1% BSA/PBS solution) at 4 °C, overnight. After a further three times washing with PBS, Pacific Blue (secondary antibody, anti-mouse, diluted 100 times in 1% BSA/PBS solution) was added and samples were incubated at room temperature for 2 h. Fluorescence images were observed with FV 3000.

Histology staining: Samples were fixed in 4% PFA for 15 min at room temperature, washed with PBS three times, and then sent to the Applied Research Company for paraffin embedding. Sectional samples were stained with hematoxylin and eosin (H&E) and CD31. Brightfield images were captured using an FL Evos Auto microscope (Thermo Fisher Scientific, MA, USA).

1.2.7 Cell compartmentalization

The barrier effect of Col-IV/LM NFs was analyzed by the “scaffold” and “sandwich”

methods.

"scaffold" method: a 24-well insert with a 3.0 μm pore size served as a "scaffold" and Col-IV/LM NFs (40 and 1000 μg/mL, respectively) were deposited onto the insert membrane. 300 μL of 2.0×10^5 HUVEC were seeded in each insert and 1 mL of medium was added outside. After incubation at 37 °C for 6, 8 12, 24, and 48 h, part of the cells migrated to the other side of insert. After washing with PBS three times, unmigrated cells inside the insert were completely removed by cotton swabs and migrated cells were stained with crystal violet/PBS solution (1.0 mg/mL) for 15 min and then washed with PBS three times. The samples were then examined by phase contrast microscope. ImageJ software was used for the analysis of migrated cell number and coverage ratio.

"sandwich" method: Col-IV/LM NFs (1000 μg/mL) was deposited between NHDF layers (1.0×10^6) and a GFP-HUVEC (1.0×10^5) monolayer, forming a "sandwich" structure which is similar to the structure of natural tissues. First, 300 μL of 1.0×10^6 NHDF were seeded into a 24-well insert which was incubated into LM (40 μg/mL)/Tris-HCl solution (50 mM, pH=7.4) at 37 °C for 2 h for cell adhesion. 1 mL of DMEM was added outside and the sample was incubated at 37 °C for 24 h. After washing with PBS, Col-IV and LM/Tris-HCl solution were alternately added into the insert, forming Col-IV/LM NFs at the surface of 3D NHDF tissues. Following seeding with 1.0×10^5 HUVEC, cells were incubated at 37 °C. The migration of HUVEC after 1, 2, 3, and 4 days was observed by FV 3000. Images were digitized using Imaris software (ver. 9.2.1, Oxford Instruments) and migrated cell number and depth were calculated using ImageJ.

Statistical Analysis: In this study, three independent experiments were carried out for each experiment, and the results are expressed in the format of means±SD. Error bars represent standard deviations. For statistical analyses, Student's *t*-test was run to assess the variance. Test gave *p* values considered significant if $*p < 0.05$.

1.3 Results and discussion

1.3.1 Col-IV/LM multilayered nanofilm preparation

The preparation of nanometer-scale multilayered nanofilms was performed by the alternate deposition of Col-IV and LM, in which LM was demonstrated to bind preferentially to Col-IV over other collagens,[10,11] as shown in **Figure 1-1a**. This assembly process was assessed using a quartz crystal microbalance (QCM). **Figure 1-1b** shows the results of LbL assembly of Col-IV and LM. As expected, frequency shift (ΔF) clearly increased with the alternate deposition of Col-IV and LM onto a gold piezoelectric crystal chip, conforming the successful fabrication of multilayered Col-IV/LM nanofilms. 5 bilayers were performed in this thesis and obtained nanofilms were noted as $(Col\text{-}IV/LM)_5$ nanofilms (Col-IV/LM NFs). The thickness of Col-IV/LM NFs can be adjusted in the range of 4-140 nm by controlling the concentration of Col-IV and LM (**Figure 1-1c**), which are similar with natural BMs at 50-100 nm thickness.[16] Due to the strong interaction between Col-IV and LM and advantages of the LbL assembly technique, even 4 nm of nanofilms can be obtained from the lowest concentration, 4 μg/mL (**Figure 1-1b, c**). Additionally, assembly from higher concentration solutions, 1000 μg/mL, the deposited amount of both Col-IV and LM sharply increased, obtained a much thicker nanofilm. This is probably resulted from the self-assembly of Col-IV and LM during LbL assembly process due to the higher concentrations.[17,18] By simply changing assembly steps and solution concentrations, Col-IV/LM NFs with various thicknesses can be applied to construct of A-BMs in different 3D tissue models.

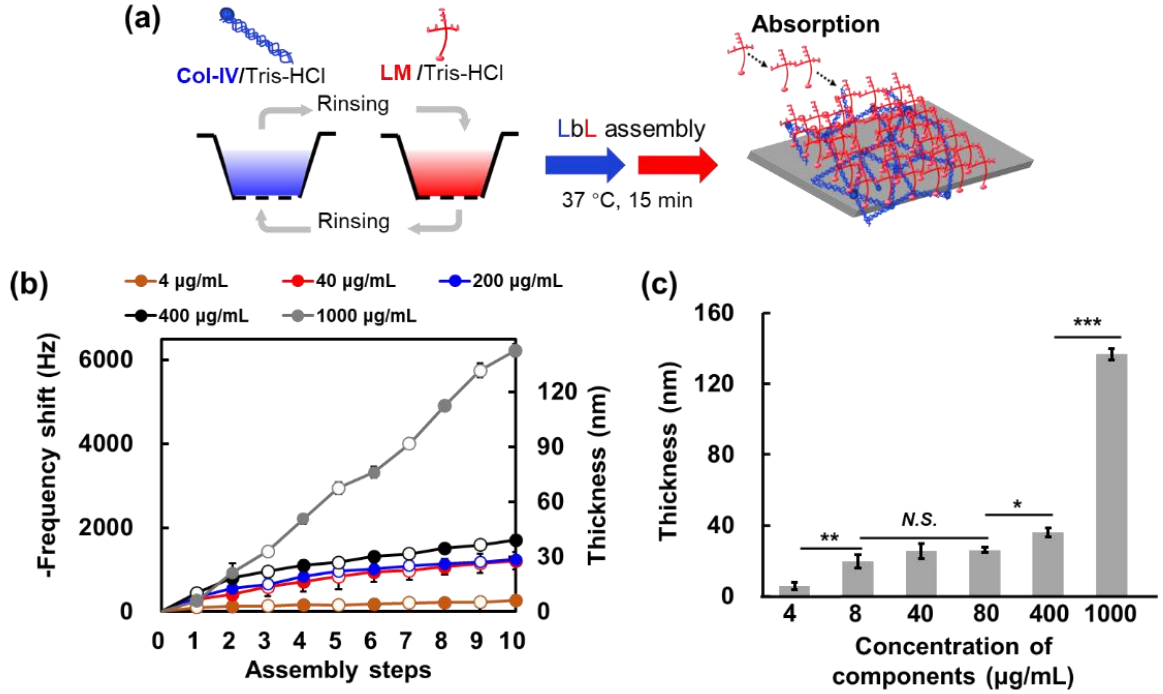

Figure 1-1. (a) Schematic illustration of alternate deposition of Col-IV and LM for the construction of LbL NFs. (b) Frequency shift and thickness increase of Col-IV (●) and LM (○) assembly in Tris-HCl buffer solutions (50 mM, pH=7.4, 37 °C), n=3. (c) Adjustable thicknesses obtained by changing Col-IV and LM/Tris-HCl solution concentrations. n=3, *$p < 0.05$, **$p < 0.01$, and ***$p < 0.001$.

Generally, LbL assembly process of polyelectrolytes based on electrostatic interaction is greatly influenced by ionic strength because of the charge shielding effects.[19] **Figure 1-2** describes the different growth models of LbL assembly process of general polyelectrolytes and Col-IV/LM at various amounts of NaCl, respectively. With the increase of NaCl concentrations, the thicknesses of poly(diallyldimethylammonium chloride)/poly(styrenesulfonate) (PDDA/PSS) LbL films increased, even changed to exponential growth. However, Col-IV/LM NFs thicknesses decreased gradually with the increase of NaCl concentrations (**Figure 1-2b**). This phenomenon is caused by the different polymer conformation between general polyelectrolytes and proteins. At lower NaCl concentrations, both polyelectrolytes and proteins follow the basic alternate deposition process. However, when NaCl concentration increased, the first layer of PDDA tended to form a more random coil or globular shape whose repulsive force of the same charge became weak due to the partial charge shielding effect. More polyanion can be absorbed to the underlying curly polycation, forming thicker nanofilms and

exponential growth.[20] However, the spatial structure of proteins cannot be changed within a certain concentration range of NaCl,[21] and LM tends to interact with Col-IV scaffold on specific domains.[10] Meanwhile, the interactions between Col-IV and LM, such as electrostatic interaction was weakened by the charge shielding effects. Thus, fewer Col-IV or LM molecules can be absorbed onto the previous layer, showing weaker interaction with more NaCl ions. From this basis, Tris-HCl buffer solution without NaCl was used for further preparation of Col-IV/LM NFs. On the other hand, the growth process of Col-IV/LM NFs follows a linear growth no matter of the NaCl concentration. And linear growth of LbL NFs generally leads to a smooth surface, elastic nanofilm, and lower permeability, which satisfied the requirements of A-BMs.

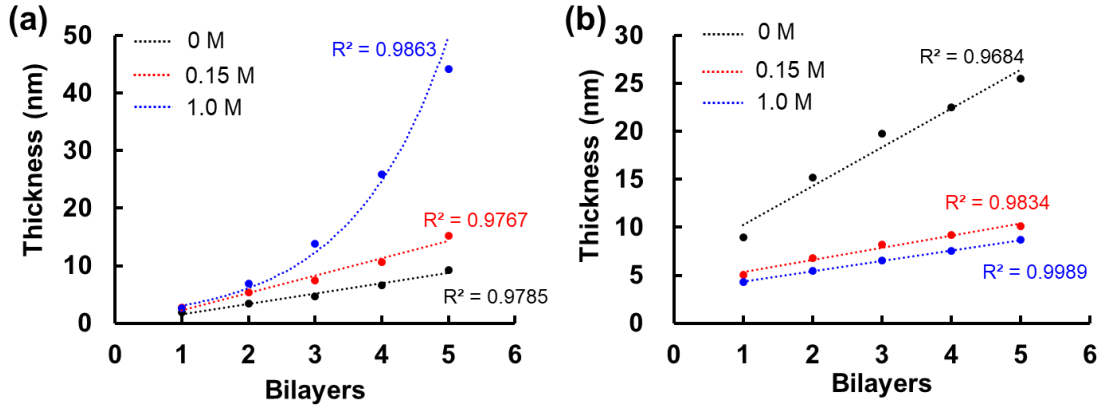

Figure 1-2. Cumulative thickness evolution of (a) PDDA/PSS and (b) Col-IV/LM multilayered nanofilms as a function of the number of deposition layers with various NaCl concentrations in Tris-HCl buffer solution (50 mM, pH=7.4, 37 ℃).

1.3.2 Microstructure of Col-IV/LM NFs

Microstructure of Col-IV/LM NFs obtained from different concentrations were observed using SEM. As shown in **Figure 1-3a**, Porous structures were found in both Col-IV/LM NFs at different thicknesses, which is similar to natural BMs. And the density of nanofilms increased obviously with the concentration increased. Pore size and fiber diameter were quantized using ImageJ software in **Figure 1-3b, c**. There was no significant difference in fiber diameter between nanofilms at different thicknesses, but slightly larger than the fiber size in natural vascular BMs in the range of 24-67 nm.[22] The average pore size of NFs-1000 was 235 nm that increased with the assembly concentration increased because of the increased density, but still much larger than natural vascular BMs. However, it is worth noting that there will be some

unavoidable differences with the nanofilms structure at wet conditions compared with the dry state observed by SEM. Meanwhile, the density of BMs also varies in different tissues. Taken together, these data indicated the potential of Col-IV/LM NFs used as A-BMs.

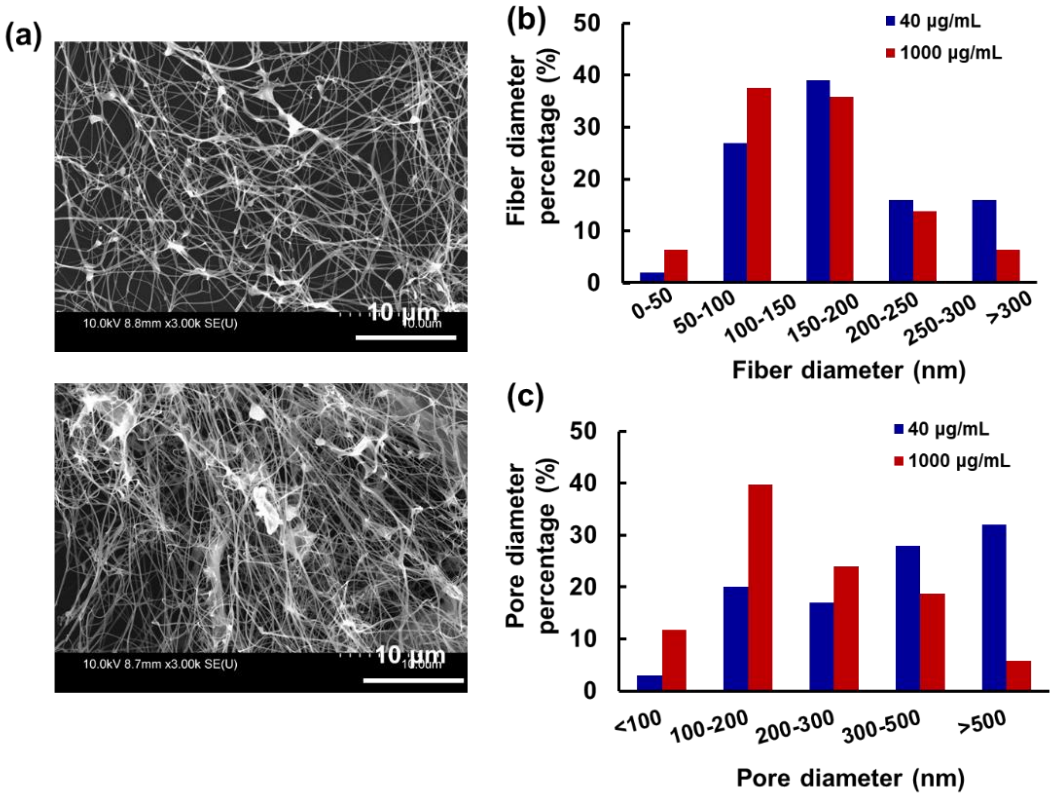

Figure 1-3. (a) SEM images of Col-IV/LM NFs with different thickness. Assembly from proteins concentration at 40 μg/mL (up) and 1000 μg/mL (down). Quantized fiber diameter (b) and pore size (c) of Col-IV/LM NFs from SEM images by ImageJ software. n≥100.

1.3.3 Stability and enzyme-degradation of Col-IV/LM NFs

Next, the weight remaining percentage of Col-IV/LM NFs at various thicknesses in PBS (pH=7.4) buffer solution was evaluated at 37 °C by analyzing frequency change of QCM, which has been reported in our previous paper.[23] As shown in **Figure 1-4**, due to the larger amount, nanofilm at 1000 μg/mL showed an obvious frequency shift increase in the first 5 h and a larger frequency shift decrease within 4 days of incubation. But, by calculation, there was around 13% of the amount increase because of the swelling effect and 20% of the amount decrease maybe because of the removal of unabsorbed proteins or the degradation of proteins. Even after 4 days, still, over 80% of nanofilm weight left and then remained stable. Other

nanofilms with lower concentrations exhibited an almost unchanged frequency shift, demonstrating the stable condition in PBS buffer solution. Considering the previous reports, for the reconstruction of natural BMs, secretion of Col-IV and LM and formation of BMs-like matrix was reported within one week co-culture. Thus, the stable condition in PBS buffer solution within 7 days ensures the application of Col-IV/LM NFs as A-BMs for the fabrication of organized 3D tissues.

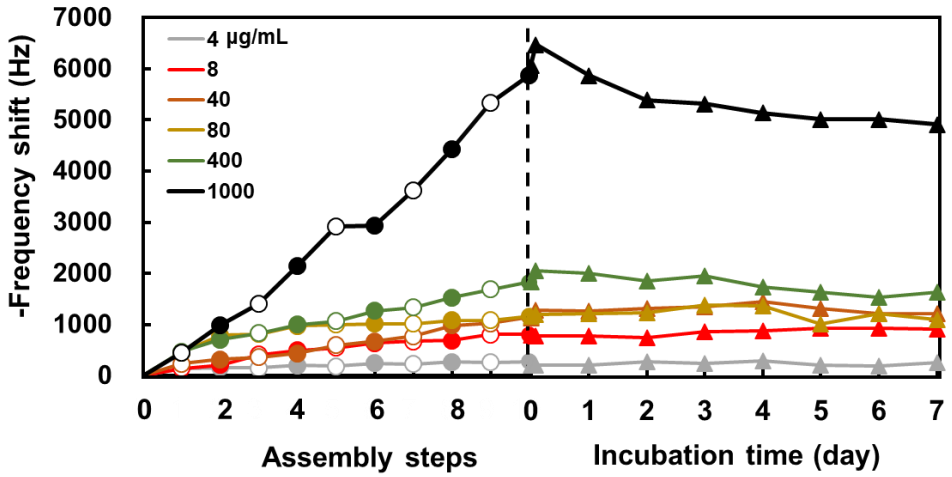

Figure 1-4. Left: Frequency shifts of the QCM stepwise assembly of Col-IV/LM NFs at 37 °C in 50 mM Tris-HCl buffer solution (pH=7.4) with various concentrations of proteins. Right: Stability of different thicknesses of Col-IV/LM NFs in PBS buffer solution (pH=7.4) at 37 °C analyzed by QCM.

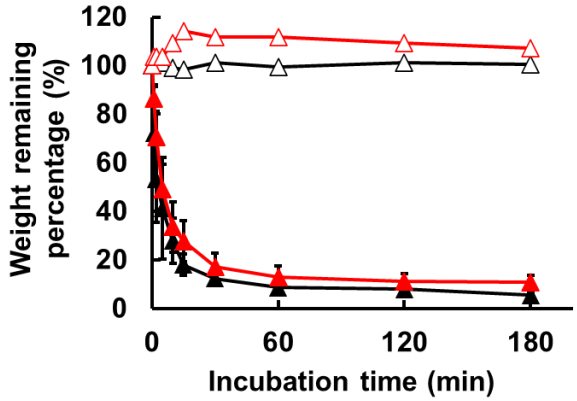

Figure 1-5. Enzymatic degradation of Col-IV/LM NFs with 25 nm obtained from 40 μg/mL (black) and 140 nm obtained from 1000 μg/mL (red) in PBS buffer solution with (solid triangle) or without (hollow triangle) collagenase-IV (100 U/mL, pH = 7.4) at 37 °C analyzed by QCM.

Figure 1-5 shows the enzymatic degradation behaviors of Col-IV/LM NFs in collagenase type IV/PBS solution (pH=7.4, 37 °C). Both of the NFs-40 (25 nm) and NFs-1000 (140 nm)

degraded rapidly and the weight remaining percentage decreased below 10% after 180 min, but kept stable in PBS solution without enzyme. Good stability and biodegradability indicated that Col-IV/LM NFs are suitable for tissue engineering.

1.3.4 Cell adhesion on Col-IV/LM NFs

Since both endothelial and mesenchymal cells are colocalized nearby with an indirect crosstalk and adhere well to the natural BMs, the cell adhesion properties of these two types of cells were evaluated on the obtained A-BMs. Surface wettability of substrate is one of the most critical factors for cell adhesion behaviors. In order to analyze the cell adhesion properties, Col-IV/LM NFs were fabricated on the surface of a polystyrene (PS) substrate that is hydrophobic. Normal human dermal fibroblasts (NHDF) and human umbilical vein endothelial cells (HUVEC) were seeded on the nanofilms surface, as shown in **Figure 1-6a**. Bare PS substrate served as a negative control, which is not suitable for fibroblasts and endothelial cells adhesion. Meanwhile, the tissue culture dish is also made from polystyrene, but treated with plasma to be applicable for tissue culture and referred to as TCPS, served as a positive control. First, water contact angles of various substrates were measured, as shown in **Figure 1-6b**. Compared with TCPS, the PS substrate is more hydrophobic. Significant differences were observed between PS substrate and Col-IV/LM NFs. After LbL assembly of Col-IV/LM NFs on QCM chips, the water contact angle decreased greatly. There was, however, no significant difference between $(Col\text{-}IV/LM)_5$ and $(Col\text{-}IV/LM)_4$-Col-IV NFs, indicating the hydrophilicity of both Col-IV and LM. When cells were cultured for 1 h on the bare PS substrate, few cells could attach to the substrate and all the cells presented a round shape morphology. However, both NHDF and HUVEC adhered well to Col-IV/LM NFs even with only one bilayer. More than 55% of NHDF and 60% of HUVEC adhered to Col-IV/LM NFs after 1 h of incubation, which showed even better adhesion properties than the TCPS substrate with 31% adhesion percentage of NHDF and 20% of HUVEC. Furthermore, after 24 h incubation, 135% of NHDF and 129% of HUVEC adhered well to Col-IV/LM NFs, and displayed their normal fiber-like and cobblestone-like morphologies (**Figure 1-6c**). However, less than 40% of cells adhered to the bare PS substrate, and the poorly adhered NHDF and HUVEC showed strong aggregation

(**Figure 1-6d**). These results demonstrated the good cell adhesion properties of Col-IV/LM NFs because the Col-IV and LM can not only increase the hydrophilicity of the PS substate, but also provide sites for cell adhesion proteins, such as integrin. Enhanced cell adhesion properties of Col-IV/LM NFs demonstrated their possibility to be employed as A-BMs.

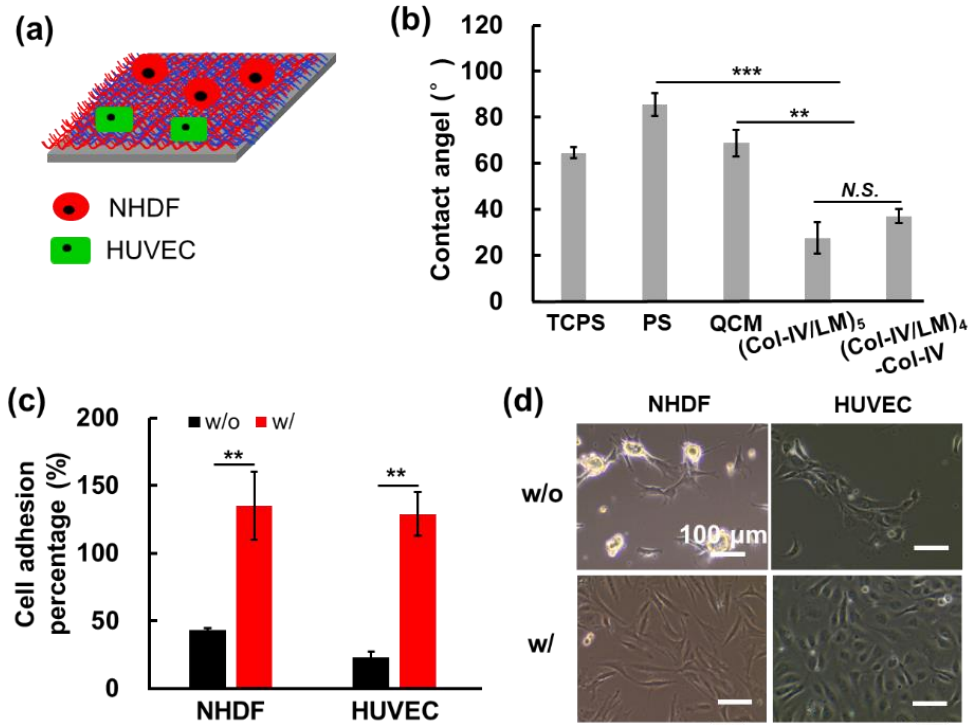

Figure 1-6. (a) Schematic illustration of cell adhesion on Col-IV/LM NFs that were constructed on PS substrate. (b) Water contact angles measured on the surfaces of TCPS, PS, QCM chip, and QCM chips coated with $(Col\text{-}IV/LM)_5$ and $(Col\text{-}IV/LM)_4$-Col-IV nanofilms. n=3. (c) Percentage of adhered NHDF and HUVEC on PS substrate without (w/o) or with (w/) Col-IV/LM NFs after 1 and 24 h incubation. *$p < 0.05$, **$p < 0.01$, and ***$p < 0.001$. (d) Morphology of NHDF and HUVEC adhered on PS substrate coated w/o or w/ Col-IV/LM NFs for 24 h.

Live/Dead cells imaging assessed the viability of cells on Col-IV/LM NFs (**Figure 1-7a**), reaching 99% of viability by calculating the ratio of live and dead cells fluorescence intensity. These results were also confirmed by WST-8 kit assay, compared to TCPS, there were 97% of viability on $(Col\text{-}IV/LM)_1$, 94% on $(Col\text{-}IV/LM)_3$ and 110% on $(Col\text{-}IV/LM)_5$ (**Figure 1-7b**), indicating their biocompatibility used for tissue engineering.

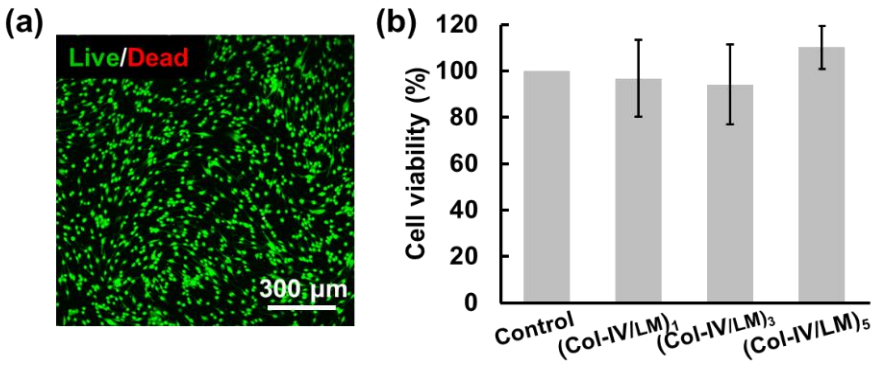

Figure 1-7. (a) CLSM image of living cells stained by Calcein-AM (green) and dead cells stained by Ethidium homodimer III (EthD-III, red). (b) Cell viability of NHDF cultured with Col-IV/LM NFs with various bilayers by WST-8 kit assay. n=6.

1.3.5 Cell migration through Col-IV/LM NFs

Natural BMs play an important role in the separation of different cells and keeping compartmentalization of various tissues or organs. Moreover, BMs are closely associated with cancer cells metastasis and invasion. Therefore, the cell separation property is one of the most critical factors, which is depicted in **Figure 1-8**. The transwell migration assay is usually used to analyze cell invasion ability or response to some chemotactic factors.[24] In this section, Col-IV/LM NFs were prepared on a transwell insert membrane that acted as a control group to compare the barrier effect of Col-IV/LM NFs on preventing cell migration (**Figure 1-8a**). HUVEC, which possess a stronger migration ability compared to NHDF, were used to test the cell separation ability of Col-IV/LM NFs. For the bare insert membrane (3.0 μm of pore), HUVEC migrated easily to the other side through the pores. Migrated cells could be observed after 6 h incubation (**Figure 1-8c, d**), and the migrated cell number percentage increased from 9% to 72% after 48 h incubation (**Figure 4d**). HUVEC migration behavior through the insert membrane was also confirmed by H&E staining, where HUVEC could be observed on both sides of the insert membrane, forming a "sandwich" structure. Compared with the bare insert membrane, Col-IV/LM NFs obtained from 40 μg/mL could prevent a small amount of cell migration in 12 h, but there was no significant prevention effect after 12 h. This maybe because of the thinner membrane at only 25 nm and enzymatic degradation by the cells. We assumed that a much stronger barrier effect would be exhibited with thicker nanofilms. Col-IV/LM NFs

at 140 nm obtained from 1000 μg/mL were measured under the same experimental condition. These thicker NFs prevented cell migration completely for up to 8 h, and showed a better separation ability for up to 48 h, when less than 20% of migrated cells. Based on the preceding analysis, there is plenty of potential for Col-IV/LM NFs with suitable thickness to prevent cell migration and separate different cells or tissues, thus mimicking natural BMs.

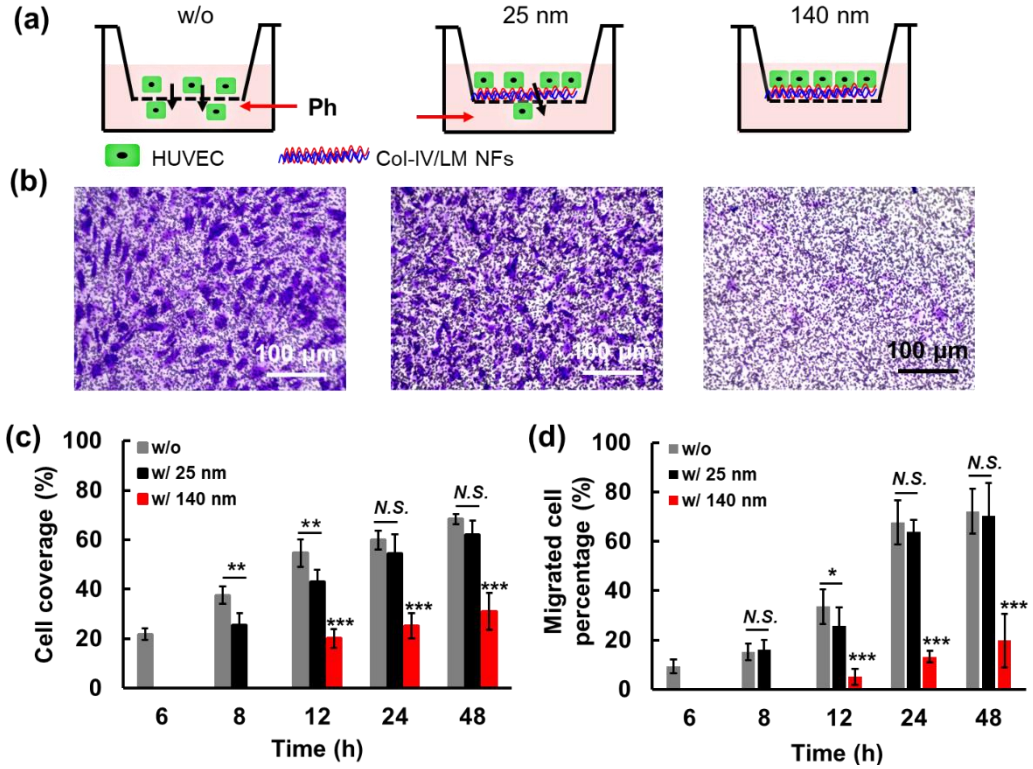

Figure 1-8. Barrier effect on HUVEC of Col-IV/LM NFs coated onto porous membranes (24-well insert with 3.0 μm pore size, 2.0×10^5 cells). (a) Schematic image of HUVEC migrated through the transwell membrane coated w/o or w/ Col-IV/LM NFs. (b) Representative transwell images of crystal violet staining of migrated HUVEC through the transwell membrane coated w/o or w/ Col-IV/LM NFs at 40 and 1000 μg/mL after incubation for 24 h. (c) Migrated HUVEC coverage and (d) HUVEC number on the other side of the transwell membrane calculated by crystal violet staining in 1800×1350 μm. n=3. *$p < 0.05$, **$p < 0.01$, and ***$p < 0.001$.

1.3.6 Cell compartmentalization by Col-IV/LM NFs

In addition, natural BMs distribute between epithelial (endothelial) cells and connective tissues *in vivo*. To further assess the barrier effect of Col-IV/LM NFs between different cells, Col-IV/LM NFs at 140 nm of thickness was placed between NHDF layers and an HUVEC

monolayer, which mimics the structure of natural tissues (**Figure 1-9a**). The location of Col-IV/LM NFs was confirmed by the cross-sectional CLSM image (**Figure 1-9b**). Col-IV/LM NFs in green were distributed between the HUVEC monolayer (CD31 stained in blue) and the NHDF layers (CellTracker Deep Red). **Figure 1-9d** shows the morphology of Col-IV/LM NFs at 140 nm, in which Col-IV was conjugated with FAM in green. Meanwhile, such layered structure of two type of cells were also evaluated using histology staining. As shown in **Figure 1-9c**, HUVEC stained with CD31 distributed on NHDF layers, forming patterned cell co-culture structure.

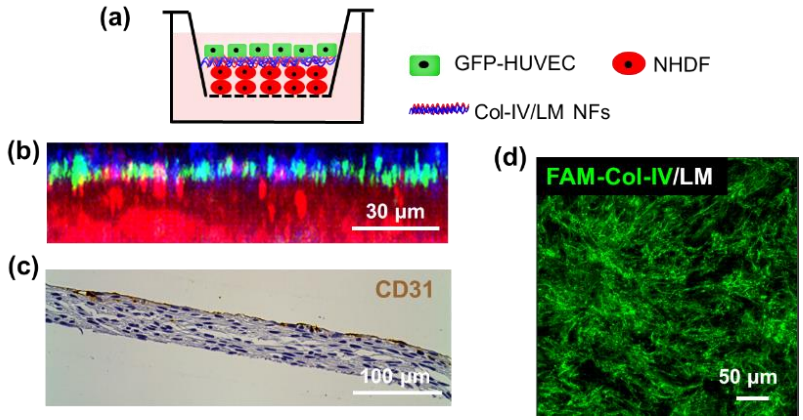

Figure 1-9. (a) Schematic image "sandwich structure" of NHDF and HUVEC co-cultured with the barrier effect of Col-IV/LM NFs. (b) Cross-sectional CLSM image showing the distribution of Col-IV/LM NFs (FAM conjugated Col-IV in green) between the HUVEC monolayer (CD31 immunostained in blue) and NHDF layers (stained by CellTracker Deep Red). (c) Histological observation of a cross-sectioned compartmentalized cells co-culture (HUVEC were stained with CD31, toluidine staining for nuclei). (d) Fluorescence image of Col-IV/LM NFs morphology (FAM conjugated Col-IV in green).

These network structures can not only support adhered cells, but also allow the transport of small signal molecules for hetero-cellular crosstalk, which is similar to natural BMs. At first, HUVEC monolayer was localized hierarchically on the surface of NHDF layers (**Figure 1-10b**), but migrated into NHDF layers quickly within 2 days. However, with the barrier effect of Col-IV/LM NFs between HUVEC and NHDF, the migration of HUVEC was prevented effectively. Without any barriers, HUVEC migrated deeply to over half the depth of NHDF layers in the first 24 h of incubation and even reached to the bottom, forming a random cells mixture on the fourth day. But under the barrier effect of Col-IV/LM NFs, after 2 days of

incubation, HUVEC and NHDF still kept their layered and organized structure. Even on the third day, the depth of HUVEC migration through NHDF layers was still less than 50%, indicating the successful barrier effect of Col-IV/LM NFs (**Figure 1-10c**). After 4 days of incubation, however, HUVEC migrated almost to the bottom. The Col-IV/LM NFs may have been partially degraded by some enzyme secreted by fibroblasts.[25] Despite this, the migrated cell number was still less than that without Col-IV/LM NFs (**Figure 1-10d**), indicating their effective barrier functions.

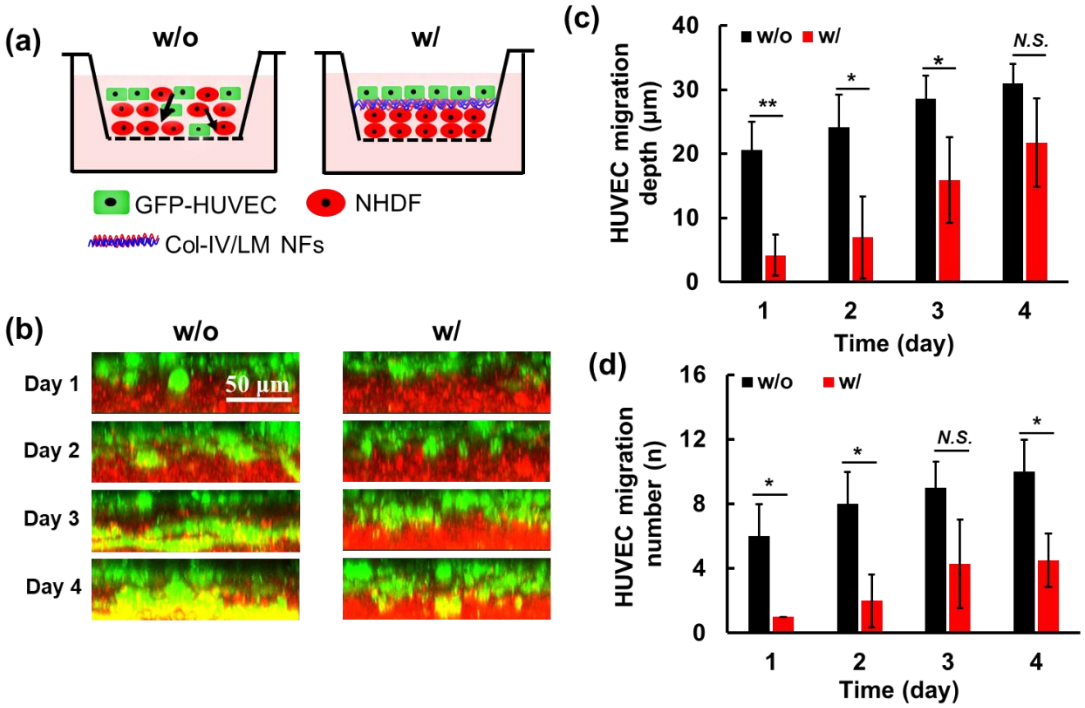

Figure 1-10. (a) Schematic image of random cell co-culture without any barriers and patterned cells co-culture with the barrier effect of Col-IV/LM NFs. (b) Cross-sectional CLSM images of cell migration and mixed cells coculture between GFP-HUVEC and NHDF (stained by CellTracker Deep Red) and cells compartmentalization w/the barrier effect of Col-IV/LM NFs at 140 nm thickness. (c) HUVEC migration depth and (d) Migrated HUVEC number through NHDF layers w/o or w/ Col-IV/LM NFs counted according to the CLSM images of 3D cell aggregation in 400×400 μm. n=3. *$p < 0.05$, **$p < 0.01$, and ***$p < 0.001$.

1.4 Conclusion

In this chapter, all of the results demonstrate the ability of A-BMs based on LbL nanofilms to imitate the structure and biofunctions of natural BMs. Simple operation and materials-versatility of the LbL assembly method enable the fabrication of nanometer-sized films with

controllable components and thickness. The obtained multilayered Col-IV/LM NFs showed adjustable components, thickness, and porous networks that are similar to natural BMs. Cell adhesion on obtained A-BMs was also improved. These multilayered Col-IV/LM NFs permitted the compartmentalized co-culture of fibroblasts and endothelial cells resembling as a physical barrier but allowed cell-cell crosstalk based on their porous microstructure, indicating the potential application of Col-IV/LM NFs as A-BMs, which could be used for the construction of compartmentalized 3D tissues.

1.5 Reference

[1] E. Hohenester, P. D. Yurchenco, *Cell Adhes. Migr.* **2013**, *7*, 56.
[2] E. Poschl, *Development* **2004**, *131*, 1619.
[3] G. Bhave, S. Colon, N. Ferrell, *Am. J. Physiol. Renal. Physiol.* **2017**, *313*, F596.
[4] M. Aumailley, R. Timpl, *J. Cell Biol.* **1986**, *103*, 1569.
[5] K. K. McKee, D. Harrison, S. Capizzi, P. D. Yurchenco, *J. Biol. Chem.* **2007**, *282*, 21437.
[6] T. M. Mundel, A.-M. Yliniemi, Y. Maeshima, H. Sugimoto, M. Kieran, R. Kalluri, *Int. J. Cancer* **2007**, *122*, 1738.
[7] M. Patarroyo, K. Tryggvason, I. Virtanen, *Semin. Cancer Biol.* **2002**, *12*, 197.
[8] J. Borges, J. F. Mano, *Chem. Rev.* **2014**, *114*, 8883.
[9] G. W. Laurie, J. T. Bing, H. K. Kleinman, J. R. Hassell, M. Aumailley, G. R. Martin, R. J. Feldmann, *J. Mol. Biol.* **1986**, *189*, 205.
[10] D. Woodley, C. Rao, J. Hassell, L. Liotta, G. Martin, H. Kleinman, *Biochim. Biophys. Acta* **1983**, *761*, 278.
[11] R. W. N. Nugroho, R. Harjumäki, X. Zhang, Y.-R. Lou, M. Yliperttula, J. J. Valle-Delgado, M. Österberg, *Colloids Surf., B* **2019**, *173*, 571.
[12] A. Nishiguchi, H. Yoshida, M. Matsusaki, M. Akashi, *Adv. Mater.* **2011**, *23*, 3506.
[13] K. Kadowaki, M. Matsusaki, M. Akashi, *Langmuir* **2010**, *26*, 5670.
[14] G. Z. Sauerbrey, Z. Phys. 1959, 155, 206.
[15] Y. Lvov, K. Ariga, I. Ichinose, T. Kunitake, *J. Am. Chem. Soc.* **1995**, *117*, 6117.
[16] G. Perry, W. Xiao, G. I. Welsh, A. W. Perriman, R. Lennon, *Integr. Biol.* **2018**, *10*, 680.
[17] P. D. Yurchenco, H. Furthmayr, *Biochemistry* **1984**, *23*, 1839.
[18] P. D. Yurchenco, E. C. Tsilibary, A. S. Charonis, H. Furthmayr, *J. Biol. Chem.* **1985**, *260*, 7636.
[19] J. T. O'Neal, E. Y. Dai, Y. Zhang, K. B. Clark, K. G. Wilcox, I. M. George, N. E. Ramasamy, D. Enriquez, P. Batys, M. Sammalkorpi, J. L. Lutkenhaus, *Langmuir* **2018**, *34*, 999.
[20] S. L. Clark, M. F. Montague, P. T. Hammond, *Macromolecules* **1997**, *30*, 7237.
[21] F. Zhang, F. Roosen-Runge, M. W. A. Skoda, R. M. J. Jacobs, M. Wolf, Ph. Callow, H. Frielinghaus, V. Pipich, S. Prévost, F. Schreiber, *Phys. Chem. Chem. Phys.* **2012**, *14*, 2483.
[22] S. J. Liliensiek, P. Nealey, C. J. Murphy, *Tissue Eng., Part A* **2009**, *15*, 2643.

[23] Y. Nakahara, M. Matsusaki, M. Akashi, *J. Biomater. Sci., Polym. Ed.* **2007**, *18*, 1565.
[24] S. Iwai, S. Kishimoto, Y. Amano, A. Nishiguchi, M. Matsusaki, A. Takeshita, M. Akashi, *J. Biomed. Mater. Res.* **2019**, *107*, 292.
[25] D. Lindner, C. Zietsch, P. M. Becher, K. Schulze, H.-P. Schultheiss, C. Tschöpe, D. Westermann, *Biochem. Res. Int.* **2012**, *2012*, 1.

Chapter 2

Analysis of Structure and Mechanical Property of Artificial Basement Membrane on Endothelial Cell Functions

2.1 Introduction

Endothelial cells (EC) align on the interior surface of microvasculature and their barrier functions play essential roles in maintaining the integrity of vessels and regulating the selective mass transport between blood vessels and surrounding tissues.[1,2] The rapid endothelialization of EC on implant-blood contacting surfaces has been recognized as essential for improving the long-term biocompatibility of implanted cardiovascular materials, thus avoiding severe complications.[3,4] Hence, understanding the impacts of biomaterials on EC behaviors will contribute to the development of scaffolds for vascular tissue engineering.

All tissues are surrounded by ECM that not only provides physical and mechanical support to cells but also mediates cell behaviors by biochemical signals.[5] To mimic the complicated properties and structures of ECM in the human body, it is suggested that ECM proteins would be the best candidates to support cell survival effectively *in vitro*.[6,7] We developed a multilayered nanofilm in chapter 1 using the main components of BMs, Col-IV and LM, to mimic the structure and bio-functions of BMs *in vitro*. Benefiting from the dense sheet-like network, the Col-IV/LM nanofilm served as an A-BM showed a practical cell compartment effect for organized 3D tissue construction.

In the human body, cells feel mechanical cues from the surrounding microenvironment through the cytoskeleton, and respond to mechanical properties changes by changing their behaviors. Thus, the mechanical properties of A-BMs will greatly influence cell functions. This chapter aims to explore the effects of thickness, roughness and stiffness of Col-IV/LM NFs on EC the functions (**Figure 2-1**).

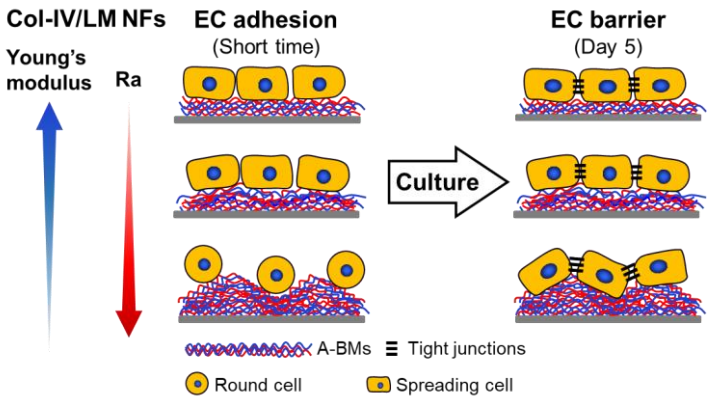

Figure 2-1. Schematic illustration of Col-IV/LM NFs with different Young's modulus and roughness (Ra) and their effects on EC functions.

2.2 Experiments

2.2.1 Materials

Goat anti-mouse Alexa Fluor™ 647 (A21235) and Anti-ZO-1 (Mouse IgG1 anti-human, ZO1-1A12) were purchased from Invitrogen (California, USA). Monoclonal mouse anti-human CD31 antibody was purchased from Dako (M0823, Glostrup, Denmark). Anti-VE-cadherin (rabbit anti-human, ab33168), Anti-claudin 5 (rabbit anti-human, ab131259) and goat anti-rabbit Alexa Fluor™ 488 (ab150077) were purchased from Abcam (Cambridge, UK). Hoechst 33342 was purchased from Thermo Fisher Scientific (Waltham, USA).

2.2.2 Col-IV/LM NFs preparation and characteristics

Col-IV/LM NFs were immersed into TGase/Tris-HCl solution (pH=7.4) containing 5 mM $CaCl_2$ at 37 °C, as describe in chapter 1. Nanofilms obtained from various assembly concentrations were denoted as NFs-4, 40, 200, 400, and 1000, respectively. The morphology and microstructure of the dried Col-IV/LM NFs were observed using an atomic force microscope (AFM, SPA-400, Seiko Instruments Inc., Chiba, Japan). Aluminum coated silicon nitride cantilevers (SII NanoTechnology Inc., Tokyo, Japan) with a resonance frequency of 120 kHz and a nominal spring constant of 10 N/m were used for imaging. For further evaluation of the roughness of the Col-IV/LM NFs, a color 3D laser scanning microscope (VK-9710,

KEYENCE, Japan) was also used to observe the morphology of nanofilms in a dry state. The Young's modulus of Col-IV/LM NFs with various thicknesses were measured by AFM (Nanowizard II BioAFM, JPK Instruments, Berlin, Germany) equipped with a Cellhesion module in wetting conditions. Meanwhile, we compared the Young's modulus of Col-IV/LM NFs assembled on different substrates, including cell culture dish and cell surface. The force-distances curves were acquired using an AFM combined with an inverted optical microscope in Tris-HCl buffer solutions (50 mM, pH=7.4) at room temperature. Monolithic silicon cantilevers (ATEC-Cont, Nanosensors, Switzerland) with a triangular pyramid tip were used to perform 6 times at different positions for one sample. Spring constants (k=0.4 ± 0.2 N/m) were determined using the thermal fluctuation method.[8] The measurement on the cell surface, tip contact positions were controlled on the center of cells. The end-point of force measurement was set at 30 nN, and a constant indentation velocity at 10 N/m was used for both approach and retract processes. Indentation (δ) is obtained by subtracting the deflection (d) to the movement of the piezoelectric ceramic ($\Delta z=z-z_0$) in the z-direction, where z_0 is the contact point. The contact point (z_0) was determined following the method proposed by Domke and Radmacher[9] using an automatic least-squares fitting procedure in the deflection range 10-100 nm.[10] For the Young's modulus (E) calculation follow the Hertz-Sneddon model:[11,12]

$$F=\frac{2E\delta^2\tan\theta}{\pi(1-\nu^2)}$$

where ν is the Poisson's ration of sample, in which the Poisson's ratio of cell was 0.5, and θ (8°) is the half cone angle of the pyramid.

2.2.3 Cell adhesion on Col-IV/LM NFs

Col-IV/LM NFs were prepared in a 24-well plate by the alternate deposition of Col-IV and LM with various concentrations. A tissue culture treated 24-well plate composed of polystyrene was named TC-PS and used as a control substrate. HUVEC (1.0×10^4 cells/cm^2) were seeded onto the obtained nanofilms and transferred to an incubator at 37 °C. After 2 h and 2 days of incubation, the cell culture medium was carefully removed and washed with PBS three times. The adhered cells morphology was observed by FL EVOS Auto microscope. And

the adhered cell number and spreading area were analyzed by ImageJ software. The aspect ratio (L/D) of each cell were measured by ImageJ software, L/D= Length (μm)/Diameter (μm).

2.2.4 Cell proliferation on Col-IV/LM NFs

Cell proliferation of HUVEC cultured on the Col-IV/LM NFs with various thicknesses was evaluated using a WST-8 kit assay. Col-IV/LM NFs were prepared in 96-well plates by the alternate absorption of Col-IV and LM/Tris-HCl (50 mM, pH=7.4) solutions at different concentrations. 100 μL of HUVEC (3.0×10^4 cells/cm^2) were seeded onto the Col-IV/LM NFs. The 96-well plates were then transferred in an incubator at 37 °C for 7 days. Followed by specific intervals of 1, 3, and 7 days incubation, 100 μL of cell count reagent SF/DMEM (1:9, without phenol red) was added to each well. And cells were incubated for a further 3 h at 37 °C. The absorbance of supernatant at 450/600 nm was measured by a microplate reader.

2.2.5 HUVEC monolayer integrity on Col-IV/LM NFs

The Col-IV/LM NFs were prepared in 24-well transwell (pore size 0.4 μm, surface area 0.3 cm^2), as described earlier, by alternate absorption of Col-IV and LM. HUVEC (6.0×10^5 cells/cm^2) were seeded onto the Col-IV/LM NFs and then incubated for 7 days. The culture medium was changed every day.

Trans-endothelial electrical resistance (TEER) measurement: After 1, 2, 3, 5, and 7 days of incubation, the HUVEC monolayers were washed with PBS three times. 200 μL of PBS (room temperature) was added to the upper chamber of the 24-well transwells and 1 mL was added to the lower chamber. The samples were incubated at room temperature for at least 20 min. The integrity of the HUVEC monolayers in the inserts was evaluated using a Millicell® ERS-2 Voltohmmeter equipped with “chopstick” electrodes (Merck Millipore, Massachusetts, USA). Mean TEER values across the HUVEC monolayers were calculated based on the following equation:[13]

$TEER= (R_{HUVEC}- R_{blank})\times M_{area}$ ($\Omega\cdot cm^2$)

where R_{HUVEC} represents the resistance value of HUVEC monolayer, R_{blank} indicates the

resistance value of a naked insert with 0.4 μm pores and M_{area} is the available surface area of the 24-well inserts.

Tight junctions expression: After 5 days of incubation, HUVEC monolayers were washed with PBS three times and fixed by 4% paraformaldehyde (PFA) for 15 min at room temperature. After washing with PBS three times, samples were permeabilized with 0.2% Triton-X 100 and then blocked by 1% BSA/PBS solution for 30 min at room temperature. Primary antibodies were diluted in 1% BSA/PBS as follows: CD 31 (1:50), VE-cadherin (1:900), ZO-1 (1:50) and claudin 5 (1:50). After removing BSA/PBS solutions, the samples were incubated with primary antibodies at 4 °C overnight. After a further three times washing with PBS, samples were incubated into diluted secondary antibodies/1% BSA/PBS solutions, with anti-rabbit Alexa Fluor™ 488 (1:200) and anti-mouse Alexa Fluor™ 647 (1:200). Hoechst 33342 (1:1000) was also used for nuclei staining. Junctional area was obtained by measuring the CD 31, VE-cadherin, ZO-1 and claudin 5 distribution area using ImageJ software. Junctional area of each cell was calculated by dividing the whole distribution area by cell number. And proportion of junctional area to the whole image is the percentage of junction coverage. n=4.

2.3 Results and discussion

2.3.1 Structure of Col-IV/LM NFs with different thicknesses

Studies on biologically specific recognition between Col-IV and LM have reported that LM binds preferentially to Col-IV over other collagens, suggesting they would be the promising candidates for LbL assembly technique. To investigate the effects of the Col-IV/LM NFs thickness and roughness on EC, we prepared a series of nanofilms with various thicknesses. Based on the simple alternate deposition process of Col-IV and LM, the thickness of the Col-IV/LM NFs can be easily controlled at 5.9, 25.6, 26.1, 36.0, and 140 nm by changing the assembly concentrations, 4, 40, 200, 400, and 1000 μg/mL, respectively, which were named as nanofilms (NFs)-4, 40, 200, 400, and 1000.

AFM images evaluated the structures of Col-IV/LM NFs with the increase of assembly concentrations (**Figure 2-2**). Compared with the control sample (tissue-culture treated plate

(TC-PS)), the gradually increased roughness demonstrated the successful assembly of nanofilms, even for low concentrations at 4 and 40 μg/mL. At the higher concentrations of 200 and 400 μg/mL, the assembled nanofilms exhibited a uniform surface morphology and fibrous structure. Due to the specific interaction and self-assembly property of Col-IV and LM *in vitro*,[14,15] the LbL assembly process endows a fibrous but dense microstructure to the Col-IV/LM NFs. At 400 and 1000 μg/mL in particular, the height difference of the nanofilm surfaces reached 81 and 194 nm, in some way, revealing the variation in thickness.

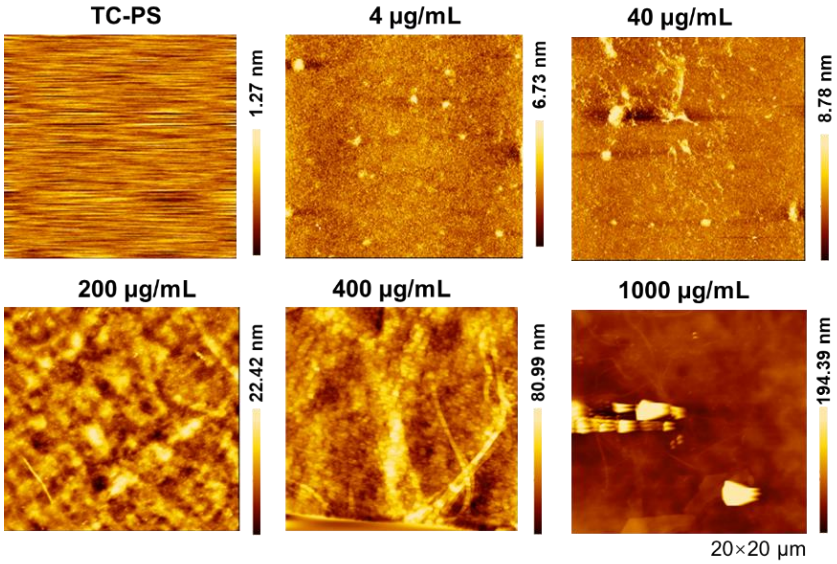

Figure 2-2. AFM images of Col-IV/LM NFs at a dry state obtained from various assembly solutions with different concentrations. A tissue culture-treated plate composed of polystyrene (TC-PS) served as the control sample.

Unlike AFM images that is affected by the AFM tips, color 3D laser scanning microscope can be used to perform a variety of non-contact 3D measurements, which includes surface profile, roughness, 3D, and comparative measurements. Further evaluation of surface scanning of the Col-IV/LM NFs was performed using color 3D laser scanning microscope, as shown in **Figure 2-3**. Similar with the results from AFM, Col-IV/LM NFs obtained from low concentrations had a smooth surface, with lower roughness value (< 100 nm, **Figure 2-3b**). However, the nanofilm surface became increasingly rough with higher assembly concentrations. The roughness of NFs-400 ranged from 100 nm to 1.0 μm, while the value of NFs-1000 surface was above 17.0 μm. Aggregates were clearly observed on NFs-1000, where the height difference even reached 117 μm, which is much larger than the size of a single cell.

This drastic increase of roughness occurred because of the self-assembly of LM at high concentrations.[16–18] These results differed from the nanofilm thicknesses measured in chapter 1 where QCM was used to check the assembly results, probably because of the different substrates and the presence of drying steps using N_2 between each step.

In conclusion, thickness of the Col-IV/LM NFs can be controlled in the range of 4-140 nm on QCM chips, and the surface morphology of the nanofilms was greatly affected by thickness change, whose roughness increased gradually with the increase of assembly concentrations.

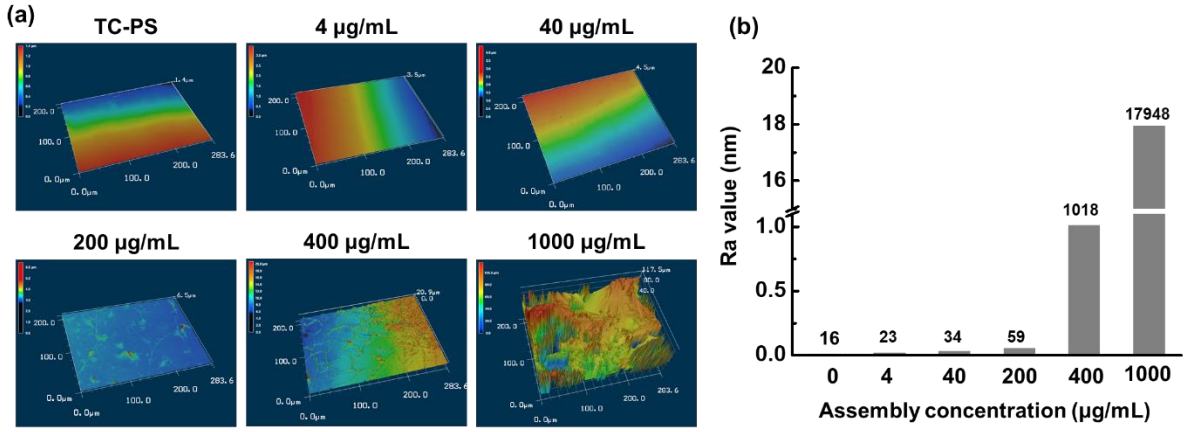

Figure 2-3. (a) Color 3D laser scanning microscopy images of Col-IV/LM NFs at a dry state obtained from various assembly solutions with different concentrations. TC-PS served as the control sample. (b) The arithmetic averages of the roughness profile (Ra) of each nanofilm, which were measured by color 3D laser scanning microscope.

2.3.2 Young's modulus of Col-IV/LM NFs with different thicknesses

The stiffness of Col-IV/LM NFs was evaluated by AFM, as shown in **Figure 2-4**. By simply changing the concentrations of assembly solutions, Col-IV/LM NFs with different thicknesses were firstly prepared on TC-PS to analyze the effects of substrate stiffness on EC functions. Due to the stiff plastic substrate, TC-PS contributed to a rigid substrate for NFs-40 with a thinner surface. Young's modulus decreased with the nanofilms thickness increase because more proteins were absorbed, demonstrating that Col-IV/LM NFs are softer than the plastic substrate. A drastic decline occurred in NFs-1000, corresponding to the results of a higher roughness in **Figure 2-4**, endowing NFs-1000 a much softer surface. Measurements of

different tissues using AFM indicated that the stiffness of BMs varies in four orders of magnitude (0.5 KPa to 5 MPa). In our study, a wide range (0.46 KPa-38 MPa) of Young's modulus was observed, satisfying the requirements for the construction of A-BMs in different tissues.

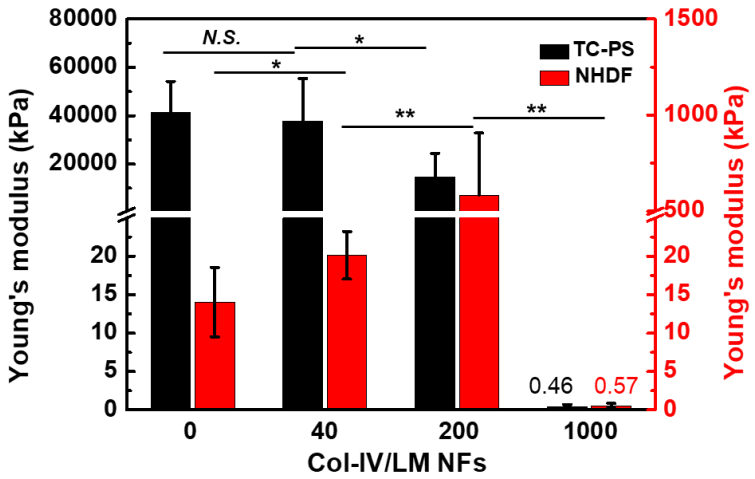

Figure 2-4. Young's modulus of Col-IV/LM NFs constructed on both of TC-PS and NHDF monolayer by the assembly of Col-IV and LM solutions at 40, 200, and 1000 μg/mL, respectively. n=6. *$p < 0.05$, ** $p< 0.01$.

Furthermore, the author also compared the assembly results on different substrates, including TC-PS and NHDF monolayer, because that the requirement in this study is to construct A-BMs in 3D tissue directly. As shown in **Figure 2-4**, a single cell is softer than the plastic substrate, with Young's modulus at 14 KPa. After the deposition of Col-IV/LM NFs, Young's modulus value increased, suggesting that Col-IV/LM NFs are stiffer than cell membranes. However, thicker NFs-1000 on the cell surface has a similar Young's modulus value with the results on TC-PS. This is probably because the thickness of NFs-1000 is wider than the tip indentation distance, representing the stiffness of nanofilms. On the other hand, there is no significant difference in NFs-200 assembled on both TC-PS and cell surface, indicating similar assembly results even on different substrates. Taken together, the stiffness of Col-IV/LM NFs can be easily controlled by changing assembly concentrations to meet the requirements in various tissues. The different substrates of TC-PS and cell membrane didn't make much difference in the assembly of Col-IV/LM NFs.

2.3.3 HUVEC adhesion on Col-IV/LM NFs

It has been reported that chemical and topographical factors have a considerable impact on EC adhesion and phenotype.[19] Owing to the specific recognition of Col-IV and LM with cells, Col-IV/LM NFs were shown to be helpful for fibroblasts and endothelial cell adhesion in chapter 1. However, structure and stiffness of multilayered nanofilms greatly varied with the increase of nanofilm thickness. Thus, HUVEC adhesion on the Col-IV/LM NFs obtained from different assembly concentrations was evaluated, and the quantitative results are shown in **Figure 2-5**. Taking the 2 h-culture results as an example, although no significant difference was observed from the quantitative results of adhered cell density as shown in **Figure 2-5b** and the adhered cell number on NFs-1000 was even higher than that on NFs-40, cells spreading morphology in each group became markedly different. HUVEC adhered to TC-PS, NFs-4 and

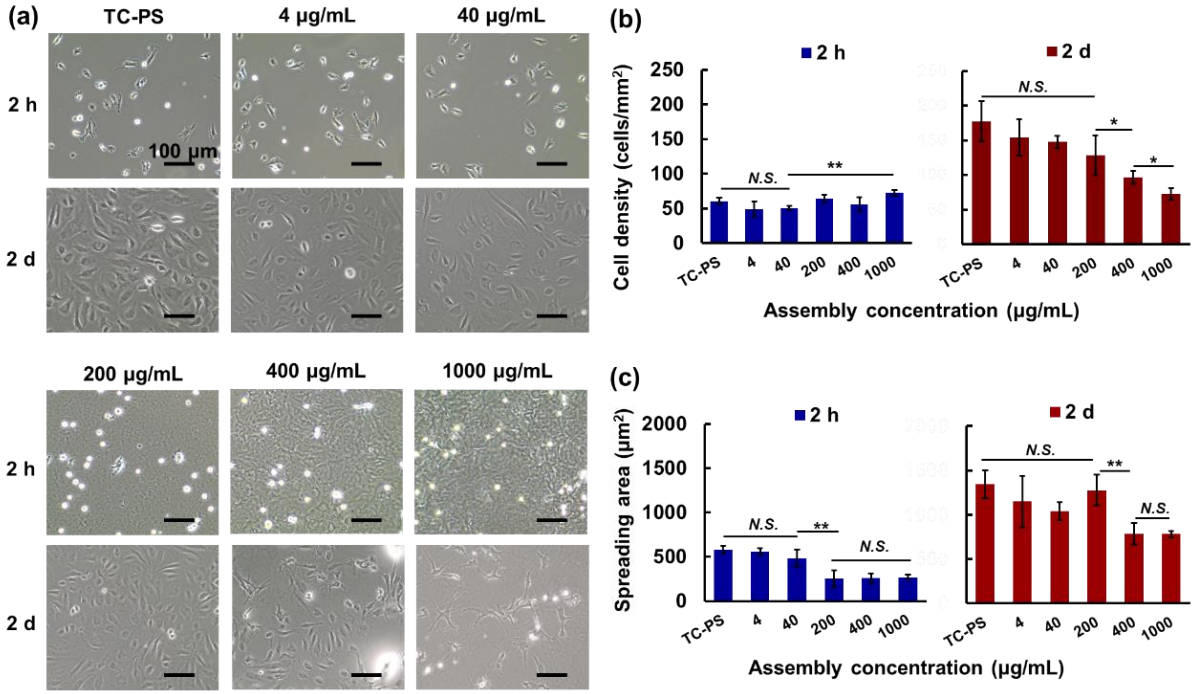

Figure 2-5. **Endothelial cells adhesion on Col-IV/LM NFs.** HUVEC cultured on a TC-PS substrate served as the control sample. Cell seeding density was 1.0×10^4 cells/cm^2. (a) Morphology of HUVEC adhered on Col-IV/LM NFs with various thicknesses after 2 h and 2 days of culture. (b) Adhered cell density of HUVEC and (c) spreading area of each HUVEC cultured on Col-IV/LM NFs with various thicknesses after 2 hand 2 days of culture. n = 3. *p < 0.05, ** p< 0.01, ***p < 0.001.

40 already started to spread on the substrates after a short culture time (2 h), while cells on thicker nanofilms maintained their un-spread state (bright dots in **Figure 2-5a**). In **Figure 2-5c**, the spreading area of each cell on NFs-200, 400, and 1000 after 2 h was clearly lower than other groups because of the un-spread cell morphology. Moreover, after 2 days of culture, HUVEC adhered well to TC-PS, NFs-4, 40, and 200, but still did not adhere well on either NFs-400 or 1000, especially for NFs-1000, showing an elongated shape. Cell density and spreading area on NFs-1000 were also lower than other groups.

To provide further insights into the relationship between roughness and stiffness of the Col-IV/LM NFs and cell adhesion state, the aspect ratio (L/D) of each cell was calculated and then all of the cells were classified into different shapes (**Figure 2-6**). An aspect ratio of 1.0 represents a round shape, indicating poor cell spreading morphology, while L/D ratios over 2.0 suggest a good cell adhesion state. Even after just a short incubation time (2 h), HUVEC started to attach and spread on the substrates. The average of the aspect ratio of cells on NFs-4, 40 was around 2.0, and fewer than 40% of cells were observed to have an aspect ratio of 1.0, while the aspect ratio of all of the cells on NFs-400, 1000 was still 1.0, corresponding well with the cell morphology shown in **Figure 2-5a**. Meanwhile, when the incubation time was extended to 2 days, the increasing aspect ratio on NFs-4, 40, and 200 indicated the spreading cell shape and good adhesion state. However, there were still some un-spread cells (aspect ratio 1.0) on NFs-400 and 1000 after 2 days of culture. Although most of the cells showed an elongated shape in these two samples (**Figure 2-5a**), the morphology of HUVEC was quite different from those on TC-PS. In general, the poor cell adhesion state on NFs-400 and 1000 may relate to the surface morphology and mechanical properties of the Col-IV/LM NFs. LM was demonstrated to show a tendency of self-assembly *in vitro*, especially at high concentrations (over 100 μg/mL), which also enhanced the assembly of Col-IV.[20,21] After the assembly of five bilayers at 37 °C, aggregation of LM at the nanofilm surfaces was clearly observed on NFs-400 and 1000. Even though it's reported EC exhibit a better morphology onto the substrate with submicron-scale roughness than a smooth surface,[22] it was still difficult for EC (~20 μm) to adhere and spread through the oversized barriers. Moreover, cell adhesion and spreading are also suppressed on the softer surfaces. Based on the above results, the author concluded that

the adhesion and spreading morphologies of HUVEC were affected by the roughness of Col-IV/LM NFs, as well as Young's modulus.

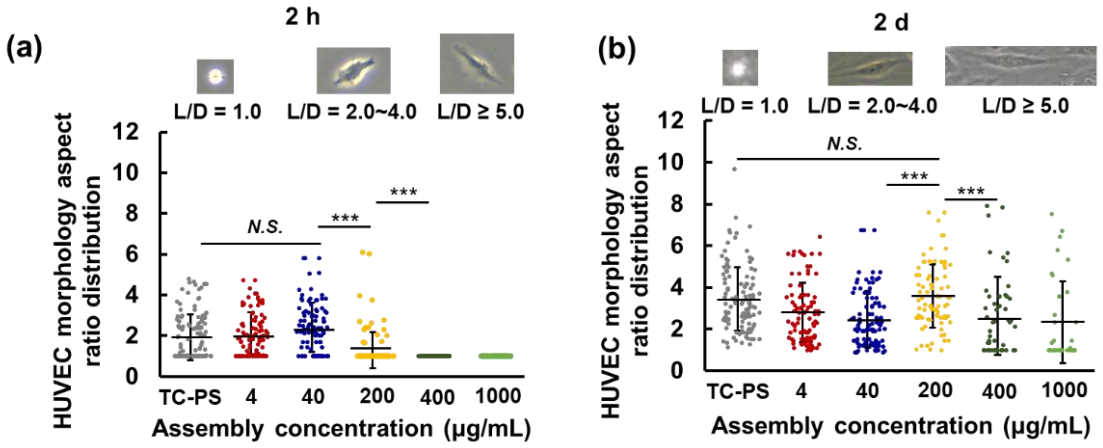

Figure 2-6. HUVEC morphology aspect ratio distribution after (d) 2 h and (e) 2 days of culture was plotted, HUVEC cultured on a TC-PS substrate served as the control sample. Representative images for adhered cell shape are shown at the top of each graph. For 2 h of culture, $n_{Control}$=158; n_4=128; n_{40}=132; n_{200}=167; n_{400}=146; n_{1000}=190. For 2 days of culture, $n_{Control}$=115; n_4=100; n_{40}=96; n_{200}=84; n_{400}=44; n_{1000}=34. ***$p < 0.001$.

2.3.4 HUVEC proliferation on Col-IV/LM NFs

Since the roughness and stiffness of Col-IV/LM NFs have a significant impact on HUVEC adhesion and spreading, proliferation was also investigated as it's one of the most critical cell behaviors (**Figure 2-7**). The proliferation results of HUVEC on NFs-4, 40, 200, and 400 indicated a similar growth ratio with TC-PS (without nanofilms). The proliferated cell number on Col-IV/LM NFs was higher than the control sample, and the cell number also increased gradually with the increase of nanofilm thickness, suggesting an enhanced effect of ECM proteins on cell proliferation. The results on NFs-400 did not agree well with the adhered cell number shown in **Figure 2-5**, probably because of the variation of LbL assembly results. However, the proliferated cell number on NFs-1000 was somewhat lower than other substrates due to the larger roughness which is not ideal for cell adhesion and spreading. In conclusion, Young's modulus and surface morphology of the Col-IV/LM NFs affected by the assembly concentrations account for the different behaviors of HUVEC, including cell adhesion, spreading, and proliferation.

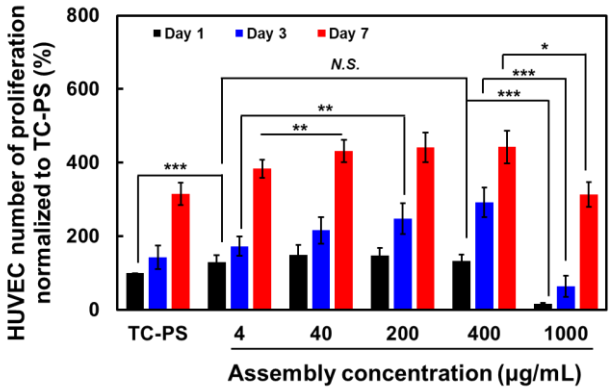

Figure 2-7. Proliferation of HUVEC (3.0×10^4 cells/cm^2) on Col-IV/LM NFs with various thicknesses after 1, 3, and 7 days culture. The cell number is normalized as a percentage of cells adhered to TC-PS at Day 1. *$p < 0.05$, **$p < 0.01$, ***$p < 0.001$.

2.3.5 Integrity of HUVEC monolayer on Col-IV/LM NFs

Alignment of vascular EC lining the inner surfaces of blood vessels contributes to their integrity, controlling the substance exchange between blood and interstitial compartments. The intact EC layer attaches tightly to BMs, which play an essential role in regulating EC functions. Therefore, the integrity of the HUVEC monolayer on A-BMs was evaluated, including interendothelial junction protein expression and trans-endothelial electrical resistance (TEER) value.

Endothelial junctions composed of adherens junctions and tight junctions create adhesive structures between adjacent cells, accounting for a unique EC barrier on the vessel walls.[23–25] As shown in **Figure 2-8a**, interendothelial adhesive proteins, including CD31 and VE-cadherin were clearly observed to be distributed on the margins of cells, demonstrating the development of cell connections. Similar results were also observed for tight junction proteins expression, including ZO-1 and claudin 5. CD31 and ZO-1 were only located on the edge of cell-cell joints, meanwhile VE-cadherin and claudin 5 tended to move to the edge of the cellular surface from the cytoskeleton. It has been demonstrated that uniform and continuous signals of junction proteins on the edge of cell-cell joints suggest an abundance of junction proteins and strong barrier integrity of an endothelial monolayer.[34] Comparing the morphology of intercellular

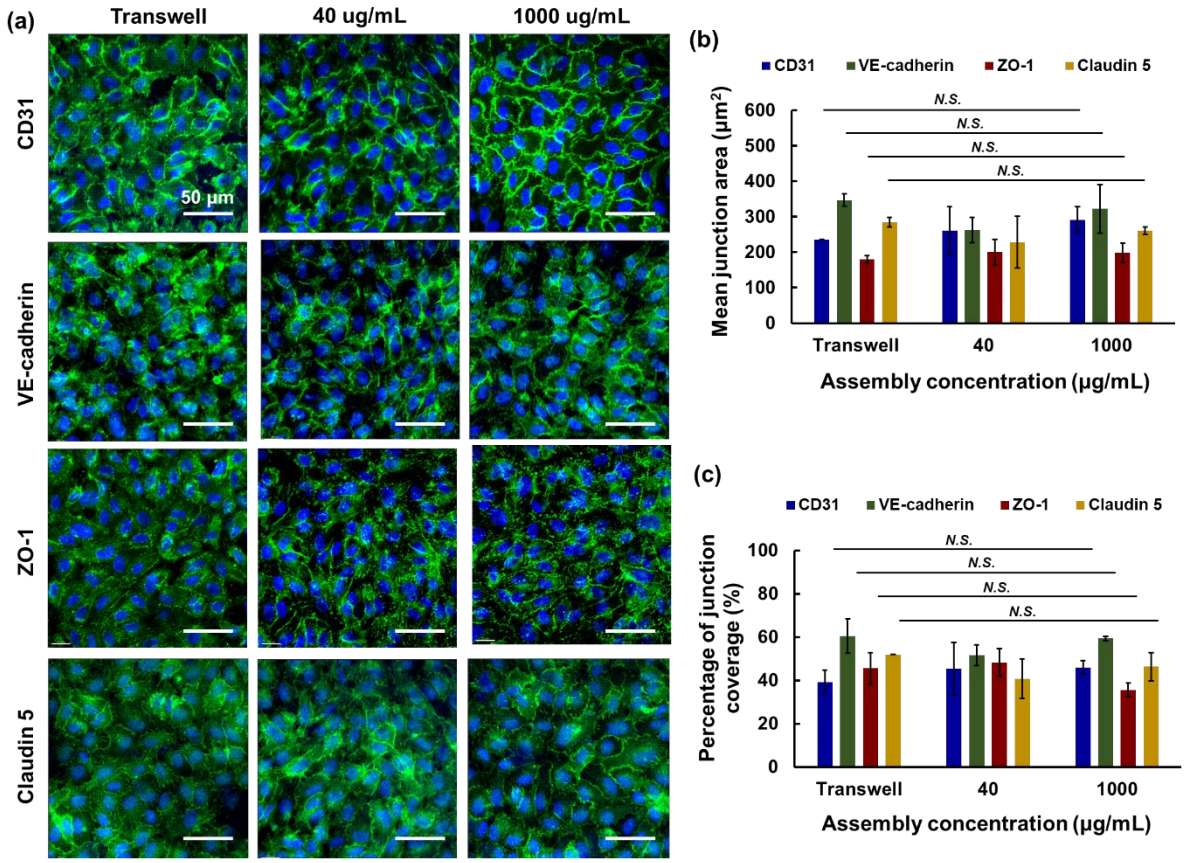

Figure 2-8. (a) Immunofluorescence images of confluent HUVEC on Col-IV/LM NFs with various thicknesses. Cells were labeled for CD31 and VE-cadherin to show the location of adherens junction proteins, and ZO-1, claudin 5 to show the location of tight junction proteins. Nuclei were stained with Hoechst 33342 and are shown in blue. HUVEC monolayer cultured on a naked 24-well insert served as the control sample. Quantitative analysis of (b) intercellular junction coverage area of each cell and (c) percentage coverage area of confluent HUVEC monolayer by analyzing the immunofluorescence intensity in (a). n=4.

junctions in each sample, no significant differences were founded. Owing to the promotion of ECM proteins to the differentiation of EC, the distribution and margin of junction proteins on NFs-1000 were even clearer than those on transwell membranes (**Figure 2-8a**), even though a large fluctuation of HUVEC monolayer was observed on NFs-1000 due to the larger roughness (**Figure 2-9a**). Moreover, by quantitative analysis, the mean interendothelial junction area of each cell and percentage of HUVEC monolayer coverage showed no statistical differences on different substrates (**Figure 2-8b, c**). This result is consistent with the previous studies that EC monolayer on soft substrate displayed higher tight jucntions expression level and stronger integrity.[26,27] Thus, even it's difficult for EC to adhere and proliferate on soft substrate,

followed by adhesion, EC has the tendency to connect with neighboring cells and form confluent monolayer.

However, the confluent EC monolayer formation on NFs-1000 showed different proliferation results to those shown in **Figure 2-7** where the proliferated cell number on NFs-1000 was lower than the other groups after 7 days of culture. Although there were no significant differences of interendothelial junction contact area of HUVEC on different substrates, the spreading area of each HUVEC on NFs-1000 was slightly higher than that on the transwell membrane and NFs-40 (**Figure 2-9b**). Thus, the smaller amount of HUVEC with a larger spreading size were enough to cover the NFs-1000 surface and form a confluent EC monolayer with larger fluctuation. Intercellular junction proteins expression results indicated that HUVEC cannot adhere well to thicker Col-IV/LM NFs due to the soft surface and high roughness, but the thickness or roughness would not affect the barrier functions of confluent HUVEC.

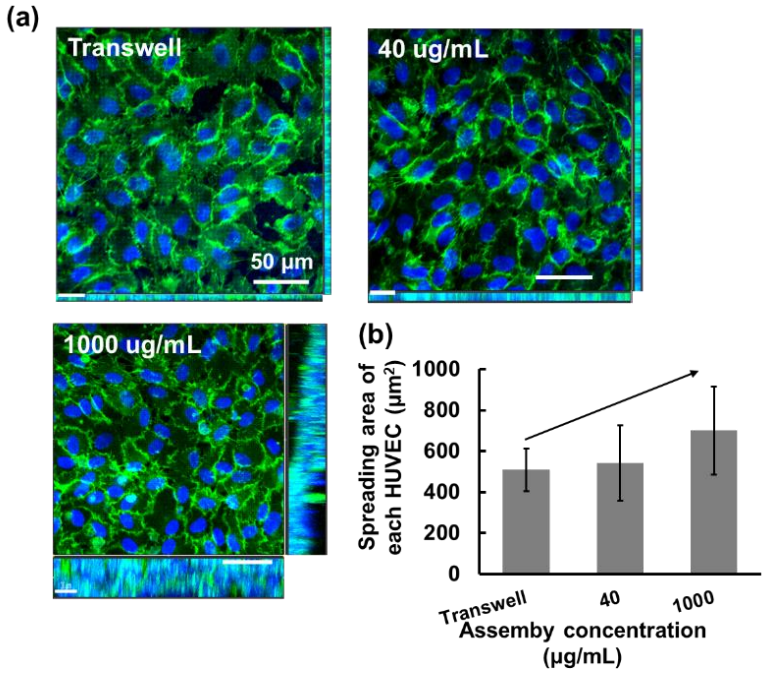

Figure 2-9. (a) Confocal microscopy of confluent HUVEC on Col-IV/LM NFs with various thicknesses. Cells were labeled with CD31 to show the location of tight junction proteins. Transverse images (right and bottom) show the fluctuation HUVEC monolayer, which were broaden by three times, but without change of the length to show the difference in each sample. (b) The coverage area of each HUVEC was measured according to the distribution of CD31 in Figure 2-8a by ImageJ software. n=3.

Unlike the cell adhesion and proliferation on thicker nanofilms, there was no statistically significance difference of intercellular junction protein expression after 5 days of culture between NFs-40 and 1000. The barrier effects of confluent HUVEC on the Col-IV/LM NFs with different thicknesses were further investigated. Integrating the Col-IV/LM NFs into a 24-well transwell insert (0.4 μm pores), the underlying porous insert membrane allowed the measurement of TEER value of confluent HUVEC. As shown in **Figure 2-10**, the TEER values increased gradually over the period of a 5-day culture, suggesting the growing barrier effects of the HUVEC monolayer. Meanwhile, the TEER values of confluent HUVEC cultured on the Col-IV/LM NFs (*e.g.*, 4.0 μg/mL, 39.2 Ω•cm) were remarkably higher than those on the transwell membrane (28.7 Ω•cm) after 3 days of culture. Improved EC barrier function on A-BMs compared with a commercial porous membrane benefits from the specific recognition between Col-IV/LM NFs with cells by integrins.[28,29] However, due to the limited adhesion and proliferation speed on thicker nanofilms, the TEER values on NFs-1000 were much lower than other samples in 5 days. Beyond 5 days of culture, however, no significant differences were found between different nanofilms. Even though HUVEC showed a decreased tendency to adhere and proliferate on the thicker nanofilms, which would affect the formation of the EC monolayer, an increased seeding cell number and extended culture time narrowed this difference.

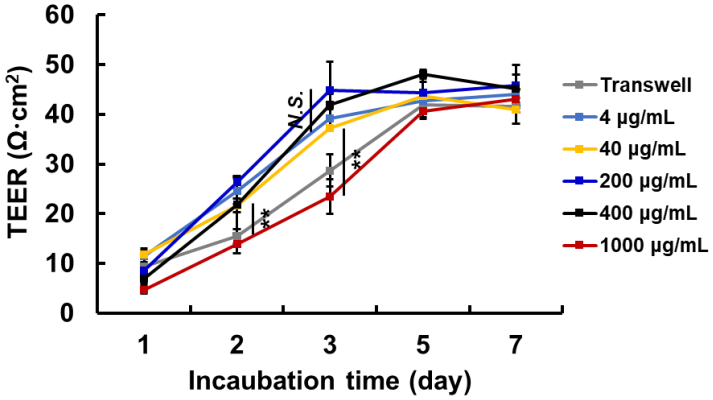

Figure 2-10. The electrical resistance through HUVEC monolayers cultured on Col-IV/LM NFs with various thicknesses was measured over 7 days culture in the 24-well transwell. HUVEC monolayer cultured in a naked 24-well insert served as the control sample. n=3. ** $p < 0.01$.

To investigate the relationship between seeding cell number and the formation of confluent monolayers, the VE-cadherin secretion of HUVEC after 2 and 5 days of culture on NFs-200 and 1000 were compared as shown in **Figure 2-11**, where the initial seeding cell number was 2.0×10^5 in a 24-well insert and around 60 times higher than that shown in **Figure 2-5**. As shown in **Figure 2-11a**, although the confluent EC monolayer did not form at day 2, there were no differences in adhered cell number and the secretion of VE-cadherin on NFs-1000 was even higher than that on NFs-200 (**Figure 2-11b**). After 5 days of culture, VE-cadherin tended to distribute at the joints of adjacent cells, forming the confluent monolayers. The margin of VE-cadherin was clearer and the joints were tighter on NF-200 than that on NFs-1000, but no significant difference of intercellular contact area was observed on different nanofilms (**Figure 2-11b**). Thus, owing to the higher seeding cell number, the adhered cells were sufficient to form confluent HUVEC monolayers, and then improved their barrier functions.

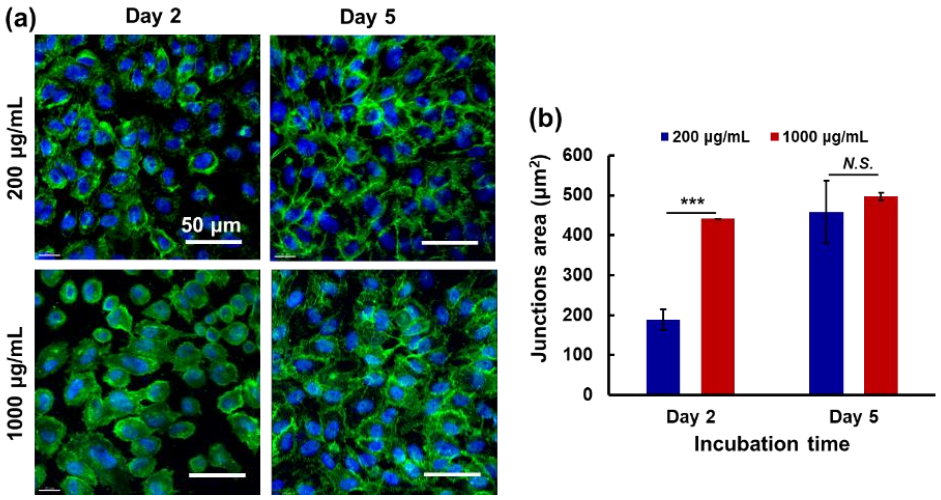

Figure 2-11. (a) Confocal microscopy of HUVEC on Col-IV/LM NFs with different thicknesses at Day 2 and Day 5, respectively. HUVEC were labeled with VE-Cadherin to show the location of junction proteins. (b) Quantification of interendothelial junction coverage area of each cell after 2 and 5 days culture. n≥2. ***$p < 0.001$.

2.4 Conclusion

This study, based on the previous discovery that Col-IV/LM LbL nanofilms can be used as A-BMs to maintain the organized cell co-culture structure, further investigated the effects of

nanofilm structure and mechanical property on the functions of EC. Col-IV/LM NFs stiffness decreased and roughness increased with the increase of thickness. HUVEC behaviors, including cell adhesion and proliferation, varied with the different thickness of nanofilms, *e.g.*, HUVEC could not adhere well to the thicker nanofilms obtained from 1000 μg/mL in a short time (less than 2 days) because of the rough and soft surface. Fortunately, these limitations were overcome by increasing seeding cell numbers and extending the cell culture time. There were no statistically significant differences in EC barrier effects on Col-IV/LM NFs with different roughness. However, in chapter 1, thicker Col-IV/LM NFs contributed to a more substantial barrier effect to maintain cell compartmentalization in 3D tissues. In order to perform the given functions related to the BM in different tissues, a trade-off has to be made between the cell functions and barrier effects when selecting appropriate assembly concentrations.

2.5 Reference

[1] S. Jalali, M. Tafazzoli-Shadpour, N. Haghighipour, R. Omidvar, F. Safshekan, *Cell Commun. Adhes.* **2015**, *22*, 79.
[2] J. A. Wood, S. J. Liliensiek, P. Russell, P. F. Nealey, C. J. Murphy, *Materials* **2010**, *3*, 1620.
[3] H. Zhang, H. Chang, L. Wang, K. Ren, M. C. L. Martins, M. A. Barbosa, J. Ji, *Biomacromolecules* **2015**, *16*, 3584.
[4] Q. Lin, X. Ding, F. Qiu, X. Song, G. Fu, J. Ji, *Biomaterials* **2010**, *31*, 4017.
[5] F. M. R. Witjas, B. M. van den Berg, C. W. van den Berg, M. A. Engelse, T. J. Rabelink, *Stem Cells Transl. Med.* **2019**, *8*, 375.
[6] F. Louis, S. Kitano, J. F. Mano, M. Matsusaki, *Acta Biomater.* **2019**, *84*, 194.
[7] Y. Naka, S. Kitano, S. Irie, M. Matsusaki, *Materials Today Bio* **2020**, *6*, 100054.
[8] A. Yamagishi, M. Susaki, Y. Takano, M. Mizusawa, M. Mishima, M. Iijima, S. Kuroda, T. Okada, C. Nakamura, *Int. J. Biol. Sci.* **2019**, *15*, 1546.
[9] J. Domke, M. Radmacher, *Langmuir* **1998**, *14*, 3320.
[10] L. Richert, A. J. Engler, D. E. Discher, C. Picart, *Biomacromolecules* **2004**, *5*, 1908.
[11] S. Kasas, G. Longo, G. Dietler, *J. Phys. D: Appl. Phys.* **2013**, *46*, 133001.
[12] M. Stolz, R. Raiteri, A. U. Daniels, M. R. VanLandingham, W. Baschong, U. Aebi, *Biophys. J.* **2004**, *86*, 3269.
[13] B. Srinivasan, A. R. Kolli, M. B. Esch, H. E. Abaci, M. L. Shuler, J. J. Hickman, *J. Lab Autom.* **2015**, *20*, 107.
[14] R. W. N. Nugroho, R. Harjumäki, X. Zhang, Y.-R. Lou, M. Yliperttula, J. J. Valle-Delgado, M. Österberg, *Colloids Surf., B* **2019**, *173*, 571.
[15] C. N. Rao, I. M. K. Margulies, L. A. Liotta, *Biochem. Biophys. Res. Commun.* **1985**, *128*,

45.
[16] M. M. S. Barroso, E. Freire, G. S. C. S. Limaverde, G. M. Rocha, E. J. O. Batista, G. Weissmüller, L. R. Andrade, T. Coelho-Sampaio, *J. Biol. Chem.* **2008**, *283*, 11714.
[17] A. Furuyama, K. Mochitate, *J. Cell Sci.* **2000**, *113*, 859-868.
[18] D. YurchencoS, C. Schittny, *J. Biol. Chem.* **1990**, *265*, 3981-3991.
[19] H. Chang, H. Zhang, M. Hu, X. Chen, K. Ren, J. Wang, J. Ji, *Biomater. Sci.* **2015**, *3*, 352.
[20] P. D. Yurchenco, E. Tsilibary, A. Charonis, and H. Furthmayr, *J. Cell Biol.*, **1985**, *260,* 7636.
[21] P. D. Yurchenco, *J. Cell Biol.* **1992**, *117*, 15.
[22] C. Xu, F. Yang, S. Wang, S. Ramakrishna, *J. Biomed. Mater. Res.* **2004**, *71A*, 154.
[23] A. Taddei, C. Giampietro, A. Conti, F. Orsenigo, F. Breviario, V. Pirazzoli, M. Potente, C. Daly, S. Dimmeler, E. Dejana, *Nat. Cell Biol.* **2008**, *10*, 923.
[24] D. Kim, S. Eom, S. M. Park, H. Hong, D. S. Kim, *Sci. Rep.* **2019**, *9*, 14915.
[25] N. Rahimi, *Front. Immunol.* **2017**, *8*, 1847.
[26] H. Chang, H. Zhang, M. Hu, J. Chen, B. Li, K. Ren, M. C. L. Martins, M. A. Barbosa, J. Ji, *Colloids Surf., B* **2017**, *149*, 379.
[27] R. C. Andresen Eguiluz, K. B. Kaylan, G. H. Underhill, D. E. Leckband, *Biomaterials* **2017**, *140*, 45.
[28] J. Song, X. Zhang, K. Buscher, Y. Wang, H. Wang, J. Di Russo, L. Li, S. Lütke-Enking, A. Zarbock, A. Stadtmann, P. Striewski, B. Wirth, I. Kuzmanov, H. Wiendl, D. Schulte, D. Vestweber, L. Sorokin, *Cell Rep.* **2017**, *18*, 1256.
[29] R. Kalluri, *Nat. Rev. Cancer* **2003**, *3*, 422.

Chapter 3

In-situ Crosslinking of Artificial Basement Membrane and Their Size-dependent Molecular Permeability

3.1 Introduction

Natural BMs, serving as physical boundaries, play an essential role in cell alignment and organization,[1] but the molecular transport across such barrier structures is also necessary to control the matter and information exchange between compartments and paracrine communication among cells. The permeability of A-BMs should be studied more systematically and comprehensively in future research. Although theoretical models for selective penetration are well developed,[2,3] they are usually complex and limited to accurately study the penetration kinetics of new drug nanocarriers due to the paradoxical and unpredictable results compared with experimental results.[4,5]

The author introduced a promising A-BM based on Col-IV/LM multilayered nanofilms in the above chapters. Col-IV/LM NFs exhibited good biocompatibility, cell adhesion, and cell compartmentalization ability. However, the developed A-BMs could only provide cell separation for up to 3 days, probably due to the degradation issues. Even though cross-linking is a common way to improve the stability of membranes, including in multilayer films,[6] the cross-linking of A-BMs should be performed after the construction of 3D tissues. Moreover, chemical crosslinking agents, such as formaldehyde, glutaraldehyde, are not available for the crosslinking of A-BMs in 3D tissues due to their strong toxicity.

In this study, the author focused on transglutaminase (TGase) as a biosafe crosslinking promotor for tissue engineering. TGase is a family of structurally and functionally related enzymes that catalyzes the formation of isopeptide bonds between γ- carboxamide groups (-$(C{=}O)NH_2$) of glutamine residue and the ε-amino groups (-NH_2) of lysine residue with subsequent release of ammonia (NH_3).[7] Isopeptide bonds widely exist in the human body,

such as human skin. They are highly stable and resistant to proteolytic degradation, playing an important role in wound healing, blood clotting, and other physiological activities.[8] TGase has been widely used for protein and polypeptide modification in the field of biomaterials.[9–11] Due to the safe catalyzing crosslinking property of the TGase, it may be applicable for the crosslinking of A-BMs in 3D tissues.

In this chapter, the author analyzed the effects of molecular size and conformation on the transport kinetics of molecules through Col-IV/LM NFs. Furthermore, cellular communication between adjacent cells though the barrier of obtained A-BMs was also evaluated. Meanwhile, we tried *in-situ* crosslinking of Col-IV/LM NFs after fabrication on the 3D tissues of NHDF by the addition of TGase to obtain stable A-BMs. To the best of our knowledge, this is the first report on *in-situ* crosslinking of nanofilms in living 3D tissues. Through *in-situ* crosslinking, the A-BMs were stably maintained between endothelial cells and NHDF tissues for at least 5 days (**Figure 3-1**).

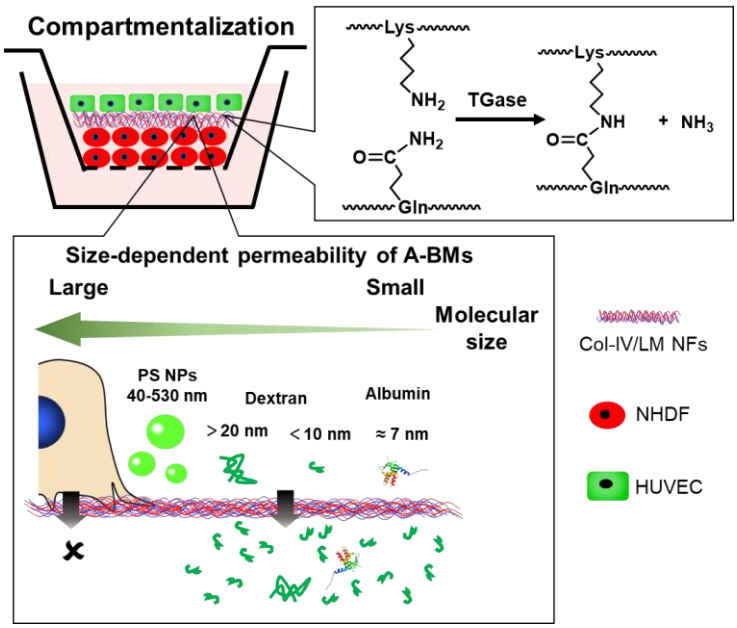

Figure 3-1. Schematic illustration of *in-situ* TGase catalyzed-crosslinking of Col-IV/LM NFs and their permeability for cell co-culture.

3.2 Experiments

3.2.1 Materials

Fluorescein isothiocyanate (FITC)-dextran, 9500 (FD-10S), 230 000 (FD-230S), 2 000 000 (FD2000S-100MG) were purchased from Sigma-Aldrich (Missouri, USA). Nile Red-polystyrene nanoparticles (PS NPs, FP-00556-2, FP-0256-2, FP-0556-2) and tetramethylrhodamine isothiocyanate (TRITC)-albumin were purchased from Spherotech. Crystal violet hydrate was purchased from TCI (548-62-9, Tokyo, Japan). Transglutaminase (1000 U/g) was kindly donated by Ajinomoto Co., Inc. Calcium chloride ($CaCl_2$, 039-00475) was purchased from Wako (Osaka, Japan). Laminin (red fluorescent, rhodamine) was purchased from Cytoskeleton (LMN01-A, Colorado). PureLink RNA Micro Kit and cellTracker Deep Red was purchased from Invitrogen (California, USA). ReverTra Ace qPCR RT Master Mix and Thunderbird SYBR qPCR Mix were purchased from Toyobo (Osaka, Japan).

3.2.2 Crosslinking of Col-IV/LM NFs

Col-IV/LM NFs were immersed into TGase/Tris-HCl solution (pH=7.4) containing 5 mM $CaCl_2$ at 37 °C, as describe in chapter 1. The chemical structure of crosslinked nanofilms was analyzed by a Fourier transform infrared (FT-IR, Spectrum 100, PerkinElmer, MA) spectrometer. Atomic force microscope (AFM, SPA-400, Seiko Instruments Inc., Chiba, Japan) was used to observe the surface morphology of crosslinked Col-IV/LM NFs. Aluminum-coated silicon nitride cantilevers (SII NanoTechnology Inc., Tokyo, Japan) with a resonance frequency of 120 kHz and a nominal spring constant of 10 N/m were used for imaging. The stiffness of nanofilms with or without crosslinking was measured using AFM, following the procedure described in chapter 2. Different with chapter 2, here a sphere tip was used to measure the Young's modulus on cell surface. The relation between Young modulus (E), force (F) follow Hertz-Sneddon model:[12,13]

$$F=\frac{4ER^{\frac{1}{2}}\delta^{\frac{3}{2}}}{3(1-\nu^2)}$$

where R is the radius of sphere, ν is the Poisson's ratio of cells, 0.5, and δ is indentation.

3.2.3 Stability of Col-IV/LM NFs

The stability of crosslinked Col-IV/LM NFs was measured by immersing samples coated onto the QCM chips into DMEM containing 10% fetal bovine serum (FBS, pH=7.4) at 37 °C for 180 min. Frequency shifts of the QCM chips were recorded at intervals. The remaining amount of nanofilms was calculated according to the frequency shifts.

3.2.4 Permeability of Col-IV/LM NFs

Col-IV/LM NFs were fabricated firstly by the alternate deposition of Col-IV and LM in a 24-well transwell with 3.0 μm pores, where the insert bottom served as a supporting porous membrane. Nile Red-polystyrene nanoparticles (PS NPs, 250 μL, 1 mg/mL), fluorescein isothiocyanate (FITC)-dextran (250 μL, 1 mg/mL), and tetramethylrhodamine (TRITC)-albumin (250 μL, 1 mg/mL) solutions were separately added to each upper chamber of the transwell. Blank solvent (1 mL) was added to the lower chamber and then incubated at 37 °C for 24 h. The solutions (10 μL) were collected from the lower chamber at intervals. The fluorescence intensity of the collected solutions was measured by a fluorescence spectrophotometer (FP-8500 WRE, JASCO Corporation), and the amount of transported model molecules was calculated from standard curves. The permeability was evaluated in percentage as compared to the final theoretical equilibrium point. HUVEC (1.0×10^5) was seeded onto the surface of the cross-linked Col-IV/LM NFs and incubated at 37 °C overnight for the formation of an endothelial cell monolayer to evaluate the permeability of Col-IV/LM NFs incorporated with an endothelial cell monolayer. Next, TRITC-albumin solution (250 μL of 1 mg/mL) was added to each well and incubated at 37 °C. Permeability was measured following the above method.

3.2.5 Cell viability

The cytotoxicity of the TGase/Ca^{2+} solution was evaluated by the WST-8 kit assay. Tris-HCl buffer solution was used during the incubation of nanofilms rather than 10% FBS-DMEM containing multiple amino acids and proteins that might be crosslinked by TGase. The cell viability cultured in the TGase/Ca^{2+}/Tris-HCl buffer solution (pH=7.4) was assessed. After the incubation of 100 μL of 1.0×10^4 NHDF in a 96-well plate for 24 h and washing with PBS three times, 100 μL of TGase/Ca^{2+}/Tris−HCl solution was added to each well for 2 h at 37 °C. After PBS washing three times, 100 μL of 10% cell count reagent SF/DMEM (without phenol red) was added. Incubation at 37 °C for a further 2 h was performed, and the absorbance of supernatants at 450/600 nm was then measured by a microplate reader.

3.2.6 Cell migration through crosslinked Col-IV/LM NFs

The barrier ability of crosslinked Col-IV/LM NFs to endothelial cells was analyzed by the transwell invasion assay. Simply, Col-IV/LM NFs were formed in a 24-well transwell with 3.0 μm pores. Also, nanofilms combined with the transwell were immersed into 2 mL of TGase/Ca^{2+}/Tris-HCl solution (pH=3.7, 2.0 U/mL) at 37 °C for 2 h, ensuring the complete cross-linking of both sides of nanofilms. GFP-HUVEC (5.0×10^4) were seeded into each chamber and then incubated at 37 °C for 7 days. After incubation, cells were gently removed by cotton swabs from the upper chamber of the transwell and migrated HUVEC were observed using confocal microscopy (FV 3000, Olympus, Japan). To maintain consistency with the study in chapter 1, migrated HUVEC were also stained with crystal violet (1.0 mg/mL) and examined by a phase contrast microscope (Ph). ImageJ software was used for the analysis of migrated cell numbers.

3.2.7 Cell compartmentalization by crosslinked Col-IV/LM NFs

In order to keep the same organized tissue structures shown *in vivo*, endothelial cells were seeded on the top of the fibroblast layers (**Figure 3-1**). Crosslinked Col-IV/LM NFs serving as barriers were formed between the HUVEC monolayer and NHDF layers. To distinguish the

positions of the two types of cells and nanofilms, NHDF were stained with CellTracker Deep Red and rhodamine-labeled laminin (4%) helped locate nanofilms. Briefly, 300 μL of 1.0×10^6 NHDF was incubated in a 24-well transwell for 24 h to maintain the adhesion of the fibroblast layers. After PBS washing three times, Col-IV and LM were deposited alternately on the NHDF surface for five bilayers and then cross-linked by the TGase/Tris-HCl solution (5.0 U/mL) containing 5 mM Ca^{2+} for 30 min at 37 °C. Next, after washing with PBS three times, 1.0×10^5 HUVEC were seeded on the top of the NHDF layers and incubated with 10% FBS-DMEM/EGM-2 (1:1) mixed solutions for 7 days at 37 °C. Media were changed every day. Co-locations of cells and nanofilms were observed by FV 3000 for a period of 7 days. The results were analyzed by ImageJ software. To compare the cell compartmentalization ability of crosslinked nanofilms (TGase-NFs), un-crosslinked nanofilms (NFs) and control samples without any barrier between HUVEC and NHDF layers were also used to observe the co-locations of two kinds of cells for a period of 7 days. The morphology of NFs and TGase-NFs assembled by FAM-Col-IV were observed by confocal laser scanning microscopy (CLSM) on the surface of NHDF layers.

3.2.8 Cellular communication

1.0×10^6 NHDF were seeded into a 6-well insert and incubated at 37 °C for 24 h for NHDF adhesion completely. After washing with PBS, Col-IV and LM/Tris-HCl solution (1000 μg/mL) were alternately added into the insert, forming Col-IV/LM NFs at the surface of NHDF layers. Following seeding with 1.0×10^6 HUVEC, cells were incubated at 37 °C for 3 days, with medium changes every day. Gene expression was analyzed using real-time quantitative polymerase chain reaction (RT-qPCR). After 3 days of incubation, all samples were washed with PBS. RNA extraction was carried out using PureLink RNA Micro Kit following the manufacturer instructions strictly. RNA content of each sample was measured by Nanodrop spectrometer (N1000, Thermo Fisher Scientific). ReverTra Ace qPCR RT Master Mix was used for reverse transcription to synthesize high quality cDNAs for RT-qPCR. Thunderbird SYBR qPCR Mix was employed to initiate and amplify the cDNA. The cDNA synthesis and RT-qPCR reactions were conducted using the StepOnePlus Real-Time PCR System (Thermo Fisher

Scientific). After preliminary trials, PPIA was employed as the house keeping gene. Results were moreover normalized by VE-cadherin expression.

3.3 Results and discussion

3.3.1 Characteristics of crosslinked Col-IV/LM NFs

Col-IV/LM NFs were prepared by alternate deposition of Col-IV and LM until five bilayers at physiological temperature based on the specific interactions between Col-IV and LM, as described in chapter 1. The interactions of between Col-IV and LM include hydrogen bonding, electrostatic interactions, hydrophobic interactions, and other weak noncovalent interactions.[9,14,15] Thus, the stability of the protein complexes would be affected by salt ions, pH, temperature, and other factors.[16] To mimic the native environment of the human body, stability of the Col-IV/LM NFs, which were immersed in DMEM containing 10% FBS at 37 °C, was quantified by measuring the frequency change using QCM, as reported in our previous studies.[17,18] TGase is an enzyme in nature to catalyze the formation of isopeptide bonds between glutamine and lysine residues (**Figure 3-1**), forming covalent bonds between proteins to enhance the stability of Col-IV/LM NFs. As shown in **Figure 3-2a**, in the first 30 min, the frequency change of NFs decreased rapidly, indicating the disassembly of the Col-IV and LM complex. The calculated results in **Figure 3-2b** show that around 40% of the amount of Col-IV and LM was lost, demonstrating the instability of the Col-IV/LM NFs in 10% FBS-DMEM. After crosslinking by TGase (1.0 U/mL) for more than 30 min, namely, for 2 and 6 h, there was almost no decline in the frequency change of Col-IV/LM NFs immersed in 10% FBS-DMEM for 180 min, suggesting the improved stability of such crosslinked nanofilms. Although stability of the nanofilms was jeopardized in short crosslinking time (< 30 min) because of the lower crosslinking degree, NFs with improved stability could be obtained in short incubation time when the TGase concentration increased to 2.0 U/mL.

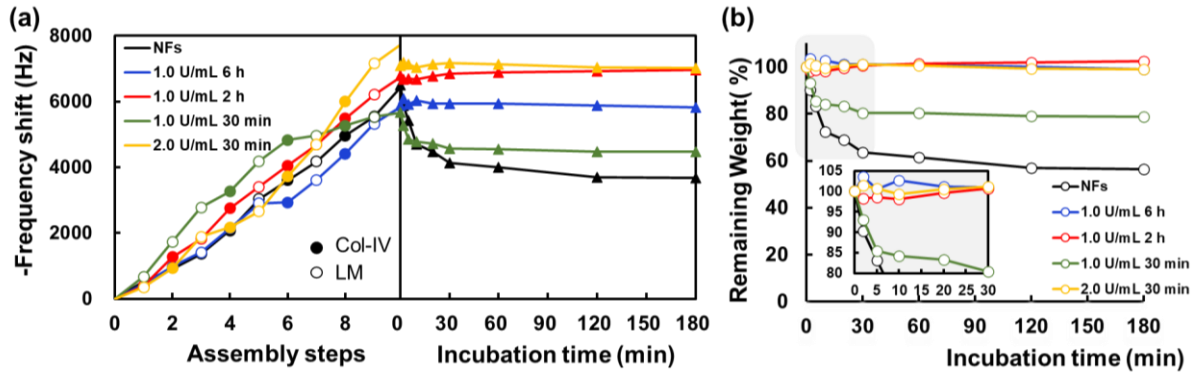

Figure 3-2. (a) Left: frequency shift of the QCM stepwise assembly of Col-IV/LM NFs (1000 μg/mL) at 37 °C in a 50 mM Tris−HCl buffer solution (pH=7.4). Right: stability of crosslinked Col-IV/LM NFs by TGase at 1.0 and 2.0 U/mL for different incubation time in DMEM including 10% FBS at 37 °C analyzed by QCM. (b) Remaining weight percentage of Col-IV/LM NFs crosslinked by TGase at 1.0 and 2.0 U/mL for different incubation time in 10% FBS-DMEM at 37 °C. The inset image shows the weight change of Col-IV/LM NFs incubated for 30 min.

Molecular structure of TGase catalyzed-crosslinked NFs was analyzed by FT-IR spectra, and the characteristic absorption peaks can be clearly identified (**Figure 3-3**). The stretching vibrations of O-H and N-H of NFs appeared at 3301 and 3087 cm^{-1}, respectively. However, the characteristic absorption peak of N-H in TGase-NFs was not clear, indicating the exhaustion of $-NH_2$ because of a reaction between $-NH_2$ and $-(C=O)NH_2$. Moreover, the amide I band corresponding to the stretching vibration of C=O appeared at 1670 cm^{-1}, amide II band at 1553 cm^{-1}, and amide III band at 1257 cm^{-1}, while the absorption peaks of amide groups after crosslinking shifted to higher wavenumbers, especially for the amide I band. These phenomena occurred probably because the formation of covalent bonds weakened the hydrogen bonds of amide groups, suggesting the successful crosslinking of Col-IV/LM NFs.

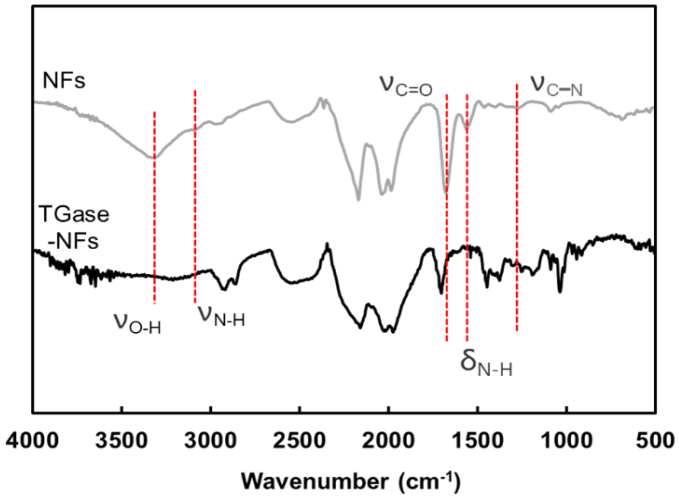

Figure 3-3. FT-IR spectra of Col-IV/LM NFs and TGase catalyzed-crosslinked Col-IV/LM NFs (TGase-NFs, 2.0 U/mL of TGase for 2 h).

Meanwhile, *in-situ* TGase catalyzed-crosslinking of Col-IV/LM NFs preformed on NHDF layers was also analyzed. Firstly, the morphology of Col-IV/LM NFs with or without crosslinking was observed by CLSM (**Figure 3-4**). On NHDF layers, both NFs and TGase-NFs exhibited a fibrous and porous microstructure, and there was no significant difference on the fiber and pore size.

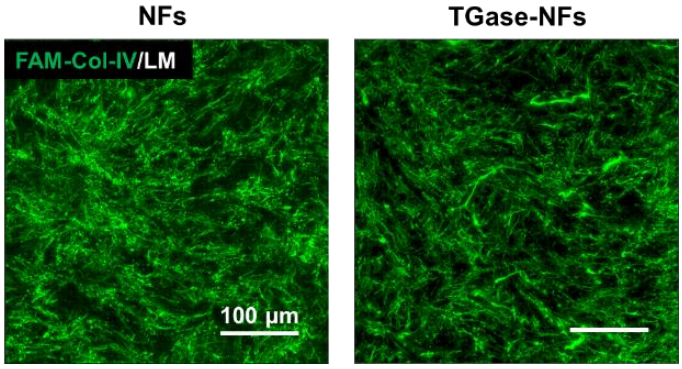

Figure 3-4. CLSM images of FAM-Col-IV/LM NFs with or without crosslinking prepared on NHDF layers (1.0×10^6) in the 24-well insert. The crosslinked nanofilms was prepared by immersing the nanofilms in TGase/Ca^{2+}/Tris-HCl solutions (5.0 U/mL, pH=7.4) at 37 °C for 30 min.

However, the stiffness of crosslinked nanofilms had a clear difference compared with un-crosslinked nanofilms on the cell surface, which were measured by AFM. As shown in **Figure 3-5**, AFM measurement was processed on cell surface by a cantilever with sphere tips. Although the obtained Young's modulus mainly reflect the mechanical property of cell, a clear value increase was found in crosslinked nanofilms, confirming the successful *in-situ* crosslinking catalyzed by TGase.

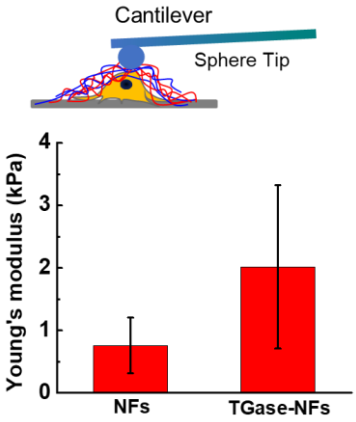

Figure 3-5. Young's modulus measurement of Col-IV/LM NFs with or without crosslinking on NHDF monolayer by AFM. n=6.

3.3.2 Viability of *in-situ* TGase catalyzed-crosslinking

Considering that *in-situ* crosslinking of A-BMs by TGase was performed in 3D tissues, the cytotoxicity of TGase was assessed using the WST-8 kit assay. As shown in **Figure 3-6**, compared with cells cultured in cell culture medium, around 80% of cell viability was

maintained after 2 h incubation with the TGase/Ca^{2+}/Tris-HCl solution (pH=7.4), even in a high concentration of TGase solution at 10 U/mL. Cell viability cultured in PBS for 2 h was also assessed, which even had a lower viability value. This data demonstrated that a slightly lower living cell percentage in TGase/Ca^{2+}/Tris-HCl solution resulted from the absence of cell culture medium, but not the biotoxicity of TGase, suggesting the biocompatibility of *in-situ* TGase catalyzed-crosslinking.

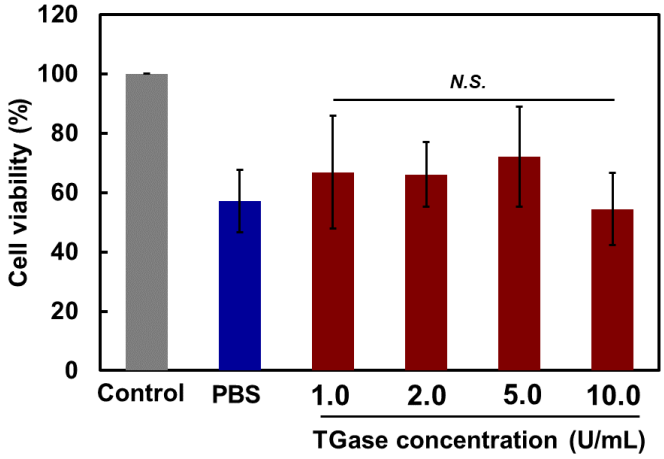

Figure 3-6. Cytotoxicity evaluation of TGase/Ca^{2+}/Tris-HCl solution (pH=7.4) using WST-8 kit assay. NHDF were incubated with TGase/Ca^{2+}/Tris-HCl solution (pH=7.4) for 2 h in the absence of cell culture medium. n=6.

3.3.3 Barrier effects of crosslinked Col-IV/LM NFs on endothelial cells

One of the most important roles of natural BMs is to isolate different cells and maintain the compartmentalized cell/tissue structures. The barrier effect of Col-IV/LM NFs has already been evaluated in chapter 1. Since the stability of nanofilms was enhanced after crosslinking by TGase, the barrier ability of crosslinked nanofilms to prevent endothelial cell migration was also analyzed using a transwell assay. As expected, in the first 24 h, HUVEC migrated easily through the pores of the transwell membrane (3.0 μm) without Col-IV/LM NFs (control), which were found on the underside of the insert after gently removing cells in the upper chamber. However, a few migrated cells were observed with the barrier effect of nanofilms, with only 22 migrated cells/mm^2 across the un-crosslinked Col-IV/LM NFs, while no cell migration through the crosslinked nanofilms (**Figure 3-7b**), indicating their efficient barrier effect to endothelial cells. Even after 48 h incubation, there were still negligible migrated cells

on the underside of the insert combined with TGase-NFs (Figure **3-7c**), and the presence of migrated cells (16 cells/mm^2) through the crosslinked nanofilms was significantly lower compared to that through un-crosslinked nanofilms (145 cells/mm^2, **Figure 3-7b, c**). This finding demonstrated the improved barrier effect of crosslinked Col-IV/LM NFs, benefitting from the improved stability. Meanwhile, no significant differences of cell migration conditions were detected between the un-crosslinked nanofilms and the control sample after 2 days of incubation, which corresponds to the findings in chapter 1. However, migrated cell number through the crosslinked nanofilms was still lower than the un-crosslinked nanofilms after 5 days of incubation, confirming the aforementioned improved barrier effect. Migrated cells were also stained with violet crystal (CV) following the traditional transwell assay, showing a similar tendency in cell migration with that observed in the fluorescence images (**Figure 3-7c**). The obtained nanofilms, serving as A-BMs with higher stability, will find great applicability in preventing cell migration and achieving cell compartmentalization in 3D tissue models.

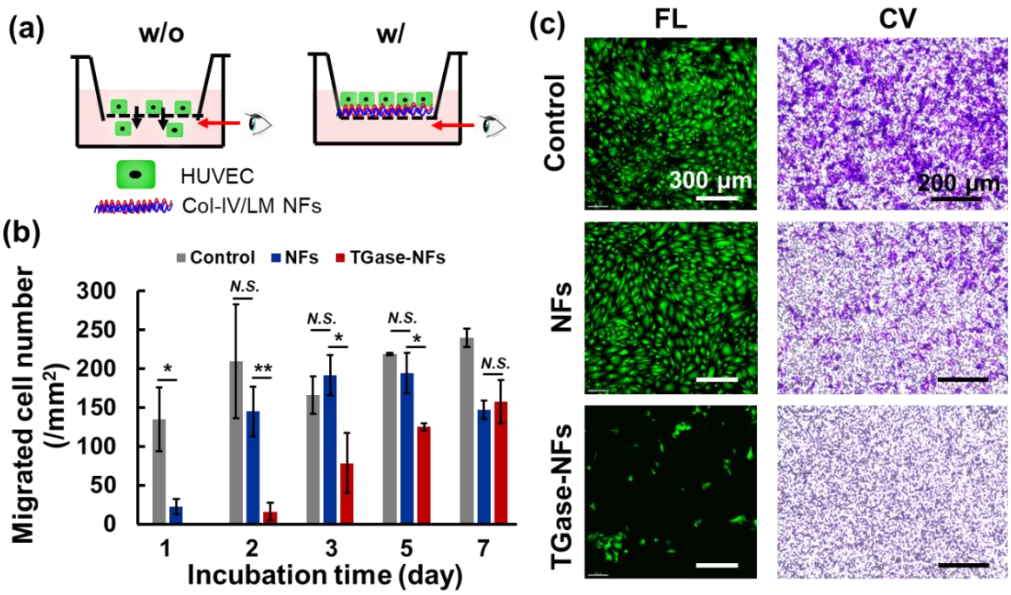

Figure 3-7. (a) Schematic image of GFP-HUVEC migration through transwell membrane (3.0 μm) coated with or without TGase catalyzed-crosslinked Col-IV/LM NFs (TGase solution was controlled at 2.0 U/mL, incubating the nanofilms for 2 h). (b) Migrated HUVEC number on the underside of the transwell membrane calculated by ImageJ software according to fluorescence images. The control sample is a transwell membrane with 3.0 μm pores. n=3. *p < 0.05, **p < 0.01. (c) Representative fluorescence (FL) images and crystal violet (CV) staining images of migrated GFP-HUVEC through the transwell membrane coated with or without TGase catalyzed-crosslinked Col-IV/LM NFs after incubation for 2 days.

3.3.4 Cell compartmentalization by crosslinked Col-IV/LM NFs

To further evaluate the potential of the crosslinked Col-IV/LM NFs acting as A-BMs, a "sandwich" structure was constructed by placing Col-IV/LM NFs between a GFP-HUVEC monolayer and fibroblast layer (CellTracker Deep Red labeled), as shown in **Figure 3-1**. The barrier ability of crosslinked nanofilms to maintaining cell compartmentalization was evaluated in **Figure 3-8**. At the initial stage, the patterned structures of GFP-HUVEC, Col-IV/LM NFs (rhodamine-labeled LM), and NHDF layers were confirmed. As shown in **Figure 3-8a**, the sandwich structure was still maintained at Day 1 in formulations. As the incubation time increased, without any barrier (control), HUVEC migrated gradually into the NHDF layers with a growing migration cell number (**Figure 3-8e**) and migrated depth (**Figure 3-8f**). This phenomenon was clearly observed in the confocal microscopy images at Day 5 in **Figure 3-8a**, where HUVEC migrated to the bottom of the 3D tissue, forming random cell mixtures with NHDF, showing an elongated shape with some interconnections. Un-crosslinked Col-IV/LM NFs exhibited a practical barrier effect to stop HUVEC migration until day 3, and obvious decreases of both the migrated cell number and migrated depth were confirmed compared with control sample. However, after 3 days of incubation, the Col-IV/LM NFs without crosslinking could no longer maintain the organized structures, with around 31 migrated cells/mm^2 entering the 3D NHDF tissues, while less than 4 migrated cells/mm^2 crossing the cross-linked nanofilms (**Figure 3-8e**). Furthermore, as shown in **Figure 3-8b**, HUVEC migrated through the un-crosslinked nanofilms at Day 5, forming mixed structures with NHDF. However, benefitting from the enhanced stability of crosslinked nanofilms (TGase-NFs), the migration of HUVEC was successfully prevented for up to 5 days of incubation. Cell compartmentalization between HUVEC and NHDF was still maintained with a negligible migration distance across the enhanced barrier (**Figure 3-8b**).

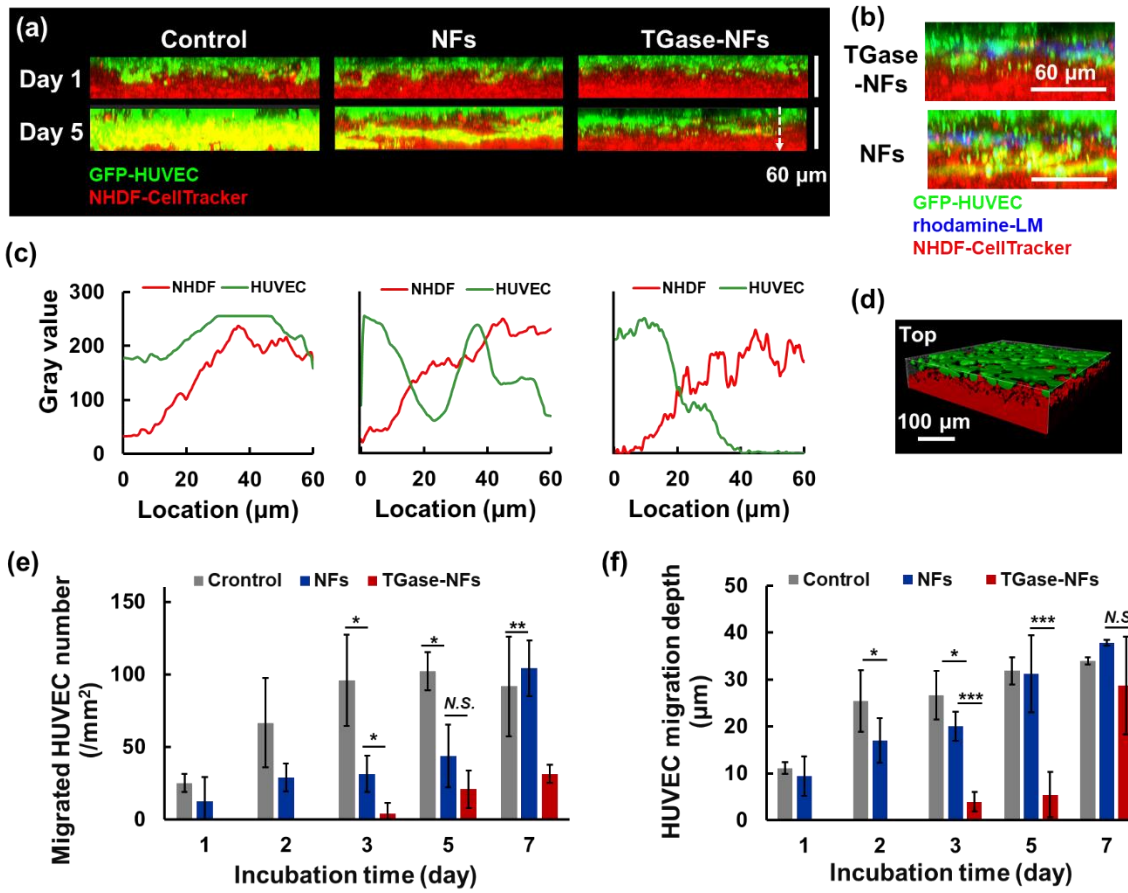

Figure 3-8. (a) Cross sectional CLSM images of patterned cells cocultured with or without the barrier effect of cross-linked Col-IV/LM NFs (the nanofilms were incubated in TGase/Ca^{2+}/Tris-HCl solutions at 5.0 U/mL for 30 min). Comparison of the migration path of GFP-HUVEC through NHDF layers (stained with cellTracker Deep Red) after 5 days of incubation. (b) Relative positions of GFP-HUVEC, NHDF, and Col-IV/LM NFs (LM was labeled with rhodamine-red) with or without TGase cross-linking after 5 days of incubation. (c) Linear scanning of the average intensity profile of GFP-HUVEC and NHDF on day 5 from the top (0 μm) to the bottom (60 μm) following the white arrow in the CLSM images of (a). n=3. (d) 3D reconstructed CLSM images of patterned cultured GFP-HUVEC and NHDF. (e) Migrated HUVEC number through NHDF layers with or without cross-linked Col-IV/LM NFs after 7 days of incubation counted according to CLSM images of patterned cultured cells. n=3. (f) Migration depth of HUVEC through NHDF layers with or without cross-linked Col-IV/LM NFs after 7 days of incubation counted according to the CLSM images of pattered cultured cells. n=3. *$p < 0.05$, **$p < 0.01$, ***$p < 0.001$.

For an intuitive illustration of the relative positions of HUVEC and NHDF in the 3D construction at Day 5, the fluorescence intensity of both types of cells were calculated from the top (0 μm) to the bottom (60 μm), as shown in **Figure 3-8c**. In the three groups, NHDF always

stayed at the bottom, but the fluorescent signal of HUVEC spread over the entire structures in the control sample and un-crosslinked nanofilms. However, with the barrier effect of crosslinked Col-IV/LM NFs, the fluorescence signal of HUVEC was just kept to around 20 μm from the surface, suggesting the successful cell compartmentalized structures. Meanwhile, 3D construction with crosslinked nanofilms was also simulated using Imaris software to clearly show the compartmentalized structure in **Figure 3-8d**. By quantitative comparison (**Figure 3-8f**), after 5 days of culture, only around 5 μm of migration depth was observed through the crosslinked nanofilms, while 31 μm of migration depth (reaching to the bottom) was observed through the un-crosslinked nanofilms, demonstrating that the barrier ability of the Col-IV/LM NFs as A-BMs was improved by TGase catalyzed-crosslinking.

Furthermore, it is still hard to tell the difference between crosslinked and un-crosslinked nanofilms from the cross-sectional images in **Figure 3-8b**. To understand the relationship between preventing cell migration and the stability of nanofilms during cell culture, the remaining amount and the morphology changes of Col-IV/LM NFs are summarized in **Figure 3-9**. In contrast to the rapid decline of un-crosslinked nanofilms, the remaining amounts of TGase-NFs were still kept at approximately 89% at Day 3 and 76% at Day 5. Meanwhile, more defects of un-crosslinked nanofilms were observed (**Figure 3-9b**), probably because of the degradation by the proteases secreted by fibroblasts,[19] while crosslinked nanofilms still kept relatively intact structures. What's more, a video displayed the HUVEC migration routes and the morphology of nanofilms cultured with cells, where the large pores in NFs matched with the HUVEC migration routes, but intact TGase-NFs assisted the compartmentalized cell co-culture structure. The more intact nanofilms benefit from the enhanced stability by TGase catalyzed-crosslinking and further explain the reasons for the improved barrier effect to keep cell compartmentalization in 3D tissues.

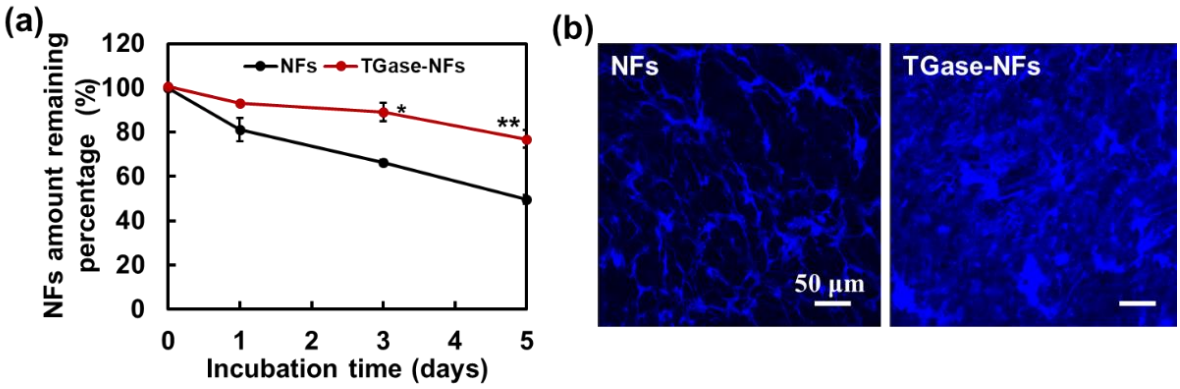

Figure 3-9. (a) Percentage of the remaining amount of Col-IV/LM NFs with or without TGase catalyzed-crosslinking (5.0 U/mL, 30 min). The remaining amount was calculated by comparing the coverage of Col-IV/LM NFs by ImageJ software. All of the data were normalized by NFs at Day 0. n≥1, *$p < 0.05$, **$p < 0.01$. (b) Morphology of Col-IV/rhodamine-LM NFs with or without TGase catalyzed-crosslinking after 5 days of incubation with NHDF and HUVEC.

3.3.5 Permeability Col-IV/LM NFs

BMs have been demonstrated to physically separate cells while allow cell-cell cross talk by administering the transportation of signal molecules.[20] BM is identified as a dense, continuous sheet-like network with nanoscale pores for the "contact" between adjacent cells.[20,21] Therefore, permeability is one of the key properties for natural BMs.

The permeability of the Col-IV/LM NFs was evaluated using a 24-well transwell, fitted with a polycarbonate membrane with 3.0 μm pores that acts as a supporting porous membrane. Polystyrene nanoparticles (PS NPs) with hydrodynamic diameters of 40, 250, and 530 nm; dextran with diameters of 4, 10, and 20 nm; and albumin with a hydrodynamic diameter of 7 nm (**Table 3-1**) were used as template molecules to evaluate the effects of molecular size and conformation on the permeability of Col-IV/LM NFs. As shown in **Figure 3-10a**, the permeability of Col-IV/LM NFs to PS NPs clearly showed a size-dependent behavior, 0.97, 0.74, and 0.53% corresponding to PS NPs-40, 250, 530 nm, respectively, after 4 h incubation. These results exhibit significant differences compared with the polycarbonate porous membrane, demonstrating the blockage effect of Col-IV/LM NFs on PS NPs because of their large size and high rigidity. Similarly, the permeability to dextran-4, 10, and 20 nm also

suggested a size-dependent behavior, corresponding to 26.6, 21.6, and 5.7% of permeability, respectively (**Figure 3-10b, c**). In the case of dextran-4 nm, due to its smaller size, there were no statistically significant differences of permeability with or without the Col-IV/LM NFs after 4 h incubation (**Figure 3-10b**). These results indicated the unimpeded penetration of small signal molecules (such as fibroblast growth factor with 3.8 nm of diameter[22]) through Col-IV/LM NFs, satisfying the requirements of A-BMs for "communication" with adjacent cells. On the contrary, the permeability to dextran-10 and 20 nm clearly decreased compared with that of the bare polycarbonate membrane due to the barrier effect of the Col-IV/LM NFs. Thus, a Col-IV/LM NFs with porous structures acted as a sieve, allowing the passage of the molecules depending on their size across the mesh. In addition to the large size, the stronger electrostatic repulsion between PS NPs and laminin also played an important role in preventing PS NPs penetration than dextran (**Table 3-1**).

Table 3-1. Parameters of template molecules measured in buffer solution (pH=7.4) at room temperature.

Template Molecules	Concentration (mg/mL)	Diameter (nm) Volume	PDI	Zeta Potential (mv)
PS NPs (530 nm)	1.0	531	0.03	-47.2
PS NPs (250 nm)	1.0	396	0.26	-30.3
PS NPs (40 nm)	1.0	37.8	0.08	-67.6
Dextran (2000 kDa)	1.0	19.5	0.56	-11.6
Dextran (230 kDa)	1.0	10.1	0.35	-12.5
Dextran (9.5 kDa)	1.0	4.2	1.0	-14.1
Albumin	1.0	7.0	0.1	-20.2

Taking dextran-20 nm as an example, the effect of nanofilm thickness on the permeability was also analyzed, as shown in **Figures 3-10d**. By simply controlling the assembly steps with 1, 2, 3, 4, and 5 bilayers, nanofilms with 12, 40, 68, 110, and 140 nm thicknesses were constructed, respectively. As expected, the permeability to dextran-20 nm decreased gradually with an increase of nanofilms thickness. Therefore, from the above-mentioned results, it can be stated that the Col-IV/LM NFs exhibit size-selective permeability that can be easily controlled by adjusting their thickness and thus enable to mimic the various permeabilities of BMs in different tissues.[23,24] Indeed, the molecular permeability of obtained A-BMs varied

with the results *in vivo*, where the cut-off for dextran penetration is around 5.5 nm and albumin cannot permeate BMs, due to the larger pore size (235±147 nm) than natural BMs (38-105 nm). However, it is worth noting that the nanofilm fibers will be swelling at the wetting state, presenting a denser structure compared with the dry condition of the SEM image. And also, note that cells such as endothelial cell barriers also assist in administering molecular permeability.

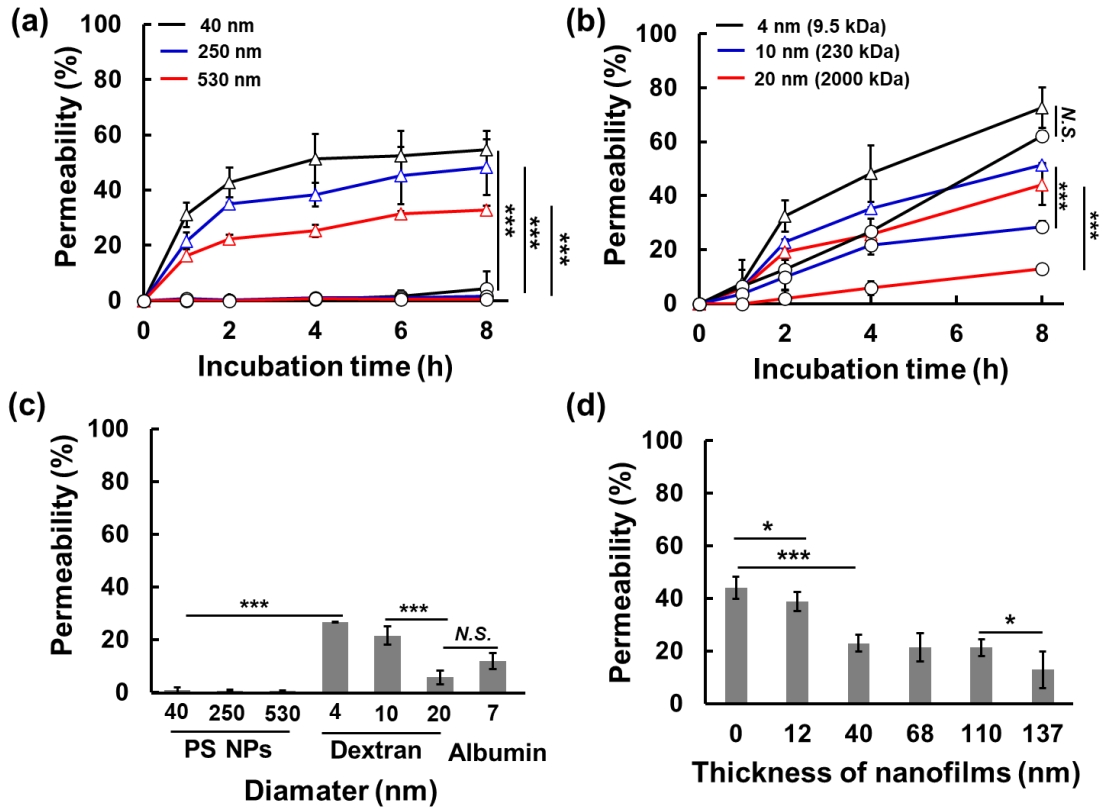

Figure 3-10. Permeability of Col-IV/LM NFs. (a) Nile Red-PS NPs with various diameters and (b) FITC-dextran with various molecular weights penetrated through a porous supporting membrane (24-well transwell membrane with 3.0 μm pores) with (○) or without (Δ) Col-IV/LM NFs at 37 °C for 8 h incubation. n=3. (c) Comparison of the permeability of Col-IV/LM NFs to various template molecules with different diameters after 4 h incubation at 37 °C. n=3. (d) Permeability of Col-IV/LM NFs with different thicknesses to FITC-dextran (20 nm, 2000 kDa) after 8 h incubation at 37 °C. n=3. *$p < 0.05$, **$p < 0.01$, ***$p < 0.001$.

Unlike the soft and random linear polymer molecules, which can entangle like spaghetti, the folded 3D structure of albumin is maintained in the physiological environment.[25] The hydrodynamic diameter of albumin is around 7 nm, which is smaller than dextran-10 nm (**Table 3-1**). However, after 8 h incubation, the permeability of Col-IV/LM NFs to albumin was 16.5%,

much lower than that of dextran-10 nm (28.5%). Meanwhile, no statistically significant differences were found between albumin and dextran-20 nm (12.9%), probably because of the different molecular conformation. On the other hand, even though both albumin and LM have negative charges (**Table 3-1**), interactions (*e.g.*, hydrogen-bonding and hydrophobic interactions) usually exist between proteins. Considering the interactions between albumin and the Col-IV/LM NFs, the concentrations of albumin remaining in the upper and lower chambers of the transwell were measured. Compared with the initial amount of albumin, there was still around 16.8% albumin lacking after the cumulative measurements of the upper and lower chambers (**Figure 3-11**), which was probably associated with the entrapment by Col-IV/LM NFs. Likewise, the penetration of dextran-20 nm was also analyzed. However, no dextran-20 nm was lacking. Thus, the physicochemical properties of the molecules also have an impact on their permeability. Further investigation into the deeper and more comprehensive penetration mechanisms is warranted. Independently of the transport mechanisms of albumin, the size selective permeability of the Col-IV/LM NFs was confirmed in this chapter.

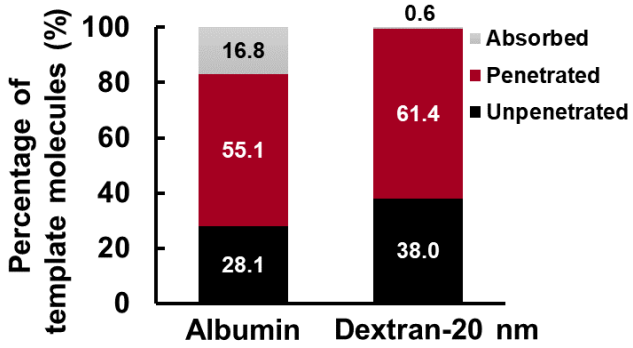

Figure 3-11. Percentage of penetrated, unpenetrated and absorbed albumin and Dextran-20 nm through Col-IV/LM NFs, incubated at 37 °C for 8 h.

Moreover, the effect of crosslinking on the permeability of the Col-IV/LM NFs was evaluated using albumin as a model molecule (**Figures 3-12a**). Under the optimized conditions described in **Figure 3-2**, Col-IV/LM NFs were crosslinked by TGase at various concentrations (1.0, 2.0, 5.0, 10.0 U/mL) for 2 h, ensuring the stability of the nanofilms. As shown in **Figure 3-12a**, the permeability of nanofilms to albumin clearly increased after crosslinking, especially for TGase solutions at 1.0 and 2.0 U/mL. These results may be related to the pore size change of the Col-IV/LM NFs after crosslinking. Assessing the structure of crosslinked nanofilms by

AFM, and pore sizes were measured using Image J software. The author found that even though there was no significant difference of nanofilms microstructure between crosslinked nanofilms, the pore sizes still tended to increase with the increase of TGase concentrations. However, with the TGase concentration further increase to 5.0 and 10.0 U/mL, the permeability level of crosslinked nanofilms decreased compared with that at 2.0 U/mL. This result probably because of the increased Young's modulus after crosslinking (**Figure 3-5**). Penetrated molecules will encounter more resistance through stiffer networks. Therefore, to perform the given functions related to the BM in different tissues, a tradeoff has to be made between the permeability, stability, and appropriate cross-linking degree.

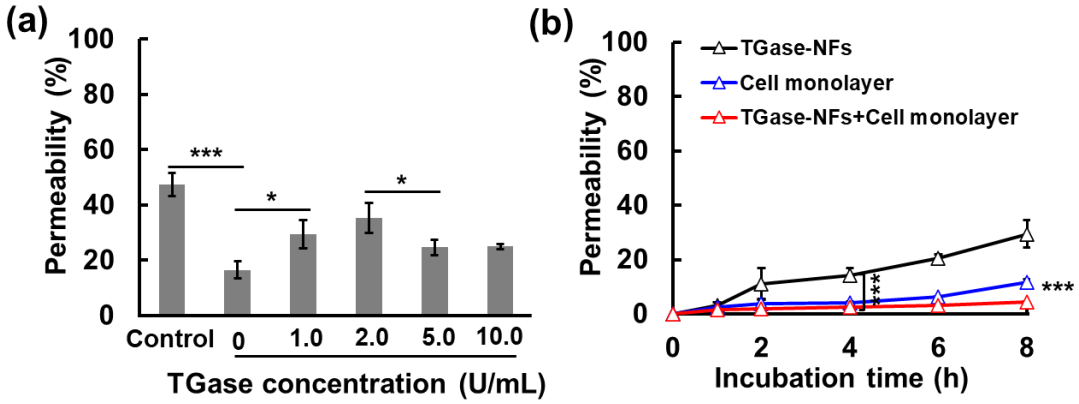

Figure 3-12. (a) Permeability of Col-IV/LM NFs with or without (control) TGase cross-linking (1.0, 2.0, 5.0, or 10.0 U/mL) for 2 h to TRITC-albumin after 8 h incubation at 37 °C. n = 3. (b) Permeability of cross-linked nanofilms (cross-linked by 2.0 U/mL of TGase) and endothelial cell monolayers to TRITC-albumin after 8 h incubation at 37 °C. The permeability of TGase-NFs+cell monolayer at 8 h showed significant differences with cell monolayers and TGase-NFs. n=3. *$p < 0.05$, ***$p < 0.001$.

3.3.6 Cell-cell cross-talk through the barrier of Col-IV/LM NFs

In vivo, cell compartmentalization is supported by natural BMs due to their barrier effects. However, natural BMs are not completely enclosed sheet-like nanofilm, but densely fibrous networks with pores that allow the transport of signal molecules, supporting the cross-talk between adjacent cells.[21] Therefore, the transport of signal molecules secreted by cells through A-BMs is another important factor for the construction of compartmentalized 3D tissues. As discussed above, Col-IV/NF NFs had a molecular size-dependent permeability, the cellular

communication between fibroblasts and endothelial cells that were localized on different sides of nanofilms was evaluated in **Figure 3-13**. The author analyzed tight junction protein expression of HUVEC co-cultured with NHDF by RT-qPCR, and compared the gene expression level with 2D HUVEC culture by normalization using VE-cadherin gene expression because this gene is expressed only in HUVEC. Intercellular tight junction proteins including ZO-1, occludin-1, and claudin-4 are crucial for the formation of endothelial barriers, as they regulate cell adhesion and migration.[26] And basic fibroblast growth factor secreted by NHDF was demonstrated to promote endothelial cell-primed angiogenesis.[27] Co-cultured with NHDF, the expression of tight junction proteins and adhesion molecules of HUVEC will be improved. In **Figure 3-13**, compared with 2D HUVEC culture, relative RNA expression values of tight junction proteins were significantly higher. Especially for claudin-4, the expression value was more than ten times higher than 2D HUVEC culture, indicating that the existence of NHDF improved HUVEC cell-cell connection and differentiation. However, there were no significant differences between the co-culture systems of NHDF and HUVEC without or with the physical barrier of Col-IV/LM NFs, suggesting that there was no suppression effect to the cross-talk between NHDF and HUVEC with the barrier effect of A-BMs. These results further demonstrated the potential of Col-IV/LM NFs used as A-BMs for compartmentalized 3D tissue construction *in vitro*.

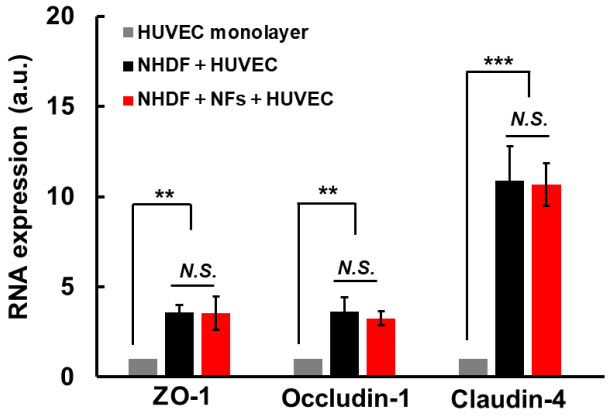

Figure 3-13. RT-qPCR analysis of tight junction protein expression of HUVEC. Tight junction protein expression of HUVEC cocultured with NHDF, which are separated w/o or w/ Col-IV/LM NFs between HUVEC layers and NHDF layers, were compared with simple 2D HUVEC culture. The results were normalized by VE-cadherin gene expression. n=3; $^{**}p < 0.01$ and $^{***}p < 0.001$.

3.4 Conclusion

This chapter introduced a facial way to fabricate robust A-BMs in 3D tissues by the *in-situ* TGase catalyzed-crosslinking. Crosslinked Col-IV/LM NFs were stably maintained between endothelial cells and NHDF tissues, and the permeability of A-BMs remained even after cross-linking. From our experiments on permeability evaluation, the effect of size on permeability was observed by the penetration of PS NPs, dextran, and albumin, showing a size-dependent cutoff property, which agreed well with what is known to occur in glomerular BMs *in vivo*. Notably, the *in-situ* crosslinked Col-IV/LM nanofilms worked well to maintain the compartmentalized cells in a 3D structure for up to 5 days. One can anticipate the possibility of using Col-IV/LM multilayered nanofilms as ABMs for the construction of compartmentalized 3D tissue models.

3.5 Reference

[1] J. Laurent, G. Blin, F. Chatelain, V. Vanneaux, A. Fuchs, J. Larghero, M. Théry, *Nat. Biomed Eng.* **2017**, *1*, 939.

[2] X.-L. Wang, T. Tsuru, S. Nakao, S. Kimura, *J. Membr. Sci.* **1997**, *135*, 19.

[3] R. L. S. Chang, W. M. Deen, C. R. Robertson, B. M. Brenner, *Kidney Int.* **1975**, *8*, 212.

[4] S. R. Pullela, C. Andres, W. Chen, C. Xu, L. Wang, N. A. Kotov, *J. Phys. Chem. Lett.* **2011**, *2*, 2067.

[5] A. Ruggiero, C. H. Villa, E. Bander, D. A. Rey, M. Bergkvist, C. A. Batt, K. Manova-Todorova, W. M. Deen, D. A. Scheinberg, M. R. McDevitt, *Proc. Natl. Acad. Sci.* **2010**, *107*, 12369.

[6] A. I. Neto, N. L. Vasconcelos, S. M. Oliveira, D. Ruiz-Molina, J. F. Mano, *Adv. Funct. Mater.* **2016**, *26*, 2745.

[7] M. Griffin, R. Casadio, C. M. Bergamini, *Biochem. J.* **2002**, *368*, 377.

[8] Mehta, Kapil, and Richard L. Eckert, *Karger Medical and Scientific Publishers,* **2005**, 38.

[9] G. Damodaran, R. Collighan, M. Griffin, A. Pandit, *J. Biomed. Mater. Res.* **2009**, *89A*, 1001.

[10] V. Nele, C. E. Schutt, J. P. Wojciechowski, W. Kit-Anan, J. J. Doutch, J. P. K. Armstrong, M. M. Stevens, *Adv. Mater.* **2020**, *32*, 1905914.

[11] C. R. Correia, S. Gil, R. L. Reis, J. F. Mano, *Adv. Healthcare Mater.* **2016**, *5*, 1346.

[12] S. Kasas, G. Longo, G. Dietler, *J. Phys. D: Appl. Phys.* **2013**, *46*, 133001.

[13] M. Stolz, R. Raiteri, A. U. Daniels, M. R. VanLandingham, W. Baschong, U. Aebi, *Biophys. J.* **2004**, *86*, 3269.

[14] D. Woodley, C. Rao, J. Hassell, L. Liotta, G. Martin, H. Kleinman, *Biochim. Biophys. Acta* **1983**, *761*, 278.

[15] H. J. McKerchar, S. Clerens, R. C. J. Dobson, J. M. Dyer, E. Maes, J. A. Gerrard, *Trends Food Sci. Technol.* **2019**, *86*, 217.
[16] J. T. O'Neal, E. Y. Dai, Y. Zhang, K. B. Clark, K. G. Wilcox, I. M. George, N. E. Ramasamy, D. Enriquez, P. Batys, M. Sammalkorpi, J. L. Lutkenhaus, *Langmuir* **2018**, *34*, 999.
[17] M. Matsusaki, M. Akashi, *Polym. J.* **2014**, *46*, 524.
[18] M. Matsusaki, K. Kadowaki, Y. Nakahara, M. Akashi, *Angew. Chem., Int. Ed.* **2007**, *46*, 4689.
[19] D. Lindner, C. Zietsch, P. M. Becher, K. Schulze, H.-P. Schultheiss, C. Tschöpe, D. Westermann, *Biochem. Res. Int.* **2012**, *2012*, 1.
[20] R. V. Iozzo, *Nat. Rev. Mol. Cell Biol.* **2005**, *6*, 646.
[21] G. Perry, W. Xiao, G. I. Welsh, A. W. Perriman, R. Lennon, *Integr. Biol.* **2018**, *10*, 680.
[22] P. Sharma, D. Rajalingam, T. K. S. Kumar, S. Singh, *Biophys. J.* **2008**, *94*, L71.
[23] Y. Wang, E. Gallagher, C. Jorgensen, E. P. Troendle, D. Hu, P. C. Searson, Martin. B. Ulmschneider, *Sci. Rep.* **2019**, *9*, 6117.
[24] Y. Hamano, J. A. Grunkemeyer, A. Sudhakar, M. Zeisberg, D. Cosgrove, R. Morello, B. Lee, H. Sugimoto, R. Kalluri, *J. Biol. Chem.* **2002**, *277*, 31154.
[25] H.-X. Zhou, X. Pang, *Chem. Rev.* **2018**, *118*, 1691.
[26] G. Bazzoni, E. Dejana, *Physiol. Rev.* **2004**, *84*, 869.
[27] M. Presta, P. Dell'Era, S. Mitola, E. Moroni, R. Ronca, M. Rusnati, *Cytokine Growth Factor Rev.* **2005**, *16*, 159.

Chapter 4

Fabrication of Shape-customized Artificial Basement Membranes in Organized 3D Tissues

4.1 Introduction

Tissue engineering has attracted much attention in the fabrication of 3D tissues. The design and construction of well-organized cellular architectures *in vitro* still present a major challenge for tissue engineering. Inspired by inherent multi-compartmentalized cellular constructs *in vivo*, different groups have begun exploring the control of isolated compartments for tissue engineering and regenerative medicine. For example, Rajagopalan and co-workers made the first attempt to construct a multilayered cellular architecture using a polyelectrolyte multilayer scaffold for the adhesion of the second layer of cells.[1] Recently, Ma[2] and Onoe[3] reported the fabrication of anisotropic hydrogel microparticles by multi-fluidic electrostatic spraying technique and centrifuge-based microfluidic device, respectively, for efficient and scalable 3D cell culture. However, *in vivo*, tissue architectures are not only simply multilayered structures. Thus, as part of 3D tissues, the shapes of natural BMs also vary in different tissues. The successful construction by the author of a robust A-BM based on Col-IV/LM LbL NFs has been described in the preceding three chapters. The obtained A-BMs had a similar microstructure to natural BMs, and their barrier functions to maintain cell compartmentalization while still allowing molecular transport were demonstrated. Moreover, the relationship between endothelial cell functions and the controllable surface roughness and physical properties were also studied carefully. Based on these results, in this chapter, the author constructed a shape-customized A-BM using the obtained Col-IV/LM multilayered nanofilms.

As mentioned in the general introduction, in addition to its versatility and available operation directly in 3D tissues, the LbL assembly technique has another major advantage: its compatibility with bioprinting, which allows for an increase in the complexity of the

multilayered scaffolds by controlling printing location and patterning. Generally, 3D bioprinting is a process of additive manufacturing to print living structures layer-by-layer, which corresponds to the alternate absorption of LbL assembly.[4,5] Therefore, there is great potential to integrate inkjet printing with LbL assembly for high-speed nanofilm fabrication. Hong[6] and co-workers demonstrated the viability of inkjet-based LbL assembly by the rapid fabrication of nanofilms with controlled composition and functionality on various substrates. Our group has reported simplified 3D-liver structures, produced by alternately inkjet printing cell suspensions and FN-G solutions, forming hundreds of multilayered micro-tissues in one micro-array, used for high-throughput drug evaluations.[7]

Although rapid fabrication of LbL nanofilms by inkjet printing has been reported, there are few studies on designing the shape of LbL nanofilms by inkjet printing. In this chapter, Col-IV and LM were printed alternately on adhered fibroblast layers by inkjet printing to construct shape-customized A-BMs. Another type of cell, endothelial cells, were seeded onto patterned A-BMs for 3D patterned cell co-culture, as shown in **Figure 4-1**.

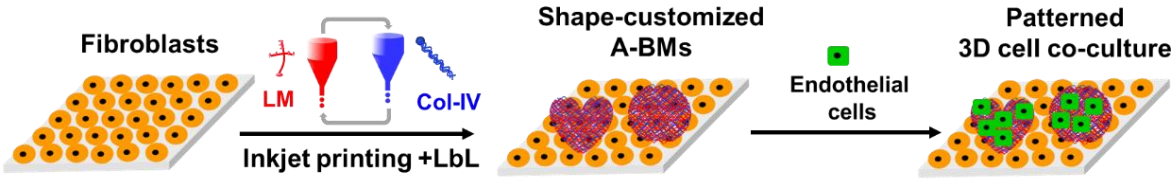

Figure 4-1. Schematic illustration of shape-customized A-BMs fabrication between endothelial cells and fibroblasts.

4.2 Experiments

4.2.1 Materials

Collagen type IV, FAM conjugated was purchased from AnaSpec (AS-85112, California, USA), and Laminin (Red fluorescent, rhodamine) was purchased from Cytoskeleton (LMN01-A, Colorado, USA). CellTracker™ Red CMTPX dye (C34552) was purchased from Thermo Fisher Scientific (MA, USA). Live/Dead staining Kit II was obtained from PromoCell GmbH (PK-CA707-30002, Heidelberg, Germany). CellTracker™ Green CMFDA dye (C2925) was purchased from Invitrogen (California, USA). Fibronogen (from bovine plasma, F8630) and

thrombin (from bovine plasma, T4648) were purchased from Sigma-Aldrich (St. Louis, USA).

4.2.2 Col-IV/LM LbL NFs printing

For the patterned LbL NFs printing, a piezo-electronic inkjet printer (DeskView^{TM}, Cluster technology, Osaka, Japan) was employed, which has four holders for nozzles with 25 μm of diameter and allow the alternate printing of different inks simultaneously, as previously described.[7,8] Briefly, around 150 μL of Col-IV and LM/Tris-HCl solutions (50 mM, pH=7.4, 100 μg/mL) were loaded to inkjet solution tanks, respectively. FAM-conjugated Col-IV (FAM-Col-IV, 100%) and rhodamine-conjugated LM (Rh-LM, 10%) were also used as printing inks to show the location of printing patterning. In order to get an intact patterning without gaps, pulse conditions have to be optimized to connect all sequential but independent liquid droplets dispensed from nozzles, as follows, voltage 10 V, frequency 100 Hz. By following the programs, layered patterning was obtained by the alternate deposition of Col-IV and LM without any drying or rinsing steps because spontaneous drying happened before the following printing process. CLSM (FV 3000) was used to observe the patterning shape and the colocalization between Col-IV layers and LM layers.

4.2.3 Col-IV/LM LbL NFs printing on cells

NHDF monolayer: In order to distinguish the printed patterning on cells surface, FAM-Col-IV solution was used to assembly with LM layers and NHDF was stained with cellTracker red in advance. NHDF monolayer with a density of 2.5×10^4 cells/cm^2 was firstly cultured on thin fibrin gels to avoid cell death during printing without medium. Fibrin gel was prepared in advance in homemade silicone wells by mixing fibrinogen (5 mg/mL) and thrombin (5 mg/mL) and then incubated at 37 ℃ for 30 min allowing the sufficient reaction between fibrinogen and thrombin.

3D NHDF constructs in fibrin gel: In order to solve the cell detachment issues during printing, NHDF (1.0×10^6 cells/mL) was seeded inside fibrin gel by simply but rapidly mixing fibrinogen solution (2 mg/mL) and thrombin solution (3.3 U/mL) containing suspended cell,

forming a flat 3D NHDF constructs supported by fibrin gel scaffold. NHDF was cultured overnight for cell adhesion. Before printing, the cell culture medium was removed completely to avoid inks diffusion, reducing patterning resolutions. After printing, the 3D structure was cultured in DMEM. FV 3000 was used to observe printed NFs, and the stability of printed NFs was evaluated from the fluorescent intensity of FAM-Col-IV.

4.2.4 Construction of patterned 3D cell co-culture structure

Followed by the printing of Col-IV/LM LbL NFs with different patterning, 10 μL of GFP-HUVEC suspensions were dispensed onto NFs using the pipette. The whole sample was kept in the incubator for 2 h allowing cell adhesion and then cultured in mixed cell culture medium (DMEM: EGM-2 = 1:1). Cell culture medium was changed every day. Patterned cell co-culture structure was observed by FV 3000.

4.3 Results and discussion

4.3.1 Shape-customized Col-IV/LM NFs construction

First, by simply following printing programs, patterned Col-IV/LM NFs were printed on glass slides, including circle, heart, and ginkgo leaf. The author used a piezo-electronic inkjet printing instrument with two injectors with 25 μm-sized nozzles, and thus different protein solutions could be co-localized alternately. Also, pulse conditions and other parameters such as voltage, frequency, stage moving speed, and patterning size, have to be optimized according to the substrates with different hydrophilicities to obtain a homogeneous and intact printing layer, as shown in **Figure 4-2b**. Stepwise printing of FAM-conjugated Col-IV (FAM-Col-IV) and rhodamine-conjugated LM (Rh-LM) was performed to fabricate 5 bilayers of patterning, and subsequently, these multilayered patterns were then analyzed by CLSM (**Figure 4-2b, c**). As shown in **Figure 4-2b** and **d**, the luminescence of FAM-Col-IV and Rh-LM increased gradually as the printing layers increased. FAM-Col-IV and Rh-LM overlaid perfectly with each other from the merged images, suggested the successful construction of patterned Col-IV/LM LbL NFs.

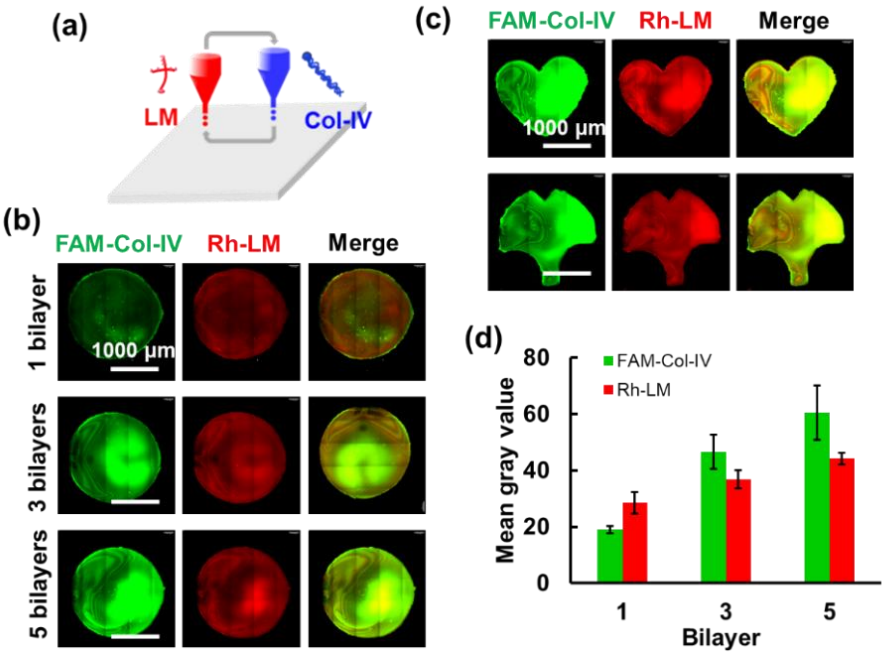

Figure 4-2. (a) Schematic illustration of the development of shape-customized Col-IV/LM NFs using LbL assembly and inkjet printing techniques. (b) CLSM images of rounded LbL NFs prepared by the alternate printing of 100 μg/mL of Col-IV and LM/Tris-HCl solutions (50 mM, pH=7.4). For the observation, Col-IV was conjugated with FAM (FAM-Col-IV) and LM was conjugated with rhodamine (Rh-LM), respectively. (c) CLSM images of heart- and ginkgo leaf-shaped Col-IV/LM NFs with 5 bilayers. (d) Fluorescent intensity of FAM-Col-IV and Rh-LM with various bilayers. n=3.

4.3.2 Shape-customized Col-IV/LM NFs construction on cells

Although living cell printing and multilayered LbL spots by step-by-step dot-printing have been reported,[8,9] patterned LbL NF construction, even just LbL spot-printing on an existing cell monolayer, has still rarely been reported.[7] Given the variously shaped tissue structures, the *in-situ* construction of A-BMs is necessary. As shown in **Figure 4-3a**, shape-customized Col-IV/LM LbL NFs were printed on a living fibroblasts monolayer. To ensure the survival of cells during printing, NHDF were seeded on thin fibrin gels that provide humid environments for cells. Fibrin gel was chosen because of its biocompatibility for tissue engineering and its transparency for subsequent observation. FAM-Col-IV was employed to show the printing patterning and position. Generally, patterned Col-IV/LM NFs (**Figure 4-3b, c**) were successfully constructed on an NHDF monolayer (NHDF was stained with CellTracker red,

Figure 4-3c). Multiple patterning with various layers could also be easily controlled by inkjet printing, where the luminescence of FAM-Col-IV increased gradually as the bilayer numbers increased (**Figure 4-3c**). Unfortunately, cell detachment occurred from the underlying substrates, probably because of the pressure caused by repeated droplets from nozzles, especially around the edges of the patterning. The detachment became more severe as more layers were printed. As shown in **Figure 4-3d**, the remaining cell amount after printing was analyzed using live/dead cell staining. The remaining cell number declined dramatically as the printing layers increased. Only around 20% of cells remained after the printing of 5 bilayers. Even though cell detachment happened, live/dead staining clearly showed considerably high cell viability independent of the printing layers (**Figure 4-3d**). Moreover, the stability of printed LbL NFs on cell monolayers incubated in cell culture medium for 6 days was evaluated from the CLSM images (**Figure 4-3e**). The gradually declining amount of nanofilms remaining from Day 1 to Day 6 was probably caused by the enzyme degradation co-cultured with cells.[10,11] Besides enzyme degradation, a drastically declining of nanofilms amount at Day 1 was also caused by the rapid disassembly of excessively deposited Col-IV and LM because of the lack of rinsing steps between each step. Although *in-situ* TGase catalyzed-crosslinking slowed down the enzyme degradation process, cell detachment and weak interaction between excess components still induced the loss of most of the printed proteins.

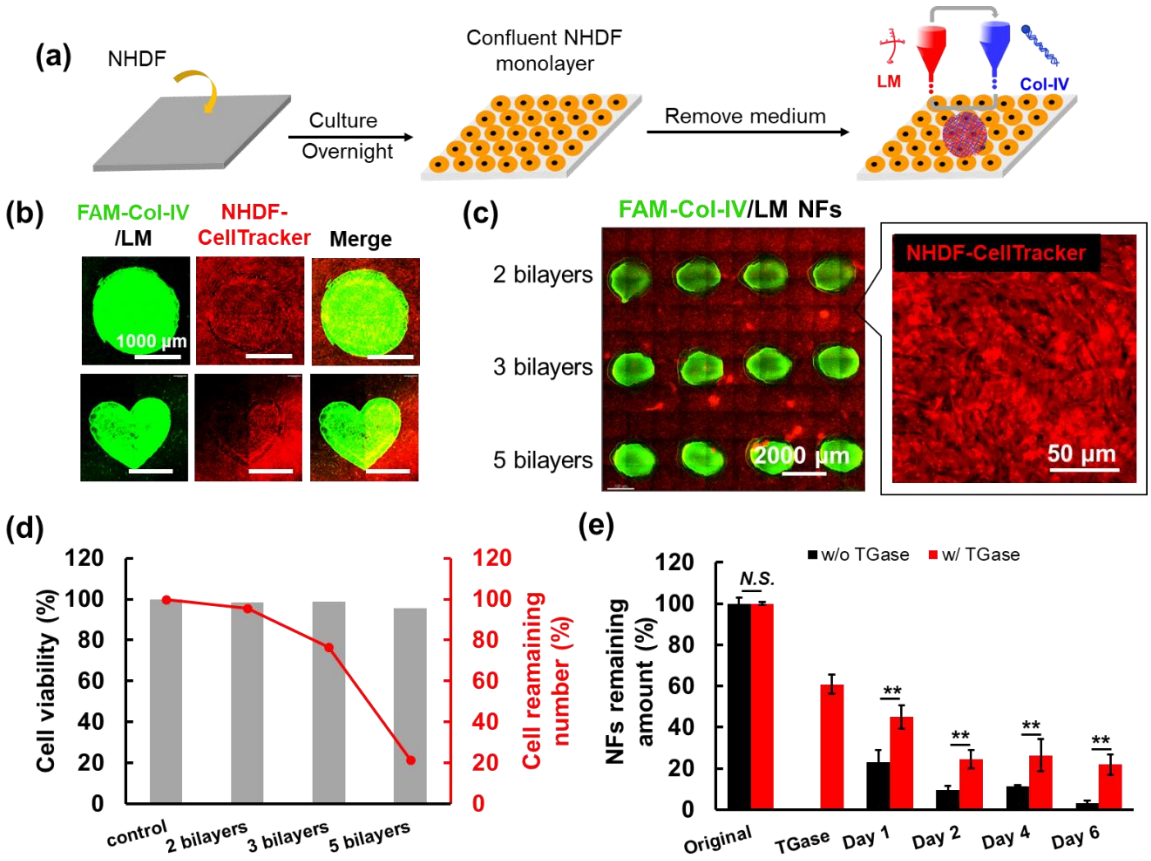

Figure 4-3. (a) Schematic illustration of shape-customized LbL Col-IV/LM NFs construction on an NHDF monolayer by inkjet printing. (b) CLSM images of round and heart-shaped Col-IV/LM NFs with 5 bilayers on NHDF. Printing inks were 100 μg/mL of Col-IV and LM/Tris-HCl solutions (50 mM, pH=7.4), respectively. Col-IV was conjugated with FAM and NHDF were stained with CellTracker red. (c) Multiple round NFs with 2, 3 and 5 bilayers on NHDF monolayers (left) and confluent NHDF monolayer (right). (d) Cell viability and remaining cell number after printing were analyzed from the live/dead cell staining images by ImageJ. (e) Stability of printed NFs on NHDF monolayers, which was co-cultured for 6 days. n=3, $^{**}p < 0.01$.

4.3.3 Patterned 3D cell co-culture

To solve the cell detachment issue, NHDF were seeded into thin fibrin gels that not only provide a humid environment but also a scaffold to protect cells from the pressure (**Figure 4-4a**). Round Col-IV/LM NFs were then printed on 3D cell constructs inside the fibrin gels (**Figure 4-4b**). However, due to the slightly hydrophobic surface of the fibrin gel, printed inks diffused inhomogeneously, forming irregular circles. NHDF conditions were evaluated

immediately after printing by FV 3000. As shown in **Figure 4-4c**, even though the fibrin gel surface sunk slightly due to the pressure, the adherent condition and cell morphology were well maintained thanks to the protection of the scaffolds (Fibrinogen-Alexa Fluor™ 594 Conjugate). **Figure 4-4d** shows negligible dead cells, indicating high cell viability. Next, 10 µL of GFP-HUVEC were seeded around Col-IV/LM NFs using a pipette, and the 3D NHDF constructs were under the Col-IV/LM NFs. After 3 days of co-culture, a patterned 3D co-culture was observed from both top and side views (**Figure 4-4e**). Cell compartmentalization was successfully achieved through the assistance of patterned A-BMs, (**Figure 4-4e**, side view). Taken together, our results demonstrated that shape-customized LbL NFs could be constructed on the surface of cells without damaging cells by inkjet printing, which contributed to the patterned 3D cell co-culture and organized 3D tissue construction.

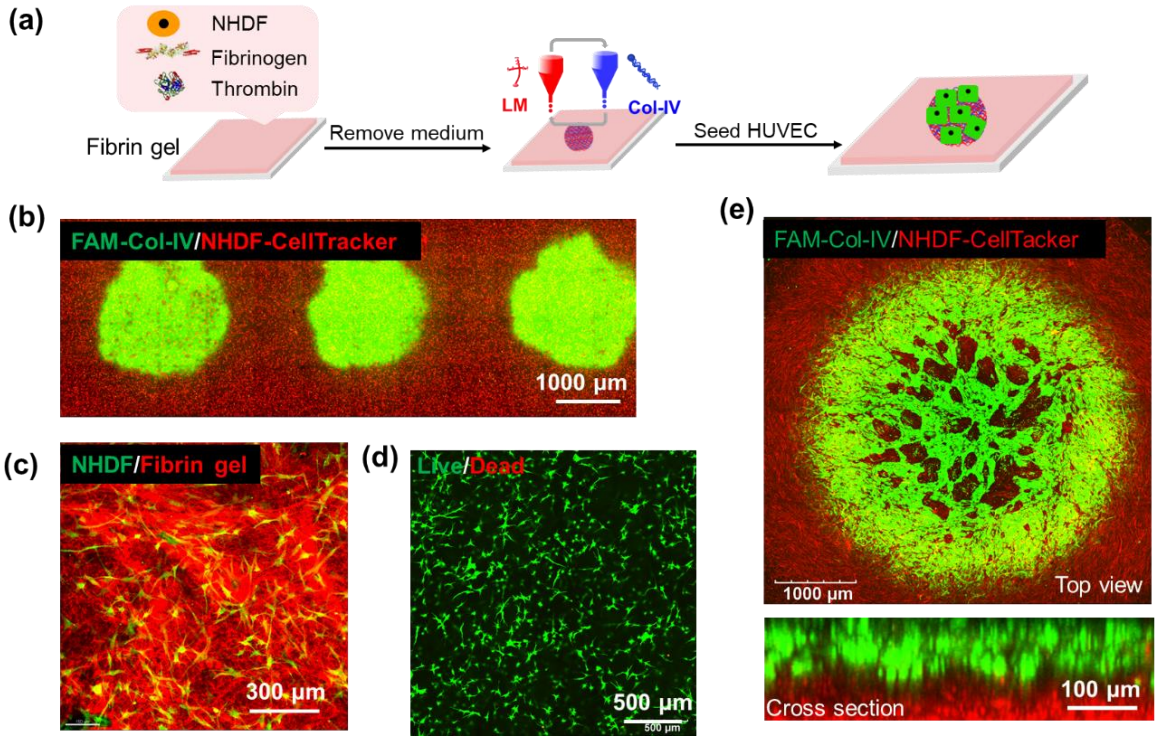

Figure 4-4. (a) Schematic illustration of the fabrication of shape-customized A-BMs on 3D cell constructs and patterned 3D cell co-culture. NHDF were seeded in a thin fibrin gel that was formed by the gelation of fibrinogen and thrombin. (b) CLSM image of round Col-IV/LM NFs on 3D cell constructs after printing. (c) CLSM images of NHDF (CellTracker green) inside a 3D fibrin gel scaffold. Fibrinogen was conjugated with Alexa Fluor™ 594. (d) Live/dead cell staining was observed immediately after printing. (e) CLSM images of patterned cell co-culture between NHDF (CellTracker red) and GFP-HUVEC with the assistance of patterned A-BMs after 3 days incubation. Up: top view, bottom: cross-section of 3D co-culture structure.

4.4 Conclusion

In this chapter, shape-customized Col-IV/LM multilayered nanofilms were fabricated successfully in 3D tissues directly by combining the LbL assembly approach and inkjet printing. Patterned fibroblasts and endothelial cell co-culture was achieved by the assistance of shape-customized A-BMs, contributing to the construction of patterned 3D tissues *in vitro* and providing more reliable organized tissue models for evaluating drug efficacy, nanotoxicology, and implantation.

4.5 Reference

[1] P. Rajagopalan, C. J. Shen, F. Berthiaume, A. W. Tilles, M. Toner, M. L. Yarmush, *Tissue Eng.* **2006**, *12*, 1553-1563.

[2] Y.-C. Lu, W. Song, D. An, B. J. Kim, R. Schwartz, M. Wu, M. Ma, *J. Mater. Chem. B* **2015**, *3*, 353.

[3] S. Yoshida, M. Takinoue, H. Onoe, *Adv. Healthcare Mater.* **2017**, *6*, 1601463.

[4] C. M. Andres, N. A. Kotov, *J. Am. Chem. Soc.* **2010**, *132*, 14496.

[5] B. Elder, R. Neupane, E. Tokita, U. Ghosh, S. Hales, Y. L. Kong, *Adv. Mater.* **2020**, 1907142.

[6] M. Choi, J. Heo, D. Choi, S. Hwangbo, J. Hong, *Macromol. Mater. Eng.* **2017**, *302*, 1700332.

[7] M. Matsusaki, K. Sakaue, K. Kadowaki, M. Akashi, *Adv. Healthcare Mater.* **2013**, *2*, 534.

[8] T. Akagi, T. Fujiwara, M. Akashi, *Langmuir* **2014**, *30*, 1669.

[9] M. Choi, H. H. Park, D. Choi, U. Han, T. H. Park, H. Lee, J. Park, J. Hong, *Adv. Healthcare Mater.* **2017**, *6*, 1700216.

[10] T. H. Vu, *Genes Dev.* **2000**, *14*, 2123.

[11] D. Lindner, C. Zietsch, P. M. Becher, K. Schulze, H.-P. Schultheiss, C. Tschöpe, D. Westermann, *Biochem. Res. Int.* **2012**, *2012*, 1.

Concluding Remarks

In this thesis, the author described the ability of A-BMs based on Col-IV/LM LbL nanofilms to imitate the structure and biofunctions of natural BMs.

The simple operation and materials-versatility of the LbL assembly method enable the fabrication of nanometer-sized films with controllable components and thickness. The obtained multilayered Col-IV/LM NFs showed adjustable components, thickness, and porous networks similar to natural BMs. A wide range of surface roughness and Young's modulus of Col-IV/LM NFs were achieved by simply changing the concentrations of assembly solutions, allowing for application as A-BMs in different tissues *in vitro*. Benefit by the specific interactions among Col-IV, LM and cell membrane, cell functions, including cell adhesion, proliferation, differentiation, were enhanced on A-BMs. Col-IV/LM NFs acting as a physical barrier permitted the compartmentalized coculture of fibroblasts and endothelial cells but allowed cell-cell crosstalk by molecular permeability through the porous networks. Furthermore, a robust A-BMs based on crosslinked Col-IV/LM NFs was developed by adding TGase on 3D fibroblast tissue. By *in-situ* cross-linking, the stability of A-BMs maintained between endothelial cells and fibroblast tissues was improved, contributing to the maintenance of cell compartmentalization for a longer time.

The author described the structure, mechanical properties, and biofunctions of A-BMs above. The comparison with natural BMs is discussed below (**Table 2**).

Compared with natural BMs, the network density of Col-IV/LM NFs was slightly lower, possessing a larger pore size and fiber diameter, which caused a higher molecular permeability (2.6%) than the results *in vivo*. It is worth noting, however, that pores and fibers structure of nanofilms were observed in a dry state and that will vary with wetting conditions. Meanwhile, thanks to their versatility and simple operation, the thickness and Young's modulus of Col-IV/LM NFs were controllable over a wide range to satisfy the requirements in different tissues. Although the obtained A-BMs could assist in preventing cell migration for up to 5 days that was lower than the stability of natural BMs maintaining cell compartmentalization, the

construction speed of Col-IV/LM NFs was much quicker than the self-development by cells/tissues. It has been reported that in the case of immortalized alveolar type-II epithelial cells cultured with Matrigel *in vitro*, the globular or fibrous deposits of laminin were fused into a mesh or a partly plugged mesh after 5 days of culture and a thin BM sheet formed after 10 days of culture. Therefore, A-BMs based on Col-IV/LM NFs will play an essential role in maintaining organized cell co-culture before the secretion of BMs components and assist the assembly and formation of regenerative BMs in 3D tissues.

Table 2. Comparison of microstructure and functions of A-BMs and natural BMs.

	A-BMs		Natural BMs
	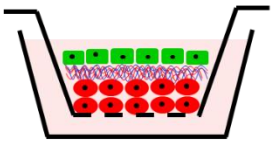		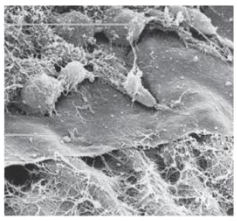
Thickness	<1000 nm	≈	50-100 nm
Pore size	240±150 nm	>	40-105 nm*
Fiber diameter	120±50 nm	>	24-67 nm*
Young's modulus	0.5 KPa-38 MPa	≈	0.5 KPa-5 MPa
3D cell separation	5 days	<	< 90 days#
Construction speed	2 hours	<	10 days
Permeability (albumin)	2.6%	>	0&

*Data from vascular BMs; #cell renew cycle *in vivo*, and &data measured together with cells in kidney.

Furthermore, shape-customized Col-IV/LM multilayered nanofilms were fabricated successfully in 3D tissues directly by the combination of the LbL assembly technique and inkjet printing. Patterned fibroblasts and endothelial cells co-culture were achieved by the assistance of shape-customized A-BMs, contributing to the construction of patterned 3D tissues *in vitro* and providing more reliable organized tissue models for evaluating drug efficacy, nanotoxicology, and implantation.

List of Publications

Chapter 1

1. Fabrication of Artificial Nanobasement Membranes for Cell Compartmentalization in 3D Tissues
   Jinfeng Zeng, Naoko Sasaki, Clara R. Correia, João F. Mano, Michiya Matsusaki
   Small **2020**, *16*, 1907434.

Chapter 2

2. Analysis of Thickness and Roughness Effects of Artificial Basement Membranes on Endothelial Cell Functions
   Jinfeng Zeng and Michiya Matsusaki
   Anal. Sci. **2021**, *37*, 491-497.

3. Studies of Substrates Effects on Stiffness of Type IV Collagen and Laminin Multilayered LbL NFs by AFM Force Spectroscopy
   Jinfeng Zeng, Anchu Viswan, Ayana Yamagishi, Chikashi Nakamura, Michiya Matsusaki
   In preparation

Chapter 3

4. *In Situ* Cross-Linking of Artificial Basement Membranes in 3D Tissues and Their Size-Dependent Molecular Permeability
   Jinfeng Zeng, Clara R. Correia, João F. Mano, Michiya Matsusaki
   Biomacromolecules **2020**, *21*, 4923-4932.

Supplementary publications

1. Layer-by-Layer Assembly of NFs to Control Cell Functions
   Jinfeng Zeng and Michiya Matsusaki
   Polym. Chem. **2019**, *10*, 2960-2974.

2. Liquefied Microcapsules as Dual-Microcarriers for 3D+3D Bottom-Up Tissue Engineering
   Clara R. Correia, Isabel M. Bjørge, **Jinfeng Zeng**, Michiya Matsusaki, João F. Mano
   Adv. Healthcare Mater. **2019**, *8*, 1901221.

Acknowledgments

This study was carried out from 2018 to 2021 at Department of Applied Chemistry, Graduate School of Engineering, Osaka University. In the past three years, I have received a lot of assistance and support for my study and daily life. Upon the completion of this thesis, I would like to express my gratitude to all those who have helped me.

First and foremost, I am extremely grateful to my supervisor, Prof. Michiya Matsusaki for his invaluable advice, continuous support, and patience at every stage of the research project. I am completely impressed by his invaluable expertise to think in a unique and wide perspective, as well as his endless enthusiasm on research. His word “There is no bad data” taught me the right attitude to research. I also appreciate that Prof. Matsusaki provided me valuable opportunities to display the achievements I got and communicated with other researchers. These absolutely broaden my horizon and enrich my life experience.

I am deeply grateful to the thesis committee: Prof. Toshiyuki Kida and Prof. Kazuya Kikuchi, for their insightful comments and their donation of time. I would like to extend my sincere thanks to Prof. João F. Mano in University of Aveiro for his insightful comments and suggestions in the experiment, data discussion and article writing. Thanks to Prof. Hiroshi Uyama, Associate Prof. Taka-Aki Asoh, and Prof. Chikashi Nakamura in AIST (Tsukuba) for their assistance and suggestions in AFM measurements. Thanks to Prof. Mitsuru Akashi and Associate Prof. Takami Akagi for their help in DLS measurements.

Besides my supervisor, I am deeply grateful to Assistant Prof. Masahiko Nakamoto for his insightful comments and suggestions for my research. Thanks Dr. Fiona Louis, Dr. Dong-Hee Kang, Dr. Naoko Sasaki, Dr. Zhengtian Xie, Dr. Hirotaka Nakatsuji and Dr. Agathe Figarol for their comments, suggestions and guidance to my experiments.

I would like to offer my special thanks to Ms. Eri Enomoto, Ms. Chika Sugiki, and Ms. Yukako Miyamoto for their warmhearted support and kind help in the laboratory affairs and daily life.

My appreciation also goes to the previous and current fellows in the laboratory: Thanks to Guest Associate Prof. Shiro Kitano, Guest Associate Prof. Shinji Irie, Visiting researcher Asuka Kato, Yasuyuki Naito, Yuka Yoshinouchi, and Dr. Keisuke Sumiyoshi. Thanks to Ms. Yukiko Sorayama, Ms. Natsuko Kato, Mr. Kouki Nishi, Mr. Yasuhiro Naka, Mr. Yuichi Yukawa, Mr. Hao Liu, Ms. Jinyu Li, Mr. Kazuma Ishiguro, Mr. Noboru Hiraoka, Mr. Abdul Sisak Muhammad Asri, Ms. Marie Piantino, Mr. Yucheng Shang, Mr. Tomoyuki Suezawa, Mr. Daisuke Tomioka, Ms. Yuning Zhang, Ms. Lingyu Pei, Mr. Shogo Shimada, Mr. Ryo Mitsuyasu, Mr. Rei Miyata, Mr. Yuki Koba, Mr. Tomoya Matsuo, Mr. Kazuki Moroishi, Mr. Kazuki Yoshida, Mr. Tamaki Kumauchi and so on. Thanks to their accompany and kind help for both research and daily life.

I would like to thank the financial supporting for international conference from Osaka University Engineering Society and research support from Japan Society for the Promotion of Science (JSPS, DC2, A21J128330).

Finally, I would like to express my deep appreciate to my husband, Changming Jin. Thanks to his love, respect, accompany, patience and support. Thanks to my parents, my brother, parents-in-law, grandparents for their accompany and encouragement.

June 2021

ZENG JINFENG